



Five Key Exoplanet Questions Answered via the Analysis of 25 Hot-Jupiter Atmospheres in Eclipse

Q. Changeat^{1,11} , B. Edwards^{1,2,11} , A. F. Al-Refaie¹ , A. Tsiaras^{1,3} , J. W. Skinner⁴, J. Y. K. Cho⁵ , K. H. Yip¹ , L. Anisman¹ , M. Ikoma^{6,7} , M. F. Bieger⁸ , O. Venot⁹ , S. Shibata¹⁰ , I. P. Waldmann¹ , and G. Tinetti¹

¹ Department of Physics and Astronomy, University College London, Gower Street, London WC1E 6BT, UK; quentin.changeat.18@ucl.ac.uk

² AIM, CEA, CNRS, Université Paris-Saclay, Université de Paris, F-91191 Gif-sur-Yvette, France

³ INAF, Osservatorio Astrofisico di Arcetri, Largo E. Fermi 5, I-50125 Firenze, Italy

⁴ School of Physics and Astronomy, Queen Mary University of London, Mile End Road, London E1 4NS, UK

⁵ Center for Computational Astrophysics, Flatiron Institute, 162 Fifth Avenue, New York, NY 10010, USA

⁶ Division of Science, National Astronomical Observatory of Japan, 2-21-1 Osawa, Mitaka, Tokyo 181-8588, Japan

⁷ Department of Astronomical Science, The Graduate University for Advanced Studies (SOKENDAI), 2-21-1 Osawa, Mitaka, Tokyo 181-8588, Japan

⁸ College of Engineering, Mathematics and Physical Sciences, University of Exeter, North Park Road, Exeter, UK

⁹ Université de Paris and Univ Paris Est Creteil, CNRS, LISA, F-75013 Paris, France

¹⁰ Institute for Computational Science, Center for Theoretical Astrophysics & Cosmology, University of Zurich, Winterthurerstr. 190, 8057 Zurich, Switzerland

Received 2021 August 9; revised 2022 January 31; accepted 2022 February 28; published 2022 April 25

Abstract

Population studies of exoplanets are key to unlocking their statistical properties. So far, the inferred properties have been mostly limited to planetary, orbital, and stellar parameters extracted from, e.g., Kepler, radial velocity, and Gaia data. More recently an increasing number of exoplanet atmospheres have been observed in detail from space and the ground. Generally, however, these atmospheric studies have focused on individual planets, with the exception of a couple of works that have detected the presence of water vapor and clouds in populations of gaseous planets via transmission spectroscopy. Here, using a suite of retrieval tools, we analyze spectroscopic and photometric data of 25 hot Jupiters, obtained with the Hubble and Spitzer Space Telescopes via the eclipse technique. By applying the tools uniformly across the entire set of 25 planets, we extract robust trends in the thermal structure and chemical properties of hot Jupiters not obtained in past studies. With the recent launch of the James Webb Space Telescope and the upcoming missions Twinkle and Ariel, population-based studies of exoplanet atmospheres, such as the one presented here, will be a key approach to understanding planet characteristics, formation, and evolution in our galaxy.

Unified Astronomy Thesaurus concepts: Exoplanet atmospheres (487); Bayesian statistics (1900); Surveys (1671); Hubble Space Telescope (761); Astronomy data reduction (1861)

Supporting material: figure sets, machine-readable tables

1. Introduction

More than 4700 exoplanets are currently known and for about 80 of these, we have atmospheric data recorded with the Hubble Space Telescope (HST), Spitzer Space Telescope, and ground-based instruments. To date, most data-oriented atmospheric analyses have focused on individual targets and only a very limited number of studies are available on populations of exoatmospheres observed with the transit or eclipse technique (Sing et al. 2016a; Tsiaras et al. 2018; Pinhas et al. 2019; Mansfield et al. 2021). In this article, we analyze eclipse spectra and photometric data, observed with the HST G141 grism and the Spitzer Space Telescope, for 25 planets. Eclipse spectra recorded in the infrared are sensitive to vertical thermal profiles and can provide strong constraints on the chemistry and thermal properties of the daysides of exoplanets. These data, taken collectively and interpreted with a suite of retrieval tools uniformly applied, are used to answer five key open questions

in exoatmospheric chemistry, circulation, and planet formation. The questions are:

- (1) *Do metal oxides and hydrides cause thermal inversions in exoplanet atmospheres?* Early theoretical and observational studies of hot Jupiters have highlighted the potential impact of metal hydrides and metal oxides in regulating the thermal properties of the dayside of hot Jupiters (Hubeny & Burrows 2009; Spiegel et al. 2009; Burrows 2014; Nugroho et al. 2017). Theoretical predictions (Lodders 2002; Fortney et al. 2008) have suggested that, analogously to brown dwarfs, planets hotter than ~ 1700 K might have metal hydrides and metal oxides in gaseous form: these molecular species are excellent absorbers in the optical/near-infrared and might cause a hot layer in the atmosphere and therefore a thermal inversion. By contrast, planets colder than ~ 1700 K might not exhibit such thermal inversions, as metal hydrides and metal oxides have been sequestered into condensates.
- (2) *Are the eclipse spectra of the hottest atmospheres consistent with blackbody curves?* Recent theoretical studies (Bell & Cowan 2018; Lothringer et al. 2018; Parmentier et al. 2018) have suggested H^- is an important opacity source, generated by the thermal dissociation of H_2 and H_2O at very hot temperatures

¹¹ These authors contributed equally to this work.



($T > 2500$ K). Eclipse spectra of very hot atmospheres would therefore resemble blackbody curves due to the continuous shape of H^- emission and the absence of other molecules that have been dissociated. Observational evidence in favor of those predictions was obtained by studies of individual planets with HST and Spitzer (Kreidberg et al. 2018; Mansfield et al. 2018; Arcangeli et al. 2019) and more recently in the HST population analysis from Mansfield et al. (2021). However, many other works (Haynes et al. 2015; Edwards et al. 2020; Mikal-Evans et al. 2020; Changeat & Edwards 2021) have found spectral signatures in similarly hot atmospheres.

- (3) *What is the dayside–terminator contrast in exoplanet atmospheres?* Planetary atmospheres present vertical and horizontal inhomogeneities: This is particularly true for tidally locked planets, for which large day–night thermal gradients, sometimes in excess of 1000 K, and asymmetric circulation patterns have been predicted (Cho et al. 2003; Showman et al. 2010; Cowan & Agol 2011; Roth et al. 2021). Recent simulations using pseudospectral methods (Skinner & Cho 2021a, 2021b; Cho et al. 2021) have revealed the complex and turbulent nature of these atmospheres, displaying highly dynamic small- and large-scale storms that develop and evolve in time. Some studies (Tan & Komacek 2019; Roth et al. 2021) have hypothesized that optical absorbers and thermal dissociation/recombination processes would impact the atmospheric dynamics. Namely, if H_2 dissociates at the dayside and recombines at the nightside, this would increase the energy transport, thus reducing the day–night temperature contrast. Mansfield et al. (2020b) provided observational evidence of these effects in the Spitzer phase-curve of KELT-9 b. On the other hand, optical absorbers such as TiO , VO , and FeH are more thermally stable, so they would not contribute much to this effect. The comparison between eclipse and transit observations might constrain these dynamical processes.
- (4) *Are metallicity and C/O viable observables to understand planet formation?* Hot Jupiters are thought to form via a three-step process (Mizuno 1980; Bodenheimer & Pollack 1986; Ikoma et al. 2000): solid core accretion, runaway gas accretion, and migration. The core accretion is believed to occur in the outer regions of a protoplanetary disk, where the abundance of solid materials leads to the rapid growth of a planetary core before disk gas dispersal. If that is the case, the composition of giant exoplanets, which is a direct outcome of these planetary formation processes, is predicted to be substellar in heavy elements such as C, O, and refractory elements because most of the heavy elements would be sequestered in the cores. The inferred superstellar bulk metallicities of Jupiter, Saturn, and warm exo-Jupiters (Saumon & Guillot 2004; Miller & Fortney 2011; Thorngren et al. 2016; Welbanks et al. 2019), however, suggest a more complicated picture, where heavy elements are also captured through some other processes, probably during gas accretion and/or migration (Hasegawa et al. 2018; Shibata & Ikoma 2019; Shibata et al. 2020; Turrini et al. 2021). Also, while difficult to determine today, the C/O of exoplanets may place constraints on where and how the giant planets collect gas and solids in evolving protoplanetary disks

(Mordasini et al. 2016; Booth et al. 2017; Brewer et al. 2017; Madhusudhan et al. 2017; Eistrup et al. 2018; Cridland et al. 2019). Constraints on those two parameters would significantly improve our understanding of planetary formation.

- (5) *Can refractory elements help us understand exoplanet formation?* In addition to the metallicity and C/O, other elemental ratios, such as N/O, S/O (Turrini et al. 2021), or even refractory elements (Lothringer et al. 2021), may help constrain planet formation scenarios. Their potential, however, remains unexplored by observational studies, as their tracers are more difficult to detect. While HST is not particularly sensitive to N- and S-bearing species, refractory elements such as TiO , VO , and FeH have been detected previously in eclipse spectra.

2. Methodology

Our study encompasses data for 25 hot Jupiters observed in eclipse with the HST-WFC3 G141 grism and Spitzer: CoRoT-1 b (CO1), HAT-P-2 b (HP2), HAT-P-7 b (HP7), HAT-P-32 b (HP32), HAT-P-41 b (HP41), HAT-P-70 b (HP70), HD 189733b (HD189), HD 209458b (HD209), KELT-1 b (K1), KELT-7 b (K7), KELT-9 b (K9), Kepler-13 A b (Ke13), TrES-3 b (Tr3), WASP-4 b (W4), WASP-12 b (W12), WASP-18 b (W18), WASP-19 b (W19), WASP-33 b (W33), WASP-43 b (W43), WASP-74 b (W74), WASP-76 b (W76), WASP-77 A b (W77), WASP-79 b (W79), WASP-103 b (W103), and WASP-121 b (W121). For WASP-121 b, we also add the available G102 grism. While some of these data sets have already been published individually in previous works, to ensure the consistency of our analysis, we have reanalyzed the raw HST data with our open-source pipeline, Iraclis (Tsiaras et al. 2016b). Below, we also refer to the data analysis leading from raw observational data to spectra as “data reduction” to distinguish this process from the analysis/interpretation of the atmospheric spectrum. Only two exoplanets, Kepler-13A b and WASP-33 b, were taken as is from the literature. WASP-33 b orbits a pulsating δ Scuti star, and Kepler-13A b is part of a triple-star system. Reduction of the data for these particular targets requires particularly careful modeling of the host stars, which is not explored in this study. For our retrieval analyses we have used Alfnor (Changeat et al. 2020a), a tool that extends the atmospheric retrieval capabilities of TauREx3 (Al-Refaie et al. 2021a) to populations of atmospheres. More technical details on our tools and methods are reported in Appendix B.

For each planet, we tested predefined scenarios, varying the molecular species included, the model assumptions, and whether Spitzer data are included. As potential biases in retrieval studies can arise from combining HST and Spitzer observations (Changeat et al. 2020b; Yip et al. 2020), we assessed the robustness of our results against possible biases by artificially modifying the Spitzer data and performing additional retrievals. More specifically, we repeated our analysis with Spitzer data offset by +100, −100 ppm and doubled uncertainties.

The free retrieval runs assumed abundances constant with altitude and included molecular species such as H_2O , CO , CO_2 , and CH_4 in a “reduced” run. Refractory species (TiO , VO , and FeH) and H^- were added in a “full” run. Please note that H^- absorbing properties are traced by the e^- abundance (John 1988). Atomic and ionic species are not considered here

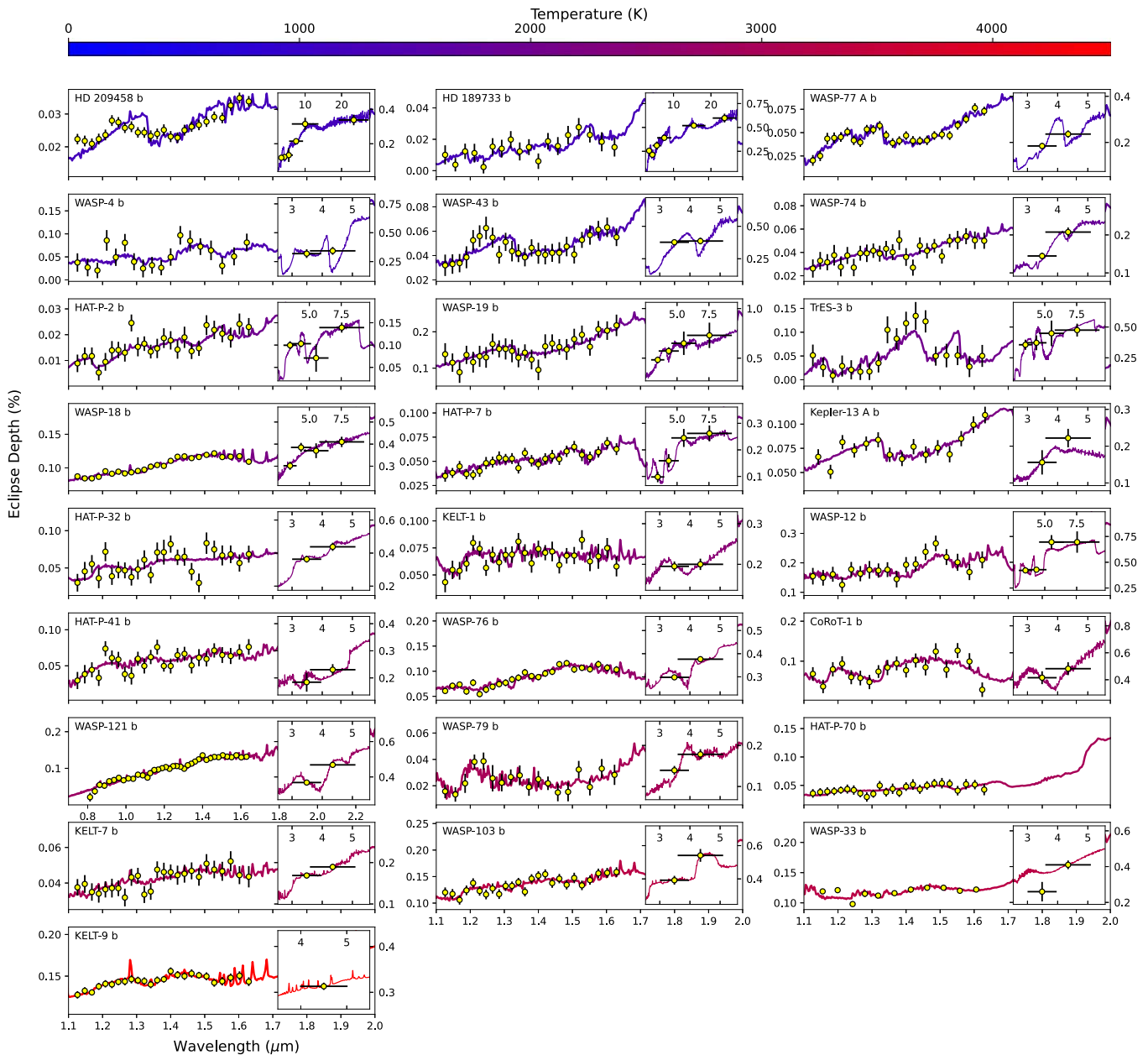


Figure 1. Best-fit spectra of the 25 planets considered in this study for the HST+Spitzer observations in eclipse. Individual analyses and additional retrievals, including a simpler blackbody fit, can be found in Appendix D. The planets are ordered in increasing atmospheric temperatures, which are traced by the colors (from blue to red). The retrieved atmospheric temperature is obtained by weighting the retrieved thermal profile by the contribution function. Unlabeled x -axes range from 1.1 to 2 μm .

as they do not absorb in the HST and Spitzer wavelength regions. In the rest of the paper, we use the term “refractory” to refer to TiO, VO, and FeH, and we use the term “optical absorber” to refer to TiO, VO, FeH, and H^- . We have also attempted equilibrium chemistry retrievals, using the GGChem code (Woitke et al. 2018) and including all the supported species, in our entire population. We used the Bayesian evidence to compare the results with the free runs. In all models, the temperature profile is determined using a heuristic N -point profile. Because the thermal profile varies with altitude, the reported value is the mean atmospheric temperature obtained in the retrievals, weighted by the atmospheric contribution function. It characterizes the thermal conditions of the atmosphere in the region probed by the observations. Note that this is not equal to the blackbody temperature or the

equilibrium temperature. For reference, best-fit blackbody temperatures are provided in Appendix D, which analyzes the planets individually.

For a subset of 17 planets, we have also analyzed the G141 transit observations using Iraclis to include additional information about the terminator region of those planets in our study.

3. Results

The HST eclipse observations reduced with our Iraclis pipeline are shown in Figure 1, alongside the Spitzer photometric data. A summary of the observations considered in this paper and relative references are given in Table B1 in Appendix B. We also show in Figure 1 the best-fit spectra obtained with Alfnor. The cooler planets in the sample, such

Table 1
Summary of Our “Full” Retrievals on HST+Spitzer Eclipse Data (Day) and the HST Transit Data (Term)

Planet	Term Detections	Term Clouds	Term T (K)	Day Detections	Day T (K)	Day Profile
CoRoT-1 b	<u>VO</u>	No	2862 ⁺⁵³⁷ ₋₁₁₀₅	H₂O, VO, H⁻	1924 ± 374	Inverted
HAT-P-2 b	<i>H₂O, VO</i>	2168 ± 123	Not Inverted
HAT-P-7 b	None	Featureless	Unknown	*H₂O, *FeH, *CO₂	2562 ± 253	Inverted
HAT-P-32 b	H₂O	Yes	2396 ⁺²⁶¹ ₋₃₁₄	<i>H⁻</i>	1962 ± 83	Inverted
HAT-P-41 b	H₂O	Yes	2002 ⁺³⁶⁴ ₋₄₄₆	None	2304 ± 169	Not Inverted
HAT-P-70 b (HST)	<u>H⁻</u>	2321 ± 263	Inverted
HD 189733b	H₂O	Yes	778 ⁺¹⁷⁹ ₋₁₁₆	*H₂O, *CO₂, *FeH	1388 ± 104	Not Inverted
HD 209458b	H₂O	Yes	1035 ⁺²⁸⁵ ₋₁₈₂	*H₂O, *CO, *CH₄	1839 ± 21	Not Inverted
KELT-1 b	None	Featureless	Unknown	FeH, VO	2913 ± 300	Inverted
KELT-7 b	H₂O, H⁻	No	1354 ⁺²⁴³ ₋₂₆₃	*CH₄, *TiO, *VO, H⁻	2480 ± 105	Inverted
KELT-9 b	TiO, VO, FeH, *H⁻	4011 ± 367	Inverted
Kepler-13A b	H₂O	2754 ± 316	Not Inverted
TrES-3 b	None	1668 ± 114	Inverted
WASP-4 b	None	1842 ± 265	Not Inverted
WASP-12 b	H₂O	Yes	2003 ⁺²⁶⁶ ₋₂₈₉	*CO₂	3114 ± 179	Inverted
WASP-18 b	None	Featureless	Unknown	H₂O, H⁻	2841 ± 174	Inverted
WASP-19 b	H₂O	No	1313 ⁺⁴¹⁸ ₋₂₈₄	H₂O	2535 ± 221	Not Inverted
WASP-33 b	H₂O, TiO, H⁻	2600 ± 402	Inverted
WASP-43 b	H₂O	No	564 ⁺¹⁴⁷ ₋₁₄₀	*H₂O, *CO₂	1701 ± 54	Not Inverted
WASP-74 b	<i>H₂O, CH₄</i>	Yes	650 ⁺⁵²¹ ₋₃₂₉	*H₂O, *CH₄	2212 ± 101	Not Inverted
WASP-76 b	H₂O	Yes	2267 ⁺²⁶⁷ ₋₃₀₉	H₂O, TiO	2478 ± 159	Inverted
WASP-77 A b	H₂O, TiO, *CH₄, *CO₂	2015 ± 210	Not Inverted
WASP-79 b	H₂O, H⁻	No	1105 ⁺⁴¹⁰ ₋₂₇₅	<u>VO, FeH</u>	1965 ± 219	Inverted
WASP-103 b	VO, TiO	No	1988 ⁺⁴⁹⁹ ₋₃₉₉	<i>VO, FeH, *CO₂, *H⁻</i>	2937 ± 129	Inverted
WASP-121 b	H₂O, H⁻	No	1386 ⁺³⁴⁰ ₋₃₆₆	*TiO, VO, H⁻	2602 ± 53	Inverted

Note. The colors reflect how trustworthy molecular detections are by comparing the Bayesian evidence to simpler models, $\Delta \ln(E)$. Bold: decisive evidence (e.g., $\Delta \ln(E) > 5$); underlined: strong evidence (e.g., $\Delta \ln(E) > 3$); italic: tentative evidence (e.g., $\Delta \ln(E) > 1$). Molecules that are only detected when Spitzer is added are marked with a star symbol (*). We also report if clouds were found at the planet’s terminator, and we indicate the retrieved temperature. The stated temperature is the retrieved atmospheric temperature, weighted by the contribution function. This temperature is not equal to the temperature obtained by the simpler blackbody fit, which we provide in the individual planet analyses in Appendix D.

as WASP-43 b, may exhibit H₂O features in absorption (around 1.4 μm) and a steep increase in the spectrum toward longer wavelengths. Hotter planets, such as WASP-121 b, show emission features from optical absorbers (from 1.1 to 1.4 μm) and their near-infrared spectra are more leveled.

While a detailed analysis of each planet is provided in Appendix D, we summarize our key findings in Table 1. The data products, including spectra, reduction, and retrieval files, for this article can be found at https://github.com/QuentChangeat/HST_WFC3_Population. Overall, after inspecting the retrieval results of our selected sample of 25 planets, we find that the HST-only spectra are difficult to interpret using free retrievals, as these may also converge to unphysical solutions. This behavior can be explained by the narrow wavelength range covered by HST (see Appendix C), which leads to large degeneracies and does not support the complexity of an emission model where both the thermal profile and atmospheric chemistry have to be disentangled. When Spitzer-IRAC observations at 3.6 and 4.5 μm are included, the thermal profiles can be retrieved more easily. In this case, a free chemical retrieval that includes only H₂O, CO, CO₂, and CH₄ (reduced model) does not fit well the entire population of exoplanets. To improve our fit, we have to include other plausible absorbers such as refractory species (TiO, VO, and FeH) and H⁻ (full model). These species are referred to as optical absorbers throughout this work. When Spitzer data are considered, the full model obtains the highest Bayesian evidence (Jeffreys 1961), $\ln(E)$, compared to a simple

blackbody fit or a reduced model. The full model is rejected in only one case, i.e., HD 209458b (this case is developed further in Appendix B and in the planet’s section). Equilibrium chemistry is expected to be a relatively valid assumption to describe planets in the 1000–2000 K range. However, atmospheric retrievals following equilibrium chemistry, while not strongly rejected by the Bayesian evidence (e.g., $\Delta \ln(E) < 3$), are almost never favored as the best solutions. Possibly, subtle departures from equilibrium chemistry may be better captured by the free retrievals. Another possibility could be that the elemental abundances of refractory elements (Ti, V, and Fe), for which their ratios (Ti/O, V/O, and Fe/O) remain solar in our equilibrium tests, are enhanced (see key question 5 below).

Combining HST and Spitzer observations should be done carefully as it can introduce biases in retrievals (Yip et al. 2021). We tested the robustness of our conclusions by including offsets in the Spitzer data or artificially increasing the photometric uncertainties. We find that while planets can be affected individually, our results on the entire population remain unchanged.

The transit observations and their associated fits are reported in Figure A1 of Appendix A. At the terminator, water vapor is recovered most of the time, independently from the planet’s atmospheric temperature. There, atmospheric clouds are also detected on many planets. Concerning the key open questions listed in the Introduction, focusing more on the results of the full model with HST+Spitzer, we find that:

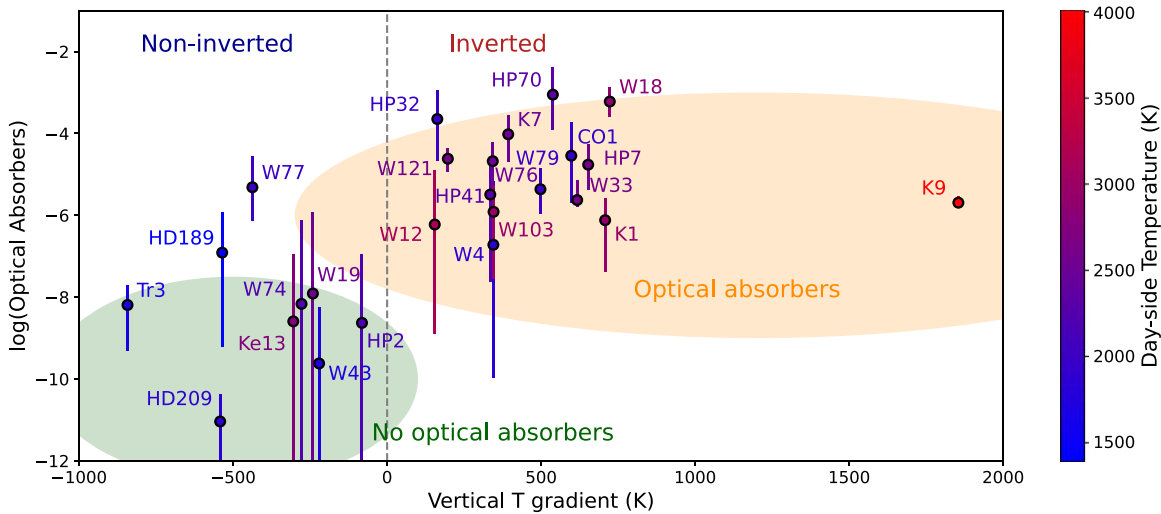


Figure 2. Correlations between the retrieved abundances of optical absorbers (TiO, VO, FeH, and H^-) and the thermal gradient in the atmosphere. The optical absorber abundances are estimated using the weighted average of the individually retrieved abundances for the detected molecules. If no optical absorber is detected, only an upper limit is available. The thermal gradient is the difference between atmospheric temperatures at 5% and 95% of the atmospheric contribution function. Colors on the data points represent averaged retrieved temperatures. Overall, planets with inverted thermal profiles have temperatures above 2000 K and possess optical absorbers (shaded orange region). Planets without thermal inversions have temperatures below 2500 K and do not possess optical absorbers (shaded green region).

(1) Refractory molecules and H^- correlate with thermal inversions.

We show in Figure 2 the weighted mean abundances of optical absorbers (TiO, VO, FeH, and H^-) as a function of the retrieved thermal gradient in the atmospheres of all the planets. Maps displaying the retrieved abundances for each individual species as a function of the atmospheric temperature are available in Appendix A (Figures A3–A6). We see in Figure 2a clear correlation between the retrieved abundances of optical absorbers and the retrieved vertical thermal gradients: Planets with positive thermal gradients show features associated with optical absorbers. While correlation does not imply causation, refractory elements (here TiO, VO, and FeH) and H^- are efficient absorbers of stellar light. In the hottest atmospheres ($T > 2000$ K), refractory elements are thermally stable and can remain in the gas phase. They could therefore provide a natural explanation for thermal inversions. At even higher temperatures, H_2 is thermally dissociated, leading to abundant H^- opacity. H^- also absorbs in the visible and could be another contributor to the retrieved thermally inverted profiles.

(2a) Spectra of the hottest exoplanets do not resemble blackbodies.

Figure 1 demonstrates that the hottest planets in our sample show features associated with molecular species. This is also confirmed by the Bayesian evidence of retrievals including absorbing species as opposed to featureless blackbody curves as shown in the complementary Figure A2 of the Appendix). The presence of refractory elements leads to spectral features that make the spectra deviate from the pure blackbody.

(2b) Dissociation processes do occur in the hottest atmospheres.

Our results also confirm the presence of dissociation processes in the hottest atmospheres: Figure 3 indicates the apparition of H^- opacity from the dissociation of H_2 and H_2O . The trend appears to be driven by the retrieved atmospheric temperature: H_2O is detected in the spectra of cooler atmospheres (high C/O and solar HJ) and H^- becomes more dominant for atmospheres hotter than 2500 K (ultra HJ). As

demonstrated by the different shaded regions of this figure, the metallicity and C/O impact the transition from nondissociated to thermally dissociated regimes. Additional figures are available in Appendix A, showing the temperature dependence for each of the investigated molecules.

(3) The day–terminator contrast of exoplanets does not appear to correlate with temperature and/or dissociation.

In Figure A7 we compare the atmospheric temperature on the dayside, as retrieved from eclipse spectra, and the atmospheric temperature at the terminator, as retrieved from transit spectra, to the estimated equilibrium temperature. Overall, we find that the dayside is about 20% hotter than the equilibrium temperature, while the terminator is about 30% cooler as also expected from theoretical studies (Cho et al. 2003; Parmentier & Crossfield 2017; Tan & Komacek 2019). We observe some scatter across the population in the recovered temperature (see Figure A7 in the Appendix), which could be explained by uncertainties in the observation, intrinsic variability in the population, or atmospheric temporal variability (Cho et al. 2003, 2015; Komacek & Showman 2020; Skinner & Cho 2021a, 2021b; Cho et al. 2021). Our retrieved temperature at the terminator is compatible with the predicted temperatures from general circulation models (GCMs) at the nightside. This confirms potential biases of transit observations toward lower retrieved temperatures, most likely due to 3D effects or the presence of clouds (Caldas et al. 2019; MacDonald et al. 2020; Pluriel et al. 2020; Skaf et al. 2020).

The presence of H^- on the dayside does not appear to be correlated with an increase in the day–terminator thermal gradient, as seen in Figure 4. For instance, for CoRoT-1 b, the terminator is found to be hotter than the dayside. While our results have large uncertainties, our study cannot confirm that the dissociation and recombination of H_2 have large effects on the day–terminator contrast (Tan & Komacek 2019; Roth et al. 2021), as demonstrated in other observational studies. To our knowledge, the only planet for which such effect has been reported is KELT-9 b (Mansfield et al. 2020b), but given the

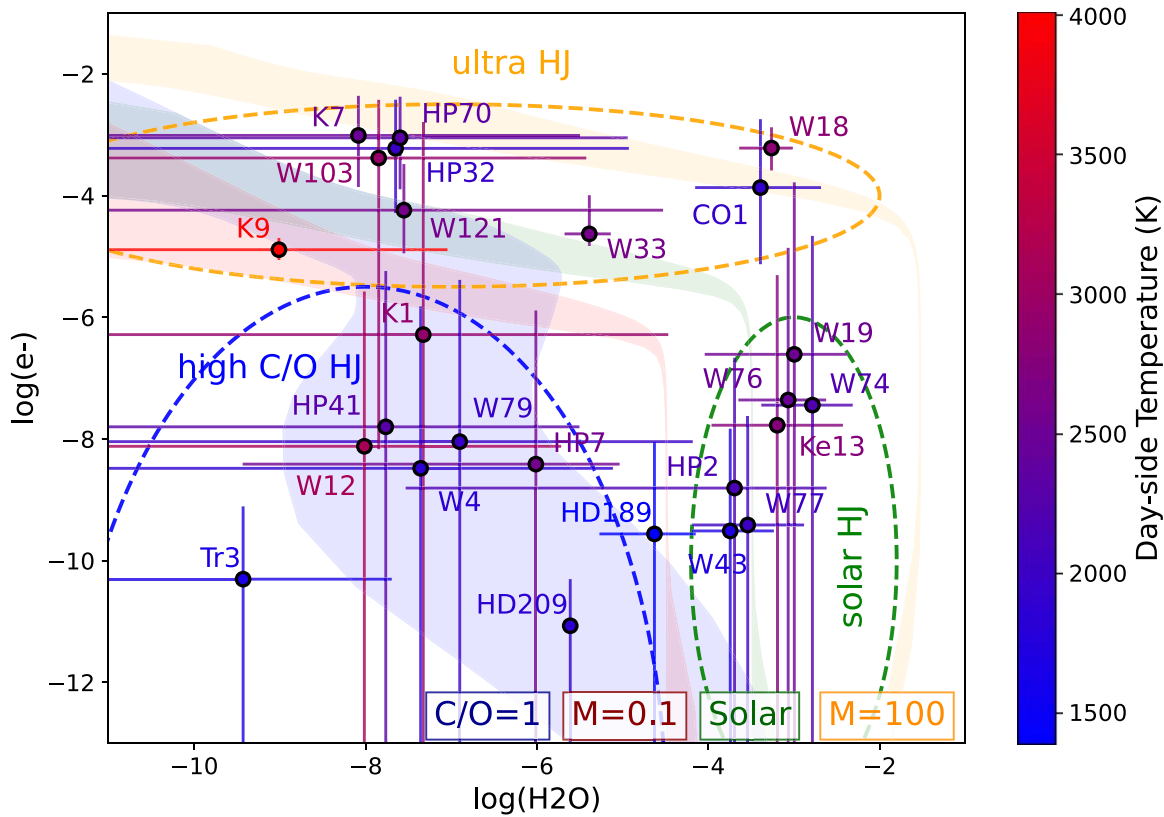


Figure 3. Retrieved abundances of e^- vs. H_2O at the dayside in our sample of 25 hot Jupiters recovered in the HST+Spitzer full runs. The colors on the data points indicate the retrieved atmospheric temperatures weighted by the contribution functions with the legend in the color bar. The shaded green region indicates the predicted abundances from equilibrium chemistry at solar metallicity ($M = 1$) and C/O ($C/O = 0.55$) between 1 bar and 0.01 bar, which is around the region probed by the observations. In orange, the metallicity is increased to 100 times solar. In red, the metallicity is decreased to 0.1 times solar. In blue, the metallicity is solar, and the C/O is increased to 1. The planets separate into three regimes: A solar hot-Jupiter regime where water vapor is detected in moderately hot atmospheres associated with a decreasing thermal profile (dashed green), an ultra-hot-Jupiter regime where thermal inversions and H^- emission are detected in very hot atmospheres (dashed orange), and a high- C/O hot-Jupiter regime where temperatures remain moderate but where water is not detected (dashed blue).

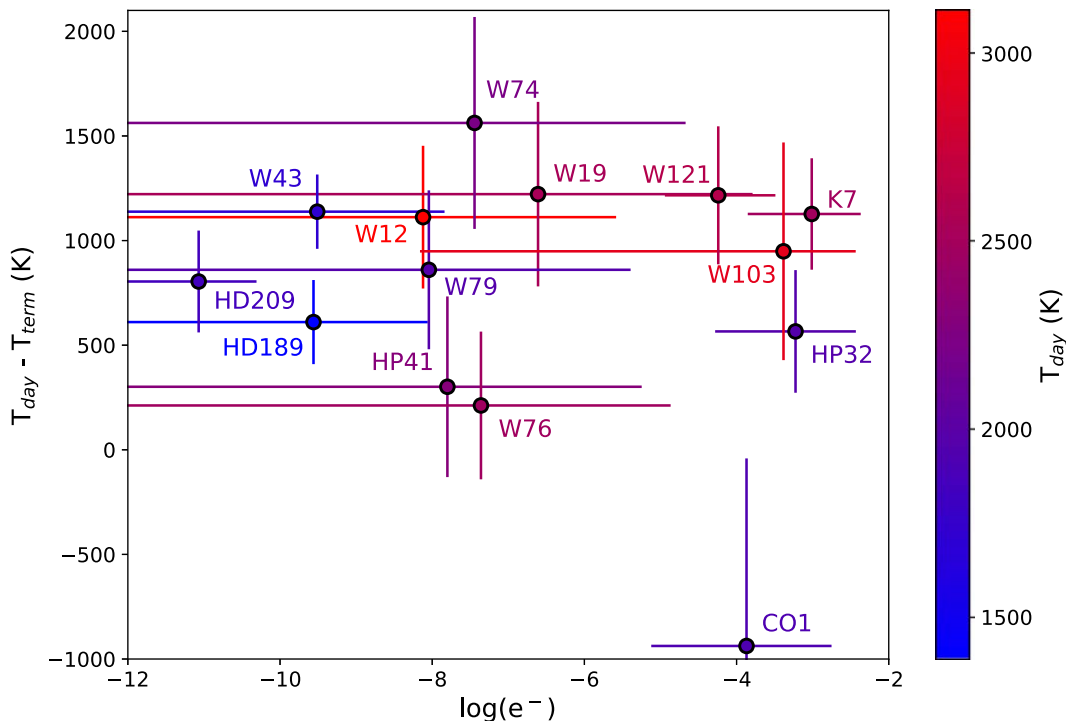


Figure 4. Day-terminator thermal gradient as a function of the e^- abundance recovered using the free retrievals. Only planets that have both eclipse and transit spectra and for which the terminator temperature is constrained are shown in this plot.

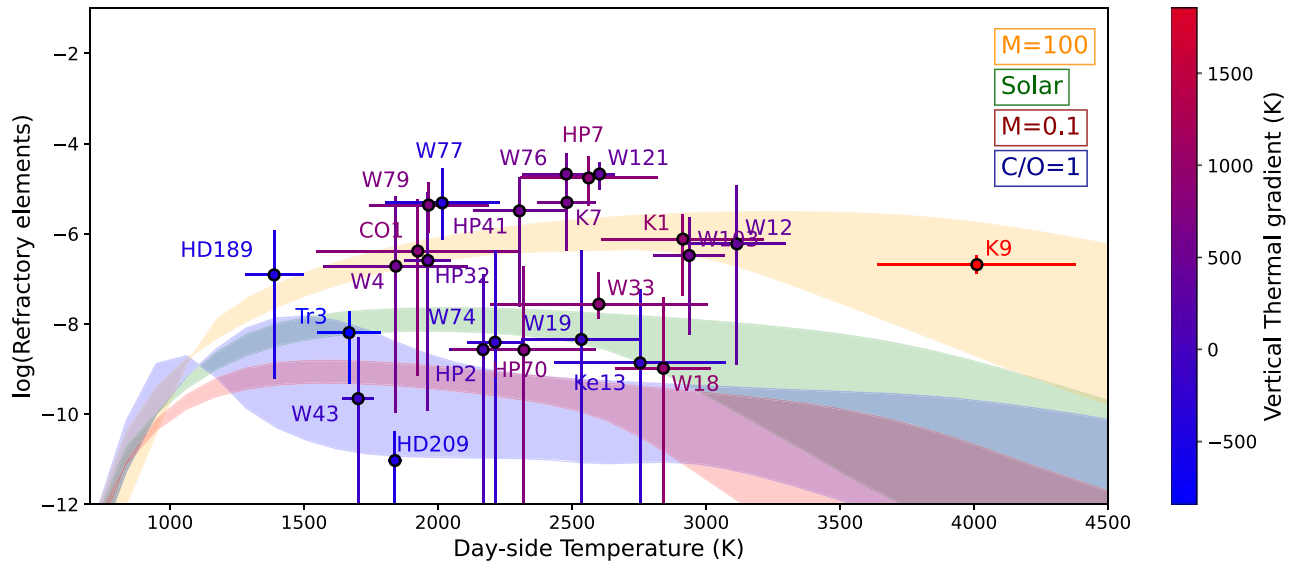


Figure 5. Averaged refractory element (TiO, VO, and FeH) abundances recovered in the HST+Spitzer full runs, weighted by their standard deviation, and plotted against the retrieved atmospheric temperature on the dayside. Green area: predictions from a solar composition and equilibrium chemistry between 1 bar and 0.01 bar. Orange area: the metallicity is assumed to be 100 times solar. Red area: the metallicity is assumed to be 0.1 times solar. Blue area: the metallicity is solar and C/O is assumed to equal 1.

fact that we do not have transit observations for this planet, we are unable to verify this claim.

(4) Planets have solar to subsolar water vapor abundances, which suggest two reservoirs for planet formation.

In most studies, the metallicity and C/O of exoplanets are inferred from the detection of water vapor and C-bearing species, or from chemical equilibrium. Here, we demonstrate that for the coolest planets, water vapor—if detected—can be used as a proxy for metallicity, allowing us to estimate the O/H ratio. This is shown in Figure A8, where the estimated metallicity from O/H is consistent with the equilibrium retrievals (see the inset). For these planets, the chemistry of H₂O is relatively well understood and should be well described by chemical equilibrium. For the hotter planets ($T > 2500$ K), water vapor dissociates, as shown in point (2), and H₂O becomes a poor indicator of the planet’s metallicity. In many cases, inferring metallicity and C/O from water only is degenerate. We attempted to constrain the abundances of the carbon-bearing species and estimate C/O from our free retrievals. At the equilibrium, CH₄ is predicted to be scarce in hot atmospheres, while CO should be the main carbon carrier. We detected evidence of CO only in HD 209458b. Instead, in a few instances, such as in WASP-43 b or HAT-P-7 b, we found evidence for high abundances of CO₂. These detections are likely driven by the stronger absorption of CO₂ in the 4.5 μ m Spitzer channels and its additional absorption at 1.5 μ m. We note that, except for HAT-P-7 b, performing retrievals without CO₂ in the cases where it is detected leads to the detection of CO instead, albeit with a slightly lower Bayesian evidence ($\Delta \ln(E) < 5$). As such, we believe the recovered abundance for CO₂ is not reliable and might here be overestimated.

While directly inferring the C/O from C-bearing species remains difficult, the abundance of water vapor also affects this parameter, which is shown in Figure 3 by the blue shaded region. In this figure, three regimes are identified. The first regime (orange dashed line) includes the hottest planets for which H⁻ is detected. We label those as ultra HJ. For cooler

planets, two reservoirs exist. The first reservoir (green dashed line) contains planets for which water vapor is detected. The recovered abundances are roughly consistent with solar predictions (see also Figure A3). There are exceptions, such as HD 189733b and HD 209458b, for which the data allow us to detect much lower water abundances. Note also that WASP-18 b and CoRoT-1 b have water abundances that are consistent with solar, but those planets also present a particularly high dissociation. The third reservoir (blue dashed line) encompasses planets that do not show the spectral feature of H₂O and H⁻. The nondetection of water in those planets could be due to either a depletion of the molecule or other molecules/clouds masking the water signal. If these atmospheres are indeed depleted of H₂O, as also suggested in previous studies (Madhusudhan et al. 2014; Pinhas et al. 2019; Welbanks et al. 2019), this provides strong constraints on the metallicity and C/O. The depletion could be explained by either an overall subsolar metallicity or, alternatively, a high C/O (see the blue region in Figure 3). When this information is combined with point (5), we argue that the latter is more probable. At present, the bulk metallicities and C/O of exoplanets are difficult to constrain from HST and Spitzer data only, partly due to the limited amount of tracers that our observations are sensitive to. Future telescopes will have the potential to characterize the metallicity and C/O for exoplanets very accurately and confirm these predictions.

(5) A contradiction exists between the abundances of volatiles and refractory elements.

For the hotter planets, we can constrain refractory elements from the abundance of metal oxides and hydrides. As their individual abundances could be unreliable due to their overlapping features, we show in Figure 5 their averaged retrieved abundances weighted by standard deviation. Shaded regions demonstrate that refractory species (TiO, VO, and FeH) are expected to condensate at cooler temperatures ($T < 1300$ K) and thermally dissociate for temperatures higher than 3500 K. For intermediate temperatures, they can exist in a gaseous form and be detectable. For planets hotter than 2500 K, at least one

metal oxide/hydride is present and, interestingly, the recovered weighted abundance is higher than the one predicted from equilibrium chemistry for solar-metallicity values. However, it is compatible with 100 times solar. While we cannot entirely exclude systematic errors from missing molecules in our retrievals or other biases arising from model assumptions, this result contradicts our estimates of the metallicity from water vapor, which suggested solar to subsolar water abundances (see Figure 3). If confirmed, our result suggests that the water depletion identified here and found in previous studies would come from a depletion in oxygen rather than an overall subsolar metallicity, which would have strong implications for planetary formation. We note that a recent study (Welbanks et al. 2019) reached the same conclusion when using alkali as secondary tracers of metallicity, which were also found to have supersolar abundances.

4. Discussion and Conclusion

We have presented here the first retrieval population study of exoplanet atmospheres observed in eclipse with the Hubble and Spitzer Space Telescopes. Our sample includes 25 hot gaseous planets. When combining the HST data with the available Spitzer data, the trends in our population are stable to changes of ± 100 ppm in the Spitzer data and an increase of observed noise by a factor of 2. Overall, we have found that:

1. The coolest planets in our sample ($T < 2000$ K) have noninverted thermal profiles with signatures of water absorption.
2. The hottest planets in our sample ($T > 2000$ K) have inverted thermal profiles with signatures from thermal dissociation (H^-) and refractory species (TiO , VO , or FeH). Their spectra in the HST wavelength range are not consistent with a simple blackbody emission.
3. The dayside–terminator thermal gradient is not found to be correlated with equilibrium temperature or H^- opacity.
4. Metallicity and C/O are difficult quantities to constrain from free retrievals of current data. Our results suggest water abundance is solar to subsolar in the sample analyses. If confirmed, this result would have important implications for planet formation.
5. Metal oxides and hydrides are found in excess of solar abundances in the hotter planets, thus contrasting with our results on the water abundances. If confirmed, this result would inform our current understanding of giant planets' formation.
6. For a number of planets in our sample, equilibrium chemistry retrievals are not the preferred solution. While we cannot strongly reject equilibrium chemistry, this suggests that disequilibrium mechanisms might be important and highlight the importance of carrying unbiased free retrieval approaches.

Population studies, such as the one presented here, pave the way for future studies based on the next generation of space telescopes. In the next decade, James Webb Space Telescope (JWST) (Gardner et al. 2006), Twinkle (Edwards et al. 2019b), and Ariel (Tinetti et al. 2018, 2021) will provide atmospheric data for thousands of diverse worlds, enabling the study of chemical regimes, circulation patterns and formation mechanisms well beyond the parameter space explored here.

This work utilized the OzSTAR national facility at Swinburne University of Technology. The OzSTAR program receives funding in part from the Astronomy National Collaborative Research Infrastructure Strategy (NCRIS) allocation provided by the Australian Government. This work utilized the Cambridge Service for Data Driven Discovery (CSD3), part of which is operated by the University of Cambridge Research Computing on behalf of the STFC DiRAC HPC Facility (www.dirac.ac.uk). The DiRAC component of CSD3 was funded by BEIS capital funding via STFC capital grants ST/P002307/1 and ST/R002452/1 and STFC operations grant ST/R00689X/1. DiRAC is part of the National e-Infrastructure.

The authors wish to thank an anonymous reviewer for providing constructive suggestions that greatly improved the article. Also, the authors wish to thank the AAS Editor and the AAS Data Editor for advising and helping with the presentation of our data and results.

We acknowledge the funding bodies that provided support to this research:

1. European Research Council (ERC), ExoAI 758892: Q.C., B.E., K.Y., I.W.
2. Science and Technology Funding Council (STFC), ST/K502406/1: Q.C., B.E., G.T.
3. Science and Technology Funding Council (STFC), ST/P000282/1: Q.C., B.E., G.T.
4. Science and Technology Funding Council (STFC), ST/P002153/1: Q.C., B.E., G.T.
5. Science and Technology Funding Council (STFC), ST/S002634/1: Q.C., B.E., G.T.
6. Science and Technology Funding Council (STFC), ST/T001836/1: Q.C., B.E., G.T.
7. Science and Technology Funding Council (STFC), ST/P000592/1: JS.
8. UK Space Agency (UKSA), ST/W00254X/1: Q.C.
9. Paris Region Fellowship Programme under the Marie Skłodowska-Curie grant agreement no. 945298: B.E.
10. University College London, UCL Cities Partnership London-Paris: Q.C., B.E., I.W., G.T., O.V.
11. Centre National d'Études Spatiales (CNES): O.V.
12. CNRS/INSU Programme National de Planétologie (PNP): O.V.
13. Agence Nationale de la Recherche (ANR), EXACT ANR-21-CE49-0008-01: O.V.
14. Japan Society for the Promotion of Science (JSPS), KAKENHI JP18H05439: M.I., S.S.
15. Japan Society for the Promotion of Science (JSPS), KAKENHI JP17H01153: M.I.
16. Japan Society for the Promotion of Science (JSPS), Core-to-Core Program, Planet²: M.I., S.S.
17. UK Research and Innovation-Science and Technology Funding Council (UKRI-STFC) studentship: M.F.B.

Q.C. and B.E. contributed equally to this work.

1. Data reduction: B.E., Q.C., A.T.
2. Retrieval analysis: Q.C., B.E., A.A., I.W.
3. Code development (Iraclis, TauREx, Alfnor): Q.C., A.T., A.A., I.W.
4. Scientific interpretation: all authors contributed to the scientific interpretation of the results. Paper redaction: all authors contributed to the redaction of the article.

The authors declare that they have no competing interests.

This work is based upon observations with the NASA/ESA Hubble Space Telescope, obtained at the Space Telescope Science Institute (STScI) operated by AURA, Inc. The raw data used in this work are available from the Hubble Archive which is part of the Mikulski Archive for Space Telescopes. This work is also based in part on observations made with the Spitzer Space Telescope, which is operated by the Jet Propulsion Laboratory, California Institute of Technology, under a contract with NASA. We are thankful to those who operate these telescopes and their corresponding archives, the public nature of which increases scientific productivity and accessibility (Peek et al. 2019).

Our HST reduction pipeline, *Iraclis*,¹² and our atmospheric retrieval code, *TauREx3*,¹³ are publicly available on Github and can be installed from pypi. The chemical code *GGChem*¹⁴ and its plug-in version, compatible with the *TauREx3* framework, are also publicly available. To perform our retrievals on the entire population of 25 exoplanets, we utilized the *Alfnoor* code. While a public version of *Alfnoor* is not yet available, it

uses the *TauREx* retrieval code, ensuring that our results on individual planets can be reproduced. All the data products from this article are available at https://github.com/QuentChangeat/HST_WFC3_Population.

Appendix

This Appendix contains A—Complementary Figures to the Main Article including Figures A1–A8, B—Materials and Methods including Figures B1–B5 and Tables B1–B5, C—Supplementary Text including Figures C1–C2, and D—Individual Planet Analyses including Figures D1–D3 and Table D1.

Appendix A

Complementary Figures to the Main Article

This appendix contains the complementary figures to the main article, Figures A1–A8.

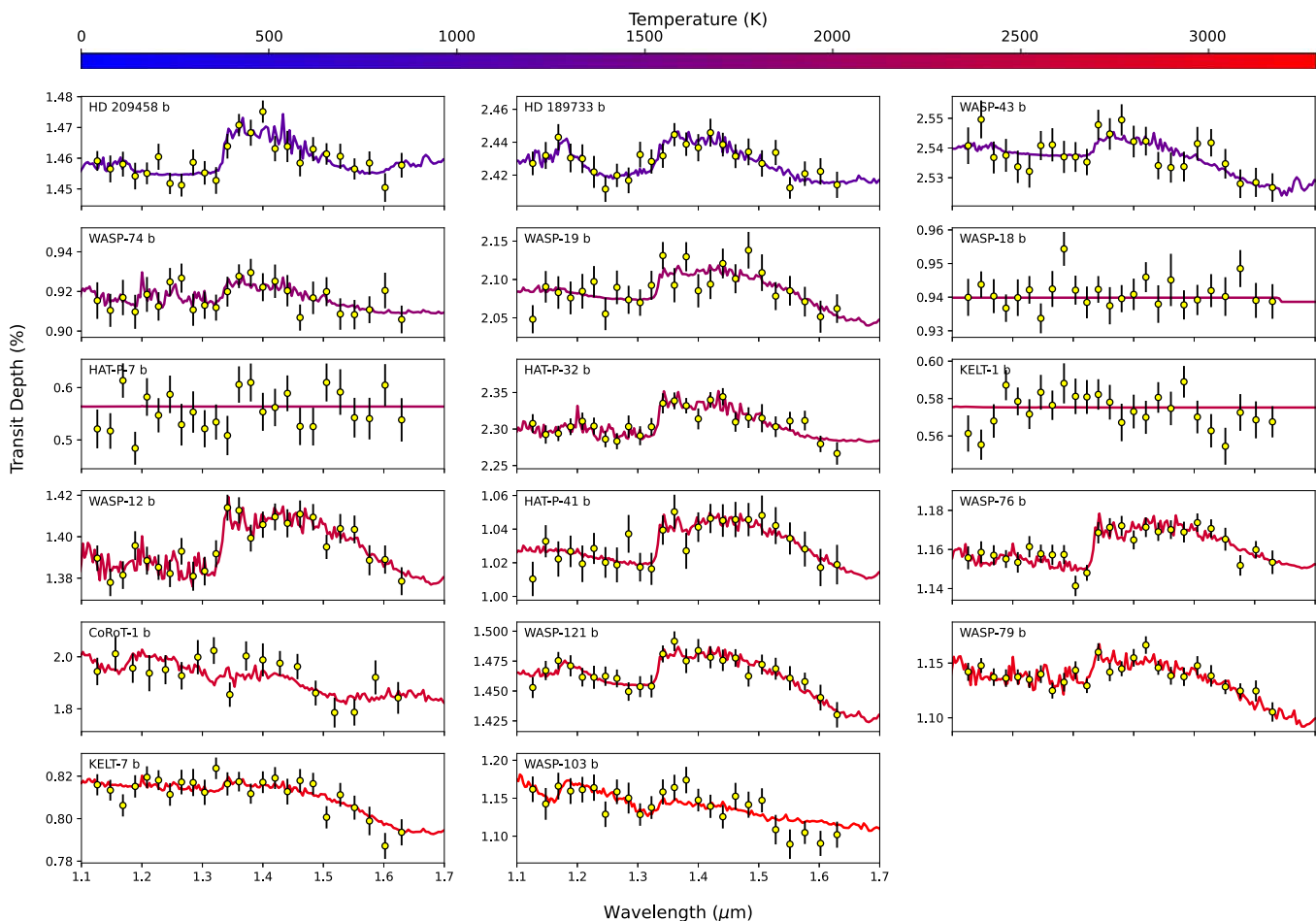


Figure A1. Best-fit spectra of the full runs for the planets observed in transit. The planets are ordered in increasing atmospheric temperatures, which are traced by the colors (from blue to red). Unlabeled x -axes range from 1.1 to 2 μm .

¹² <https://github.com/ucl-exoplanets/Iraclis>

¹³ https://github.com/ucl-exoplanets/TauREx3_public

¹⁴ <https://github.com/ucl-exoplanets/GGchem>

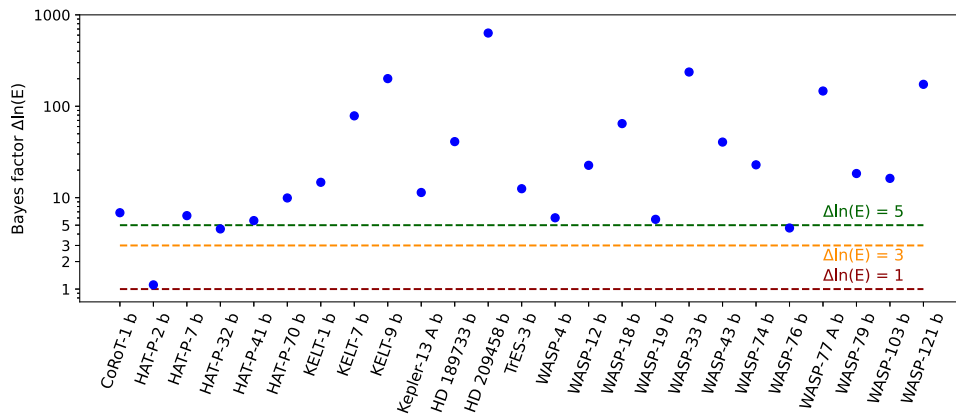


Figure A2. Bayes factor between the full HST+Spitzer retrieval and the blackbody fit for the eclipses. The figure shows that a blackbody is rejected for all planets in the combined data set, except HAT-P-2 b.

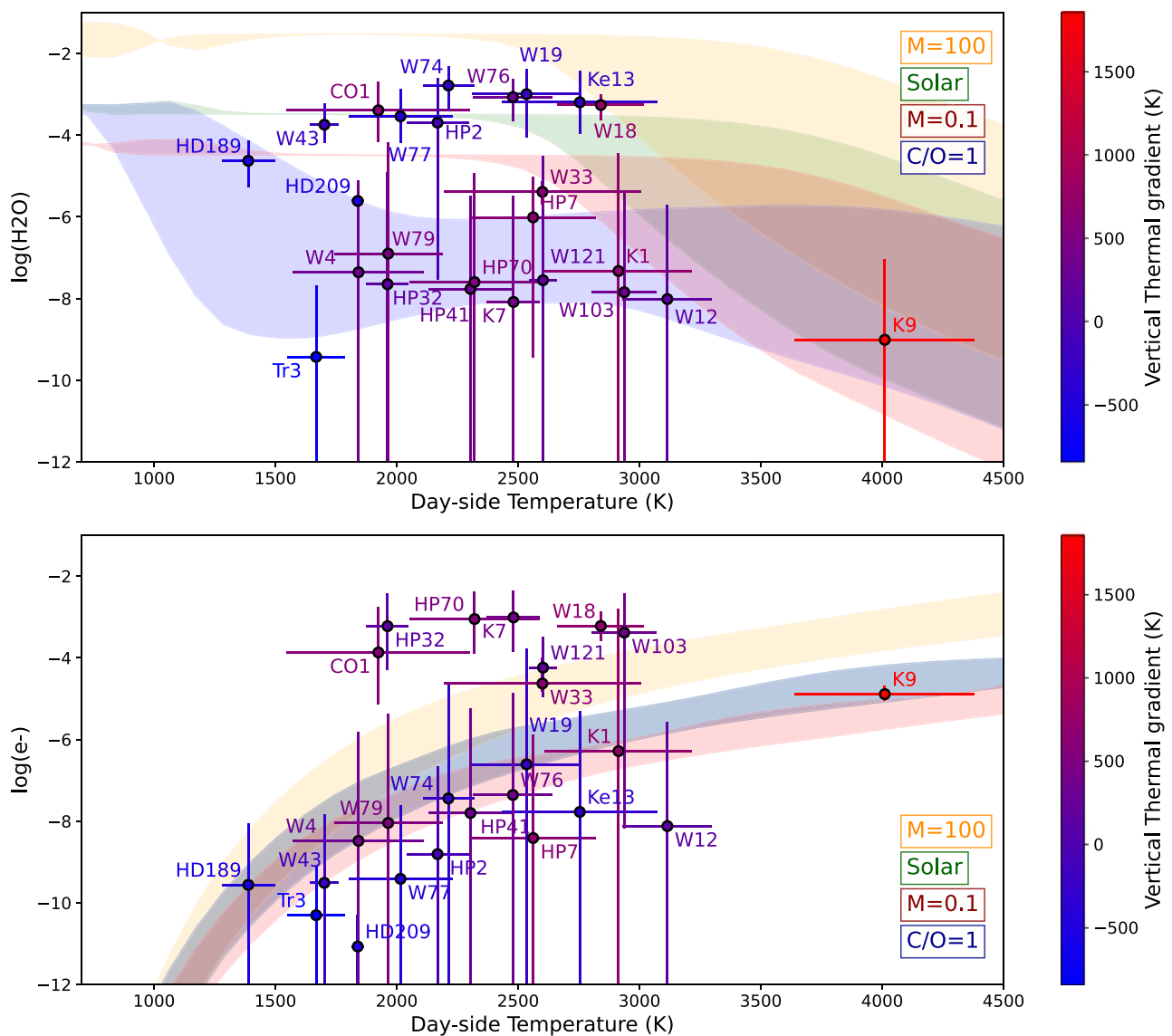


Figure A3. Correlations at the dayside between the H₂O (top) and e⁻ (bottom) abundances and the mean retrieved temperature weighted by the contribution function. The colors indicate the retrieved thermal gradient, defined as the temperature differences between the upper and lower quantiles of the contribution function. The shaded green region is the predicted abundances from equilibrium chemistry at solar metallicity and C/O between 1 bar and 0.01 bar. In orange, the metallicity is increased to 100 times solar. In red, the metallicity is decreased to 0.1 times solar. In blue, the metallicity is solar and the C/O is increased to 1. Note that in the e⁻ plot (bottom), the solar and C/O = 1 cases overlap.

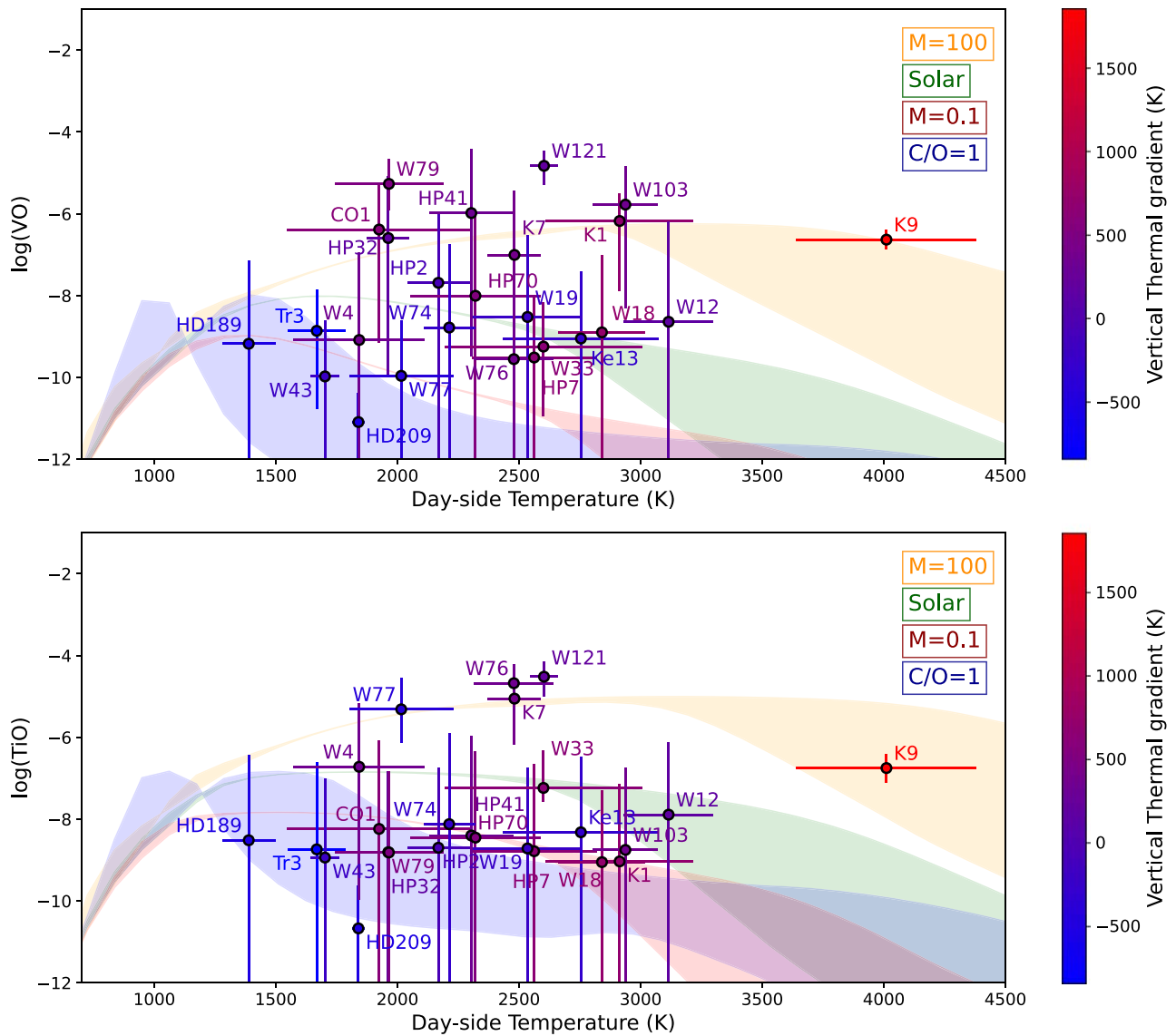


Figure A4. Correlations at the dayside between the VO (top) and TiO (bottom) abundances and the mean retrieved temperature weighted by the contribution function. The colors indicate the retrieved thermal gradient, defined as the temperature differences between the upper and lower quantiles of the contribution function. The shaded green region is the predicted abundances from equilibrium chemistry at solar metallicity and the C/O between 1 bar and 0.01 bar. In orange, the metallicity is increased to 100 times solar. In red, the metallicity is decreased to 0.1 times solar. In blue, the metallicity is solar and the C/O is increased to 1.

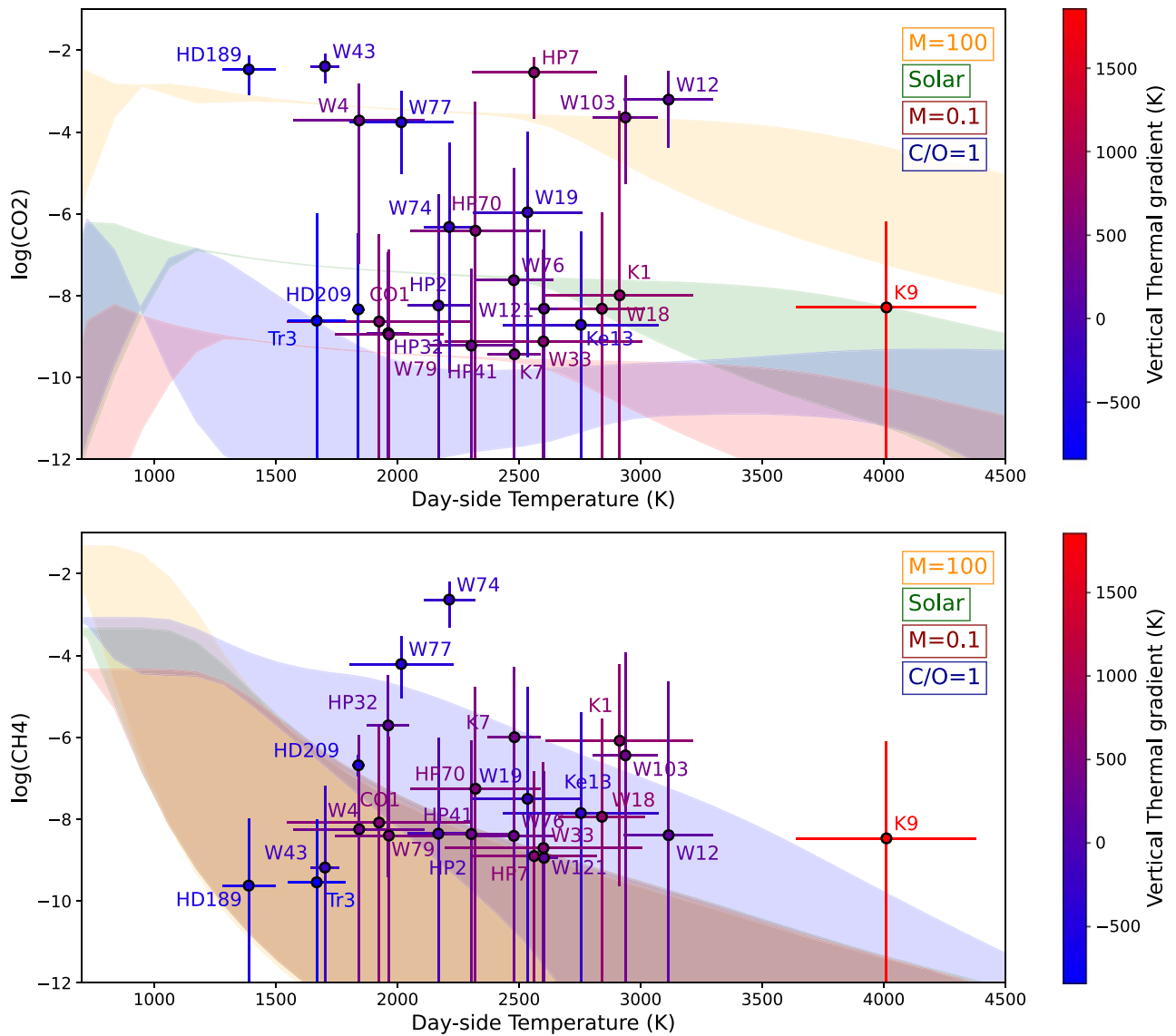


Figure A6. Correlations at the dayside between the CO₂ (top) and CH₄ (bottom) abundances and the mean retrieved temperature weighted by the contribution function. The colors indicate the retrieved thermal gradient, defined as the temperature differences between the upper and lower quantiles of the contribution function. The shaded green region is the predicted abundances from equilibrium chemistry at solar metallicity and the C/O between 1 bar and 0.01 bar. In orange, the metallicity is increased to 100 times solar. In red, the metallicity is decreased to 0.1 times solar. In blue, the metallicity is solar and the C/O is increased to 1.

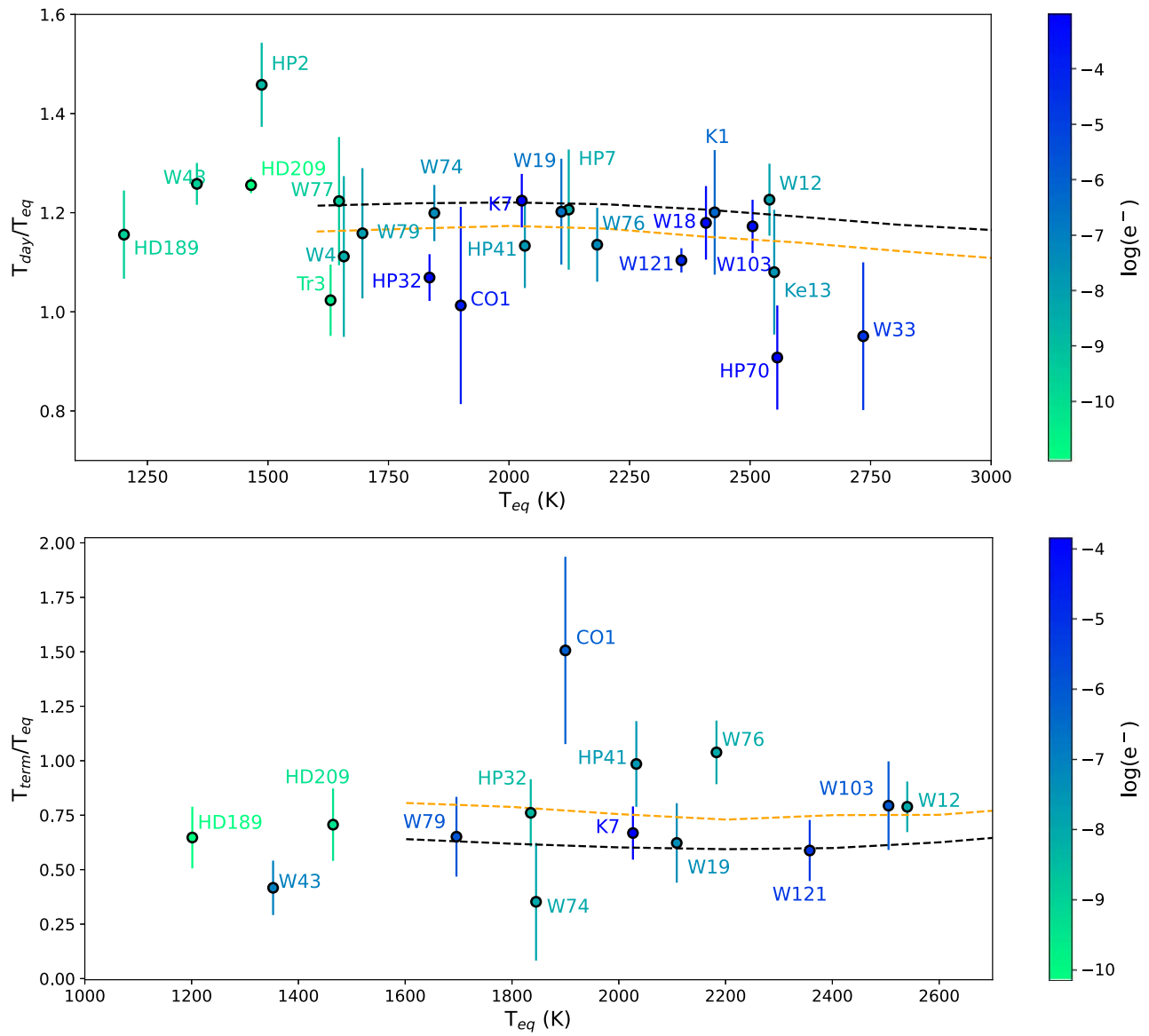


Figure A7. Weighted retrieved atmospheric temperature for the dayside (top) and terminator (bottom) as a function of the planet’s equilibrium temperature. The equilibrium temperature is calculated for a planetary Albedo of 0. The colors correspond to the abundance of e^- , which traces H_2 dissociation. As a reference, we also show in dashed lines the GCM predictions from Tan & Komacek (2019) with H_2 dissociation/recombination included for their slow (orange) and fast (black) drag timescales.

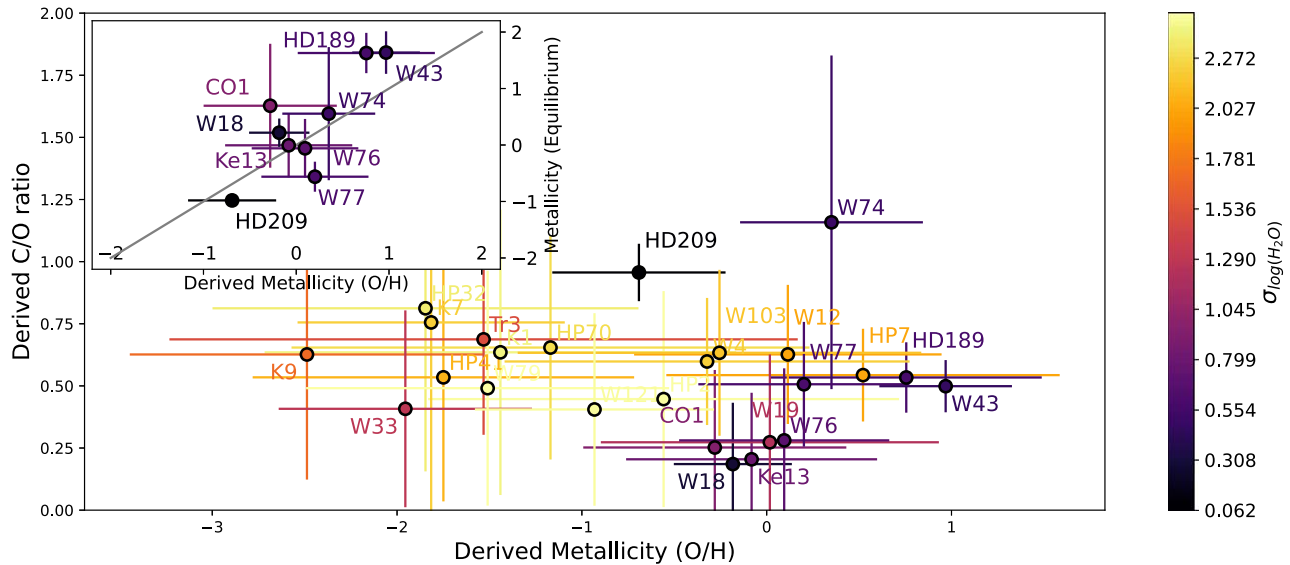


Figure A8. Metallicity (O/H) and C/O recovered from our free-chemistry retrievals. In colors, we highlight the error on the retrieved abundance of water $\sigma_{\log(\text{H}_2\text{O})}$ because only the cases where water is recovered are reliable (purple to black). C/O remains very difficult to constrain because our observations lack sensitivity to carbon-bearing species. In the inset, we show the metallicity derived from free chemistry for the runs with $\sigma_{\log(\text{H}_2\text{O})} < 1$ vs. the metallicity recovered in the equilibrium chemistry cases.

Appendix B Materials and Methods

B.1. Description of the Observations and Their Reduction

For this study, we considered the planets that have been observed in eclipse using the Hubble Space Telescope (HST) WFC3 camera with grism G141. This constitutes a sample of 25 planets. For all planets except HAT-P-70 b, data from the Spitzer Space Telescope are also available for at least the 3.6 and the 4.5 μm IRAC channels. When available, we also reanalyzed the complementary HST-WFC3 data from transit observations, which is the case for 17 planets in our sample. We describe below our reduction method for the HST observations and the sources for the Spitzer data.

B.1.1. Hubble Space Telescope Data

For all planets, except for Kepler-13 A b and WASP-33 b, we downloaded the publicly available data from the Mikulski Archive for Space Telescopes¹⁵ (MAST). We note that data from HST also exist for the planet CoRoT-2 b, but due to the very shallow eclipse for this planet (Wilkins et al. 2014), we were not able to reliably reduce the observations and chose to not include this planet in the study. The publicly available data consist of a series of raw detector images.

We carried out the analysis of all HST-WFC3 data using Iraclis, our highly specialized software for processing WFC3 spatially scanned spectroscopic images (Tsiaras et al. 2016b), which has been used in a number of studies (Tsiaras et al. 2016c; Damiano et al. 2017; Tsiaras et al. 2018, 2019; Anisman et al. 2020; Changeat et al. 2020b; Edwards et al. 2020; Pluriel et al. 2020; Skaf et al. 2020; Changeat & Edwards 2021; Edwards et al. 2021; Guilluy et al. 2021; Libby-Roberts et al. 2021; Mugnai et al. 2021; Yip et al. 2021). For this study and except for two planets (WASP-33 b and Kepler-13A b), we acquired literature spectral data only if the reduction had been performed with the Iraclis pipeline to

ensure homogeneity between planets. In particular, Tsiaras et al. (2018; hereafter referred to as Tsiaras et al. 2018), already reduced a number of the data sets for the transits we consider here with Iraclis. Else, we performed a reduction process that included the following steps: zero-read subtraction, reference-pixel correction, nonlinearity correction, dark current subtraction, gain conversion, sky background subtraction, calibration, flat-field correction, and bad-pixel/cosmic-ray correction. Then we extracted the white (1.088–1.68 μm) and the spectral light curves from the reduced images, taking into account the geometric distortions caused by the tilted detector of the WFC3 infrared channel.

We fitted the light curves using our light-curve modeling package PyLightcurve (Tsiaras et al. 2016a) with the parameters from Table B1. During our fitting of the white light curve, the planet-to-star flux ratio and the mideclipse time were the only free parameters, along with a model for the systematics (Kreidberg et al. 2014c; Tsiaras et al. 2016b). It is common for WFC3 exoplanet observations to be affected by two kinds of time-dependent systematics: the long-term and short-term “ramps.” The first affects each HST visit and is modeled by a linear function, while the second affects each HST orbit and has an exponential behavior. The formula we used for the white light-curve systematics (R_w) was the following:

$$R_w(t) = n_w^{\text{scan}} (1 - r_a(t - T_0))(1 - r_{b1}e^{-r_{b2}(t-t_o)}), \quad (1)$$

where t is time, n_w^{scan} is a normalization factor, T_0 is the mideclipse time, t_o is the time when each HST orbit starts, r_a is the slope of a linear systematic trend along each HST visit, and (r_{b1}, r_{b2}) are the coefficients of an exponential systematic trend along each HST orbit. The normalization factor we used (n_w^{scan}) was changed to n_w^{for} for upward scanning directions (forward scanning) and to n_w^{rev} for downward scanning directions (reverse scanning). The reason for using separate normalization factors is the slightly different effective exposure times due to

¹⁵ <https://archive.stsci.edu/>

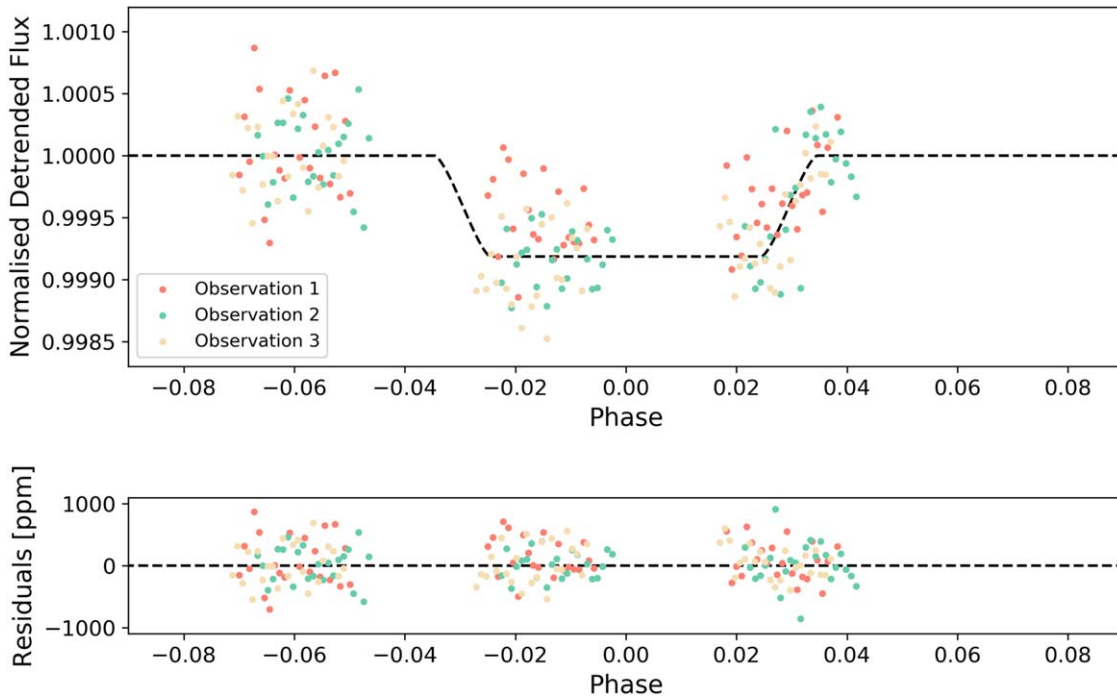


Figure B1. White light-curve fit of CoroT-1 b with Iraclis (top) and residuals (bottom).
(The complete figure set (24 images) is available.)

the known upstream/downstream effect (McCullough & MacKenty 2012).

We fitted the white light curves using the formulae above and the uncertainties per pixel, as propagated through the data-reduction process. However, it is common in HST/WFC3 data to have additional scatter that cannot be explained by the ramp model. For this reason, we scaled up the uncertainties in the individual data points, for their median to match the standard deviation of the residuals, and repeated the fitting (Tsiaras et al. 2018). The white light-curve fits obtained for the eclipse spectra are shown in Figure Set B1.

Next, we fitted the spectral light curves with a transit model (with the planet-to-star flux ratio being the only free parameter) along with a model for the systematics (R_λ) that included the white light curve (divide-white method; Kreidberg et al. 2014c) and a wavelength-dependent, visit-long slope (Tsiaras et al. 2016b):

$$R_\lambda(t) = n_\lambda^{\text{scan}}(1 - \chi_\lambda(t - T_0)) \frac{LC_w}{M_w}, \quad (2)$$

where χ_λ is the slope of a wavelength-dependent linear systematic trend along each HST visit, LC_w is the white light curve, and M_w is the best-fit model for the white light curve. Again, the normalization factor we used (n_λ^{scan}) was changed to (n_λ^{for}) for upward scanning directions (forward scanning) and to (n_λ^{rev}) for downward scanning directions (reverse scanning). Also, in the same way as for the white light curves, we performed an initial fit using the pipeline uncertainties and then refitted while scaling these uncertainties up, for their median to match the standard deviation of the residuals.

We note that several of these data sets were acquired using the staring mode, which is usually less efficient than the spatial scanning technique. Furthermore, the signal-to-noise ratio (S/N) achieved on the eclipse varied between planets. We used the S/N on the white light curve to dictate the resolution of the spectral fitting. For those with an S/N > 7, a high-resolution spectrum was extracted (25 bins) while a lower resolution binning was chosen for all others (18 bins). The recovered spectral light curve for the planets reduced with Iraclis is shown in Figure Set B2.

For planets with multiple visits, we correct for offsets by subtracting each spectrum by the corresponding white light-curve depth, $(F_p/F_\star)_{w,v}^2$, and adding the weighted average eclipse depth of all white light curves, $(F_p/F_\star)_w^2$. Finally, we compute the weighted average from all the eclipse observations, which we use for all subsequent analyses. Due to possible variabilities in the star, the planet, or the instrument systematics, the measured white eclipse depths could change between the different visits, so we choose not to perform a joint fit of these data sets as done in many previous studies (Cartier et al. 2017; Arcangeli et al. 2018; Wakeford et al. 2018). However, except for HD 209458b, when multiple visits are available, the individual eclipse depths are all consistent within 1σ , meaning that a joint fit would be equivalent. For HD 209458b, we show the extracted spectra in Figure B3 along with the final spectrum obtained by averaging all five visits. We note that the spectral features are consistent in the five observations.

While most of our spectra are consistent with the literature, HD 209458b differs significantly from the spectrum derived in Line et al. (2016), as shown in Figure B3. The shape of the spectra is highly similar, but we observe a ~ 160 ppm vertical

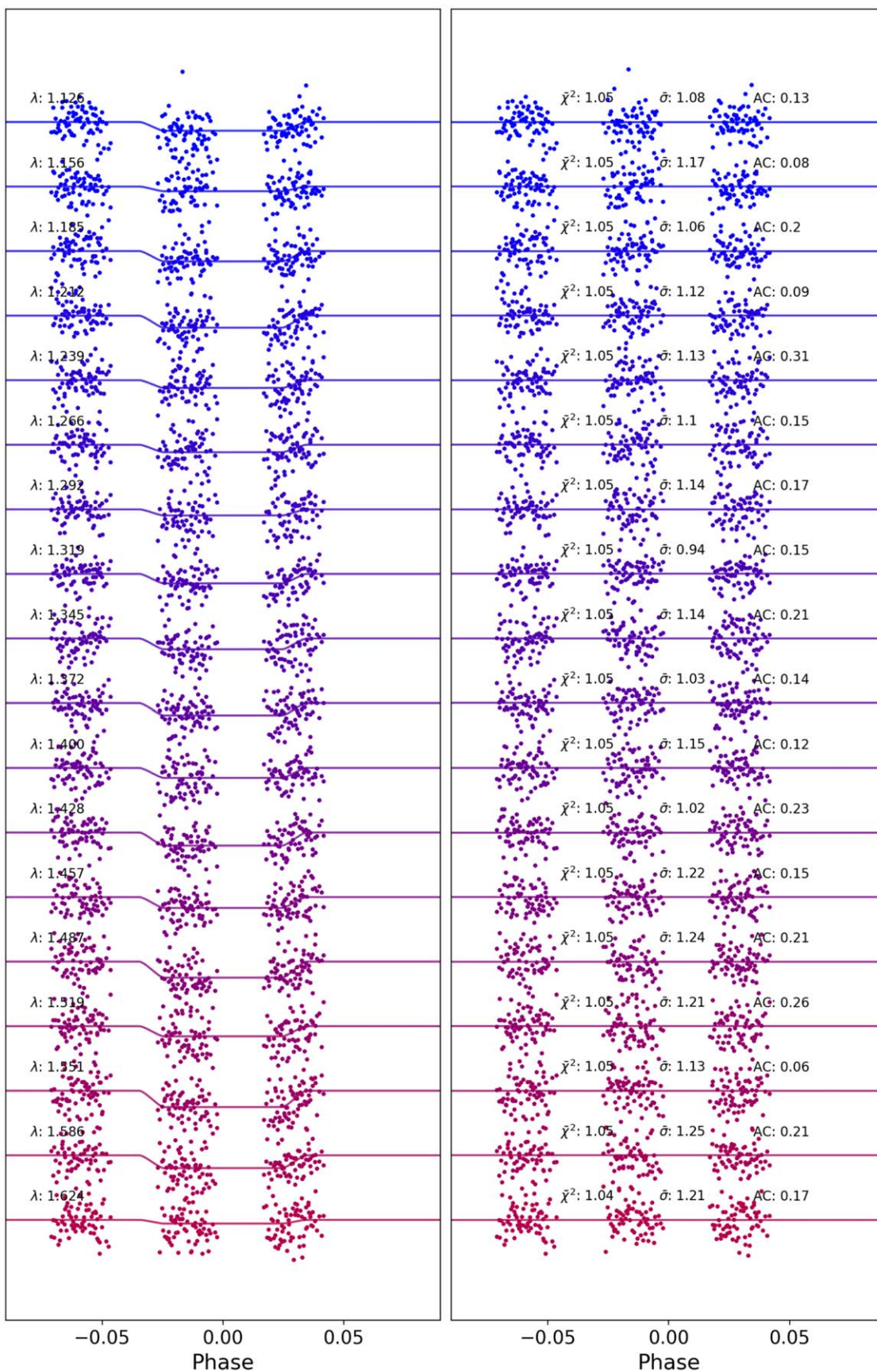


Figure B2. Spectral light curve of CoRoT-1 b obtained with Iraclis.
 (The complete figure set (24 images) is available.)

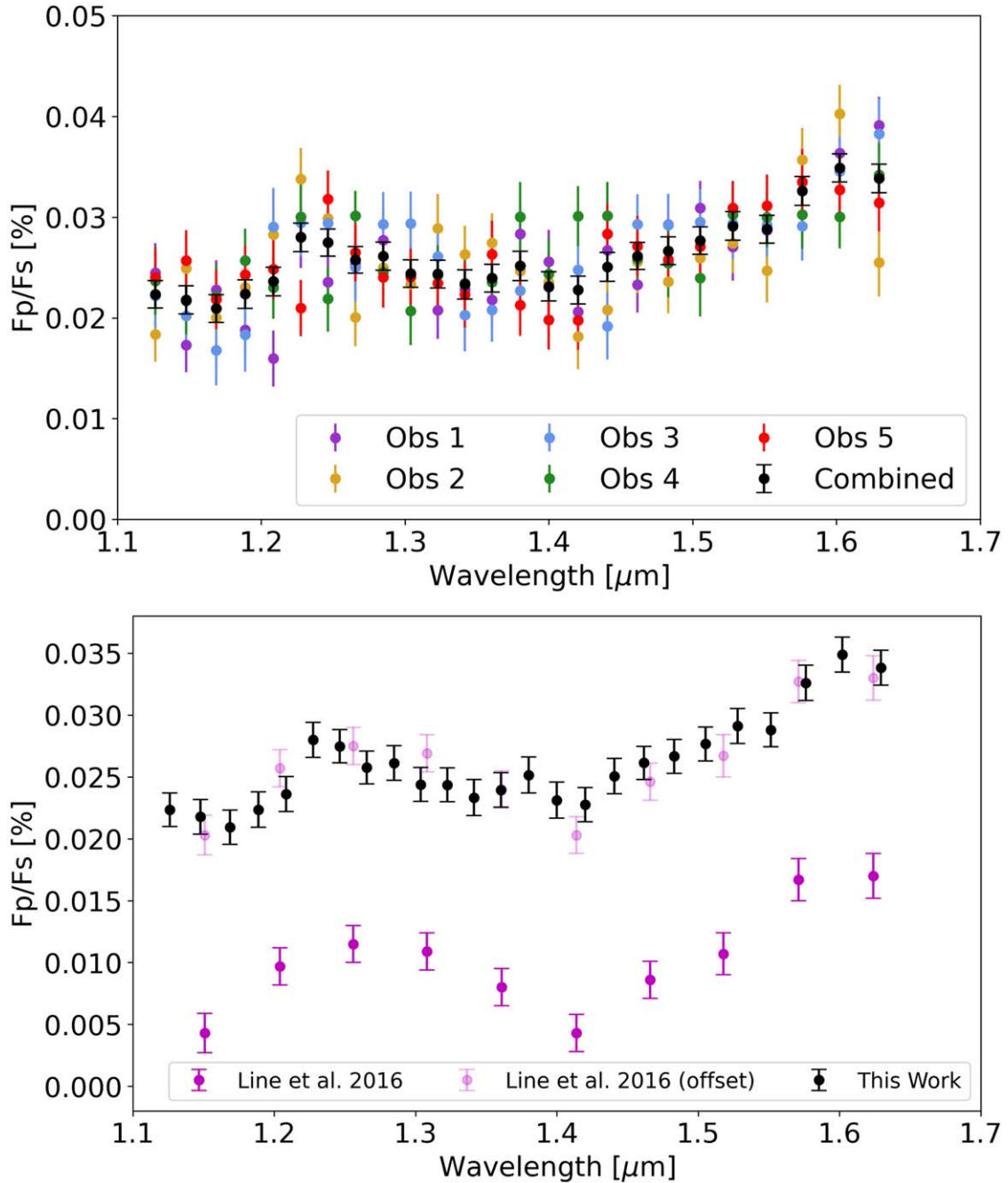


Figure B3. Top: recovered spectra from each visit and the final, averaged spectrum (black). Bottom: comparison of the spectrum recovered here to that of Line et al. (2016). We note that, while the spectra have similar shapes, they are offset by around 0.016% (160 ppm).

offset. We identified that the difference comes from the assumption of a quadratic systematic for the long-term ramp in Line et al. (2016), while we here assume a linear behavior. We note that Line et al. (2016) only managed to fit four of the five eclipse observations while we fitted all five. Additionally, when fitting these observations with a quadratic trend, we found the white light-curve depth, and the associated errors, was far more unstable than the linear fits. The spectral shape recovered with both trends was very similar. HD 209458b is the planet for which the most significant difference from the literature can be observed. Other spectra from the literature are compared to our Iracelis pipeline reductions in Figure Set B4. Overall, we find that except

for HD 209458b and for TrES-3 b, we do not find significant differences in spectral shape and observe only minor offsets.

We also considered the transmission spectra, which are available for 17 planets. These were reduced using the same process as for the emission data.

For two systems, WASP-12 and WASP-103, a close stellar companion contaminated the data from HST-WFC3. For exoplanet spectroscopy, this third light modifies the transit/eclipse depth. To account for this, we used the freely available WFC3 simulator Wayne.¹⁶

¹⁶ <https://github.com/ucl-exoplanets/wayne>

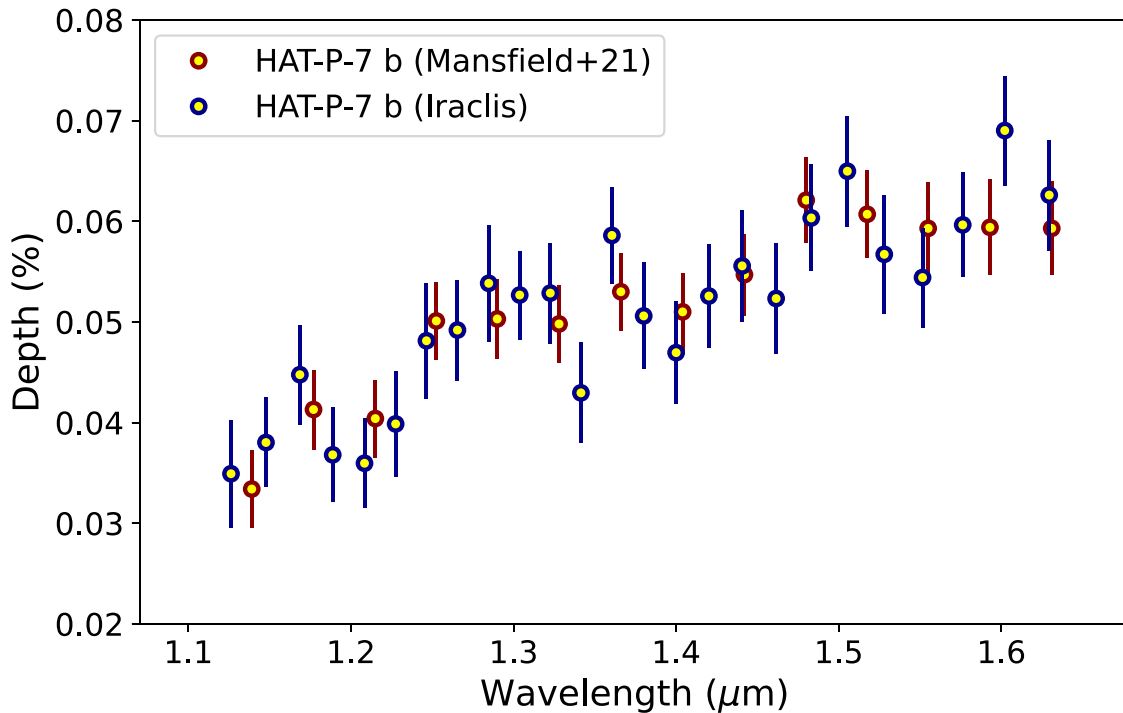


Figure B4. Comparison of the Iraclis final reduction (blue) with the literature for HAT-P-7 b. (The complete figure set (16 images) is available.)

Type	Parameter	Mode	priors
Transmission only	planet radius (R_p)	linear	0.1 - 2.0 (R_J)
	temperature (T)	linear	100 - 4000 (K)
	cloud pressure (P_{clouds})	log	$10^6 - 1$ (Pa)
Emission only	temperature points i (T_i)	linear	100 - 4000 (K)
	pressure points 1 (P_1)	log	$10^6 - 100$ (Pa)
	pressure points 2 (P_2)	log	$10^4 - 0.01$ (Pa)
Both	abundances (H_2O , CH_4 , CO , CO_2 , H^-)	log	$10^{-12} - 0.01$ (VMR)
	abundances (TiO, VO, FeH)	log	$10^{-12} - 10^{-4}$ (VMR)
	Metallicity (Eq)	log	0.1 - 100 (to solar)
	C/O ratio (Eq)	linear	0.1 - 2

Figure B5. List of the free parameters and their uniform priors in the retrievals.

Wayne is capable of producing grism spectroscopic frames, both in staring and in spatial scanning modes (Varley et al. 2017). We utilized Wayne to model the contribution of each companion star to the spectral data obtained. We created simulated detector images of both the main and companion star, using these to extract the flux contribution in each spectral bin of each star. The correction to the spectra is then applied as a wavelength-dependent dilution factor, which is derived as a ratio of extracted flux between the stars. Such an approach has previously been used on WFC3 data, e.g., for WASP-76 b (Edwards et al. 2020).

B.1.2. Spitzer Data

For the Spitzer data, we used the data from the literature directly. For all the planets in our sample, we find that at least the 3.6 and the 4.5 μm channels from the Infrared Array Camera (IRAC) are available. Adding Spitzer data significantly increases the wavelength coverage of our observations but can also lead to biases when the observations are not compatible. This well-

known issue is discussed further in Complementary Text. In order to be as consistent as possible, we prioritized the inclusion of the Spitzer data from the population study of Garhart et al. (2020), later referred to as G20. A few planets possess additional channels from legacy Spitzer observations with the Infrared Array Camera (IRAC: 5.8 and 8 μm channels), the InfraRed Spectrograph (IRS: 16 μm), and the Multiband Imaging Photometer for Spitzer (MIPS: 24 μm). In this case, we add the most complete reduction, which allows us to greatly increase the information content for these planets. For HD 209458b, we took the Spitzer data from Diamond-Lowe et al. (2014). We noted, however, that the 16 μm point used, in fact, refers to the Spitzer-IRS low-spectral-resolution observations (Swain et al. 2008a), which span the wavelength range from 7.46 to 15.25 μm . We therefore chose to include the derived broadband eclipse depth from the original study. In Spitzer, photometric channels are large and can cover entire or multiple broadband molecular features. The shape of the spectral response function is therefore important and has to be accounted for during binning

Table B1
List of the Orbital Parameters Used in This Paper and the Associated Literature References

Planet	R_s	T_s	$\log(g)$	[M/H]	P	a/R_s	e	i	t_{mid}	M_p	Reference
CoRoT-1 b	1.11	5950	4.25	-0.3	1.5089557	4.92	0.0	85.1	2454159.4532	1.03	Barge et al. (2008)
HAT-P-2 b	1.64	6290	4.16	0.14	5.6334729	8.99	0.5171	86.72	2454387.49375	9.09	Pál et al. (2010)
HAT-P-7 b	1.84	6350	4	0.32	2.2047354	4.1545	0.0	83.14	2454954.3585723	1.78	Esteves et al. (2013)
HAT-P-32 b	1.367	6207	4.33	-0.04	2.1500082	5.344	0.159	88.98	2455867.24	0.68	Wang et al. (2019)
HAT-P-41 b	2.05	6390	4.14	0.21	2.694047	5.45	0.0	87.7	2454983.86167	1.19	Stassun et al. (2017) Johnson et al. (2017)
HAT-P-70 b	1.86	8450	4.18	-0.059	2.74432452	5.45	0	96.50	2458439.57519	<6.78	Zhou et al. (2019)
HD 189733b	0.75	5052	4.49	-0.02	2.218577	8.84	0.0	85.69	2458334.990899	1.13	Stassun et al. (2017) Addison et al. (2019)
HD 209458b	1.20	6092	4.28	0.0	3.524750	8.87	0.0	86.78	2454560.80588	0.64	Boyajian et al. (2015) Evans et al. (2015)
KELT-1 b	1.462	6518	4.337	0.052	1.217514	3.60	0.0099	87.8	2455914.1628	27.23	Sivard et al. (2012)
KELT-7 b	1.732	6789	4.149	0.139	2.7347749	5.50	0.0	86.79	2457095.68572	2.88	Gaudi et al. (2017)
KELT-9 b	2.362	10170	4.093	-0.03	1.4811235	3.153	0.0	83.76	2456355.229809	1.28	Bieryla et al. (2015)
Kepler-13A b	1.74	7650	4.2	0.2	1.763588	4.5007	0.00064	86.77	2454953.56596	9.28	Esteves et al. (2015)
TrES-3 b	0.817	5650	4.581	-0.19	1.30618608	6.01	0	81.99	2454538.58069	1.910	Christiansen et al. (2011) Southworth (2011)
WASP-4 b	0.893	5400	4.47	-0.07	1.3382299	5.451	0.0	89.06	2455804.515752	1.186	Bouma et al. (2019)
WASP-12 b	1.657	6360	4.157	0.33	1.0914203	3.039	0.0	83.37	2456176.66825800	1.47	Collins et al. (2017)
WASP-18 b	1.26	6431	4.47	0.11	0.9414526	3.562	0.0091	84.88	2458375.169883	10.4	Shporer et al. (2019)
WASP-19 b	1.004	5568	4.45	0.15	0.788838989	3.46	0.002	78.78	2455708.534626	1.114	Wong et al. (2016)
WASP-33 b	1.444	7430	4.30	0.10	1.2198675	3.68	0.0	87.90	2455507.5222	3.266	Collier Cameron et al. (2010) von Essen et al. (2014)
WASP-43 b	0.6	4400	4.65	-0.05	0.813473978	4.872	0.0	82.1	2455528.868634	1.78	Hellier et al. (2011) Kreidberg et al. (2014b)
WASP-74 b	1.42	5990	4.39	0.39	2.137750	4.86	0.0	79.81	2456506.892589	0.72	Stassun et al. (2017)
WASP-76 b	1.73	6250	4.128	0.23	1.809886	3.9997	0.0	89.9	2456107.85507	0.92	West et al. (2016)
WASP-77 A b	0.955	5500	4.33	0.00	1.3600309	5.40	0	89.4	2455870.44977	1.76	Maxted et al. (2013)
WASP-79 b	1.51	6600	4.226	0.03	3.662392	7.41	0.0	86.1	2456215.4556	0.85	Brown et al. (2017)
WASP-103 b	1.436	6110	4.22	0.06	0.925542	2.978	0.0	86.3	2456459.59957	1.490	Gillon et al. (2014)
WASP-121 b	1.458	6459	4.242	0.13	1.2749255	3.754	0.0	87.6	2456635.70832	1.183	Delrez et al. (2016)

Note. R_s is the star radius in Sun radii. T_s is the star temperature in kelvin. g is the stellar surface gravity in cm s^{-2} . [M/H] is the stellar metallicity in dex, P is the orbital period of the planet in days. a is the semimajor axis. e is the eccentricity. i is the inclination in degrees. t_{mid} is the midtransit time in days. M_p is the planetary mass in Jupiter masses. For HAT-P-70 b only an upper limit on the planetary mass is available.

of the forward model. Spitzer spectral response functions for the IRAC, IRS, and MIPS instruments can be found at the NASA/IPAC Infrared Science Archive.¹⁷

The full list of observations that are considered in the retrievals is provided in Table B2. We detail the spectra recovered from this reduction step in Tables B3 and B4 for, respectively, eclipse and transit observations. The full tables are

available in machine-readable format. In those tables, we also include for convenience the Spitzer data sets that were obtained from the literature. These spectra constitute the inputs of our retrieval analysis, further described in the next section.

B.2. Standardized Retrievals with Alfnor

To analyze the spectra obtained by Iraclis, we perform atmospheric retrievals using the Alfnor tool (Changeat et al. 2020a). Alfnor extends the capabilities of the Bayesian

¹⁷ <https://irsa.ipac.caltech.edu/data/SPITZER/docs/>

Table B2

Summary of the Observations Considered in This Paper. HST: Hubble Space Telescope; Spz: Spitzer Space Telescope

Planet	Type	Instruments	Sources
CoRoT-1 b	Eclipse	HST G141	12181 (Deming)
	Eclipse	Spz 3.6, 4.5	Deming et al. (2010)
	Transit	HST G141	12181 (Deming)
HAT-P-2 b	Eclipse	HST G141	16194 (Desert)
	Eclipse	Spz 3.6, 4.5	Lewis et al. (2013)
HAT-P-7 b	Eclipse	HST G141	14782 (Bean)
	Eclipse	Spz 3.6, 4.5, 5.8, 8	Christiansen et al. (2010)
	Transit	HST G141	12181 (Deming)
HAT-P-32 b	Eclipse	HST G141	14767 (Sing)
	Eclipse	Spz 3.6, 4.5	Zhao et al. (2014)
	Transit	HST G141	14260 (Deming)
HAT-P-41 b	Eclipse	HST G141	14767 (Sing)
	Eclipse	Spz 3.6, 4.5	Garhart et al. (2020)
	Transit	HST G141	14767 (Sing)
HAT-P-70 b	Eclipse	HST G141	16307 (Fu)
HD 189733b	Eclipse	HST G141	12881 (McCullough)
	Eclipse	Spz 3.6, 4.5, 5.8, 8, 16, 24	Charbonneau et al. (2008)
	Transit	HST G141	12881 (McCullough)
HD 209458b	Eclipse	HST G141	13467 (Bean)
	Eclipse	Spz 3.6, 4.5, 5.8, 8, 11.35, 24	Diamond-Lowe et al. (2014); Swain et al. (2008a)
	Transit	HST G141	12181 (Deming)
KELT-1 b	Eclipse	HST G141	14664 (Beatty)
	Eclipse	Spz 3.6, 4.5	Garhart et al. (2020)
	Transit	HST G141	14664 (Beatty)
KELT-7 b	Eclipse	HST G141	14767 (Sing)
	Eclipse	Spz 3.6, 4.5	Garhart et al. (2020)
	Transit	HST G141	14767 (Sing)
KELT-9 b	Eclipse	HST G141	15820 (Pino)
	Eclipse	Spz 4.5	Mansfield et al. (2020b)
Kepler-13 A b	Eclipse	HST G141	Beatty et al. (2017)
	Eclipse	Spz 3.6, 4.5	Shporer et al. (2014)
TrES-3 b	Eclipse	HST G141	12181 (Deming)
	Eclipse	Spz 3.6, 4.5, 5.8, 8	Fressin et al. (2010)
WASP-4 b	Eclipse	HST G141	12181 (Deming)
	Eclipse	Spz 3.6, 4.5	Beer et al. (2010)
WASP-12 b	Eclipse	HST G141	12230 (Swain)
	Eclipse	Spz 3.6, 4.5, 5.8, 8	Campo et al. (2011)
	Transit	HST G141	13467 (Bean)
WASP-18 b	Eclipse	HST G141	13467 (Bean)
	Eclipse	Spz 3.6, 4.5, 5.8, 8	Nymeyer et al. (2011)
	Transit	HST G141	13467 (Bean)
WASP-19 b	Eclipse	HST G141	13431 (Huitson)
	Eclipse	Spz 3.6, 4.5, 5.8, 8	Anderson et al. (2013)
	Transit	HST G141	12181 (Deming) + 13431 (Huitson)

Table B2
(Continued)

Planet	Type	Instruments	Sources
WASP-33 b	Eclipse	HST G141	Haynes et al. (2015)
	Eclipse	Spz 3.6, 4.5	Deming et al. (2012)
WASP-43 b	Eclipse	HST G141	13467 (Bean)
	Eclipse	Spz 3.6, 4.5	Garhart et al. (2020)
	Transit	HST G141	13467 (Bean)
WASP-74 b	Eclipse	HST G141	14767 (Sing)
	Eclipse	Spz 3.6, 4.5	Garhart et al. (2020)
	Transit	HST G141	14767 (Sing)
WASP-76 b	Eclipse	HST G141	14767 (Sing)
	Eclipse	Spz 3.6, 4.5	Garhart et al. (2020)
	Transit	HST G141	14260 (Deming)
WASP-77 A b	Eclipse	HST G141	16168 (Mansfield)
	Eclipse	Spz 3.6, 4.5	Garhart et al. (2020)
WASP-79 b	Eclipse	HST G141	14767 (Sing)
	Eclipse	Spz 3.6, 4.5	Garhart et al. (2020)
	Transit	HST G141	14767 (Sing)
WASP-103 b	Eclipse	HST G141	14050 (Kreidberg) + 13660 (Zhao)
	Eclipse	Spz 3.6, 4.5	Garhart et al. (2020)
	Transit	HST G141	14050 (Kreidberg)
WASP-121 b	Eclipse	HST G102	15135 (Mikal-Evans)
	Eclipse	HST G141	14767 (Sing) + 15134 (Mikal-Evans)
	Eclipse	Spz 3.6, 4.5	Garhart et al. (2020)
	Transit	HST G141	14468 + 15134 (Mikal-Evans)

Note. We used observations from the grisms G102 and G141 aboard HST and photometric channels from 3.6 to 24 μm aboard Spitzer.

retrieval suite TauREx3 (Al-Refai et al. 2021a, 2021b) and automates retrievals to large exoplanet populations. It was first built for simulations in the context of the ESA space mission Ariel (Tinetti et al. 2018, 2021) to enable retrieval studies of the mission’s entire target list (Edwards et al. 2019a), but it can also perform standardized retrievals from any real data observation. We use Alfnor to extract the information content of our planetary atmospheres (chemical composition and temperature structure) separately for the transit and eclipse scenarios. For spectroscopic data, such as those presented here, Bayesian retrievals are the currently most adopted analysis technique to extract unbiased information from atmospheric spectra. Another method that has been used to investigate population trends in a few studies (e.g., Crossfield & Kreidberg 2017; Mansfield et al. 2021) consists of measuring the signal amplitude of the molecules of interest, for instance, water. The technique compares the observed flux in the HST water band, which is defined to be between 1.35 and 1.48 μm , for instance, in Mansfield et al. (2021), with a reference flux taken outside the band to evaluate deviations from the expected signal. Such a method, however, does not rely on a full exploration of the parameter space. More importantly, the method requires the definition of signal and reference bands, both of which can contain additional molecular features as shown in our work. Here, we prefer to extract trends in our

Table B3
List of Eclipse Spectra Used in This Population Study

λ (μm)	$\Delta\lambda$	CoRoT-1b	HD 189733 b	TrES-3 b	WASP-4 b	WASP-12 b
1.1262	0.0308	0.0682 ± 0.0149	0.0101 ± 0.0056	0.0515 ± 0.0209	0.0378 ± 0.0183	0.1547 ± 0.0255
1.1563	0.0293	0.0367 ± 0.0149	0.0038 ± 0.0038	0.0263 ± 0.0188	0.0271 ± 0.0177	0.1492 ± 0.0239
1.1849	0.0279	0.0797 ± 0.0159	0.0123 ± 0.0044	0.0088 ± 0.0137	0.0206 ± 0.0152	0.1612 ± 0.0228
1.2123	0.0269	0.0937 ± 0.0167	0.0112 ± 0.0054	0.0288 ± 0.0206	0.0858 ± 0.0208	0.1253 ± 0.0226
1.2390	0.0265	0.0600 ± 0.0158	0.0023 ± 0.0036	0.0210 ± 0.0185	0.0491 ± 0.0171	0.1781 ± 0.0224
1.2657	0.0269	0.0578 ± 0.0164	0.0153 ± 0.0049	0.0169 ± 0.0157	0.0808 ± 0.0174	0.1632 ± 0.0232
1.2925	0.0267	0.0477 ± 0.0158	0.0141 ± 0.0051	0.0174 ± 0.0162	0.0394 ± 0.0169	0.1762 ± 0.0274
1.3190	0.0263	0.0740 ± 0.0141	0.0198 ± 0.0049	0.0351 ± 0.0182	0.0249 ± 0.0178	0.1739 ± 0.0216
1.3454	0.0265	0.0840 ± 0.0172	0.0122 ± 0.0052	0.1050 ± 0.0267	0.0318 ± 0.0165	0.1769 ± 0.0226
1.3723	0.0274	0.0943 ± 0.0155	0.0150 ± 0.0046	0.0863 ± 0.0205	0.0264 ± 0.0147	0.1447 ± 0.0256
1.4000	0.0280	0.0772 ± 0.0161	0.0060 ± 0.0044	0.1188 ± 0.0227	0.0496 ± 0.0173	0.1937 ± 0.0234
1.4283	0.0285	0.1016 ± 0.0157	0.0188 ± 0.0048	0.1343 ± 0.0276	0.0969 ± 0.0185	0.1958 ± 0.0232
1.4572	0.0294	0.0845 ± 0.0182	0.0157 ± 0.0052	0.1228 ± 0.0217	0.0848 ± 0.0210	0.2375 ± 0.0254
1.4873	0.0308	0.1243 ± 0.0186	0.0227 ± 0.0053	0.0498 ± 0.0185	0.0723 ± 0.0165	0.2661 ± 0.0237
1.5186	0.0318	0.0787 ± 0.0185	0.0277 ± 0.0054	0.0510 ± 0.0232	0.0642 ± 0.0196	0.2197 ± 0.0243
1.5514	0.0337	0.1265 ± 0.0168	0.0228 ± 0.0043	0.0511 ± 0.0187	0.0307 ± 0.0171	0.2019 ± 0.0264
1.5862	0.0360	0.0993 ± 0.0188	0.0184 ± 0.0056	0.0276 ± 0.0204	0.0511 ± 0.0178	0.1687 ± 0.0247
1.6237	0.0390	0.0286 ± 0.0162	0.0150 ± 0.0055	0.0502 ± 0.0215	0.0812 ± 0.0176	0.2099 ± 0.0260
3.6000	Spz3	0.4150 ± 0.0420	0.2560 ± 0.0140	0.3560 ± 0.0350	0.3190 ± 0.0310	0.4210 ± 0.0110
4.5000	Spz8	0.4820 ± 0.0420	0.2140 ± 0.0200	0.3720 ± 0.0540	0.3430 ± 0.0270	0.4280 ± 0.0120
5.8000	Spz5	...	0.3100 ± 0.0340	0.4490 ± 0.0970	...	0.6960 ± 0.0600
8.0000	Spz8	...	0.3910 ± 0.0220	0.4750 ± 0.0460	...	0.6960 ± 0.0960
16.0000	Spz16	...	0.5190 ± 0.0200
24.0000	Spz24	...	0.5980 ± 0.0380

Note. λ refers to the central wavelength of the bin and $\Delta\lambda$ is the bin width. For Spitzer, the bin widths are irrelevant because we consider the spectral response of the channel.

(This table is available in its entirety in machine-readable form.)

population by atmospheric retrievals with a nested sampling optimizer and by testing a variety of atmospheric scenarios.

B.2.1. Emission and Transmission Forward Models from TauREx3

For both transit and eclipse scenarios, the atmosphere is modeled assuming 1D layers (default 100 layers). In the transit case (Waldmann et al. 2015b), the total transit depth at wavelength λ is given by

$$\Delta_\lambda = \frac{R_p^2 + a_\lambda}{R_s^2}, \quad (3)$$

where R_p is the planet radius and R_s is the parent star radius. a_λ is the wavelength contribution from the atmosphere (transit

depth), which takes the form

$$a_\lambda = 2 \int_0^{z_{\max}} (R_p + z)(1 - e^{-\tau_\lambda(z)}) dz. \quad (4)$$

where z_{\max} is the altitude at the top of the atmosphere and $\tau_\lambda(z)$ is the wavelength-dependent optical depth. It is evaluated by

$$\tau_\lambda(z) = \sum_i \tau_{\lambda,i}(z), \quad (5)$$

with $\tau_{\lambda,i}$ is the optical depth of each absorber i .

In eclipse (Waldmann et al. 2015a), the emission from each layer is integrated to produce the final spectrum. The wavelength-dependent intensity at the top of the atmosphere

Table B4
List of Transit Spectra Used in This Population Study

λ (μm)	$\Delta\lambda$	HAT-P-7 b	HAT-P-32 b	HAT-P-41 b	HD 189733b	HD 209458b	KELT-1 b
1.1262	0.0219	0.5210 \pm 0.0353	2.3076 \pm 0.0115	1.0104 \pm 0.0097	2.4271 \pm 0.0066	1.4591 \pm 0.0029	0.5613 \pm 0.0092
1.1478	0.0211	0.5171 \pm 0.0323	2.2925 \pm 0.0113	1.0328 \pm 0.0090	2.4319 \pm 0.0076	1.4565 \pm 0.0041	0.5553 \pm 0.0076
1.1686	0.0206	0.6135 \pm 0.0311	2.2939 \pm 0.0092	1.0222 \pm 0.0099	2.4430 \pm 0.0074	1.4581 \pm 0.0037	0.5680 \pm 0.0085
1.1888	0.0198	0.4841 \pm 0.0297	2.3032 \pm 0.0102	1.0268 \pm 0.0088	2.4304 \pm 0.0082	1.4542 \pm 0.0040	0.5872 \pm 0.0076
1.2084	0.0193	0.5820 \pm 0.0342	2.3107 \pm 0.0106	1.0194 \pm 0.0103	2.4300 \pm 0.0082	1.4551 \pm 0.0033	0.5785 \pm 0.0069
1.2275	0.0190	0.5471 \pm 0.0310	2.3040 \pm 0.0104	1.0285 \pm 0.0087	2.4219 \pm 0.0092	1.4605 \pm 0.0039	0.5717 \pm 0.0075
1.2465	0.0189	0.5870 \pm 0.0341	2.2861 \pm 0.0098	1.0202 \pm 0.0086	2.4115 \pm 0.0072	1.4518 \pm 0.0031	0.5834 \pm 0.0088
1.2655	0.0192	0.5291 \pm 0.0381	2.2834 \pm 0.0098	1.0187 \pm 0.0098	2.4198 \pm 0.0065	1.4512 \pm 0.0034	0.5764 \pm 0.0074
1.2847	0.0193	0.5533 \pm 0.0377	2.3034 \pm 0.0140	1.0372 \pm 0.0107	2.4168 \pm 0.0072	1.4587 \pm 0.0039	0.5881 \pm 0.0102
1.3038	0.0188	0.5214 \pm 0.0337	2.2908 \pm 0.0117	1.0174 \pm 0.0080	2.4325 \pm 0.0072	1.4552 \pm 0.0035	0.5812 \pm 0.0090
1.3226	0.0188	0.5341 \pm 0.0318	2.3030 \pm 0.0108	1.0164 \pm 0.0090	2.4283 \pm 0.0068	1.4528 \pm 0.0041	0.5809 \pm 0.0086
1.3415	0.0189	0.5084 \pm 0.0358	2.3352 \pm 0.0125	1.0394 \pm 0.0082	2.4318 \pm 0.0068	1.4639 \pm 0.0037	0.5822 \pm 0.0077
1.3605	0.0192	0.6058 \pm 0.0330	2.3386 \pm 0.0103	1.0503 \pm 0.0096	2.4446 \pm 0.0065	1.4708 \pm 0.0033	0.5781 \pm 0.0088
1.3800	0.0199	0.6097 \pm 0.0345	2.3320 \pm 0.0093	1.0271 \pm 0.0102	2.4388 \pm 0.0066	1.4683 \pm 0.0039	0.5672 \pm 0.0095
1.4000	0.0200	0.5537 \pm 0.0345	2.3139 \pm 0.0131	1.0412 \pm 0.0083	2.4367 \pm 0.0077	1.4752 \pm 0.0033	0.5731 \pm 0.0085
1.4202	0.0203	0.5620 \pm 0.0340	2.3399 \pm 0.0094	1.0463 \pm 0.0081	2.4458 \pm 0.0079	1.4631 \pm 0.0038	0.5700 \pm 0.0083
1.4406	0.0206	0.5891 \pm 0.0324	2.3443 \pm 0.0105	1.0451 \pm 0.0091	2.4385 \pm 0.0066	1.4638 \pm 0.0048	0.5806 \pm 0.0077
1.4615	0.0212	0.5259 \pm 0.0340	2.3096 \pm 0.0120	1.0457 \pm 0.0099	2.4315 \pm 0.0067	1.4584 \pm 0.0040	0.5747 \pm 0.0085
1.4831	0.0220	0.5254 \pm 0.0343	2.3156 \pm 0.0129	1.0457 \pm 0.0093	2.4341 \pm 0.0076	1.4629 \pm 0.0036	0.5890 \pm 0.0080
1.5053	0.0224	0.6097 \pm 0.0345	2.3149 \pm 0.0180	1.0481 \pm 0.0113	2.4271 \pm 0.0075	1.4614 \pm 0.0032	0.5701 \pm 0.0082
1.5280	0.0230	0.5915 \pm 0.0418	2.3031 \pm 0.0129	1.0421 \pm 0.0104	2.4338 \pm 0.0071	1.4606 \pm 0.0038	0.5628 \pm 0.0084
1.5516	0.0241	0.5425 \pm 0.0361	2.3110 \pm 0.0113	1.0345 \pm 0.0090	2.4123 \pm 0.0061	1.4565 \pm 0.0031	0.5545 \pm 0.0094
1.5762	0.0253	0.5407 \pm 0.0380	2.3116 \pm 0.0122	1.0282 \pm 0.0099	2.4209 \pm 0.0069	1.4584 \pm 0.0035	0.5726 \pm 0.0093
1.6021	0.0264	0.6047 \pm 0.0384	2.2796 \pm 0.0100	1.0172 \pm 0.0105	2.4223 \pm 0.0075	1.4504 \pm 0.0044	0.5686 \pm 0.0094
1.6294	0.0283	0.5383 \pm 0.0397	2.2666 \pm 0.0141	1.0189 \pm 0.0112	2.4141 \pm 0.0074	1.4577 \pm 0.0037	0.5676 \pm 0.0078

Note. λ refers to the central wavelength of the bin and $\Delta\lambda$ is the bin width.

(This table is available in its entirety in machine-readable form.)

Table B5
Table of Interpretation for the Bayes Factor Adapted from Kass & Raftery (1995)

Grade	B	$\Delta\ln(E)$	Interpretation
Grade 0	$B < 1$	$\Delta\ln(E) < 0$	Evidence against M1
Grade 1	$1 < B < 3$	$0 < \Delta\ln(E) < 1$	Evidence for M1 not worth mentioning
Grade 2	$3 < B < 20$	$1 < \Delta\ln(E) < 3$	Positive Evidence for M1
Grade 3	$20 < B < 150$	$3 < \Delta\ln(E) < 5$	Strong Evidence for M1
Grade 4	$B > 150$	$\Delta\ln(E) > 5$	Decisive Evidence for M1

Note. The Bayes factor B is defined as the evidence ratios of the models M1 and M2. In particular $\ln(B) = \Delta\ln(E)$. Note that we use $\ln(E)$, the natural logarithm of the evidence, which is the standard MultiNest outcome and is often denoted $\log(E)$ in the literature.

from a viewing angle θ is

$$I(\tau = 0, \mu) = B_\lambda(T_s) e^{-\frac{\tau_s}{\mu}} + \int_0^1 \int_0^{\tau_s} B_\lambda(T_\tau) e^{-\frac{\tau}{\mu}} d\tau d\mu, \quad (6)$$

where $\mu = \cos(\theta)$, $B_\lambda(T)$ is the plank function at a given temperature T , T_s denotes the temperature at maximum atmospheric pressure, and τ_s is the total optical depth from the planetary surface to the top of the atmosphere. Then, the flux is integrated for the cosine viewing angle μ using an N -point Gauss–Legendre quadrature scheme:

$$I(\tau = 0) = \sum_i^N I(\tau = 0, x_i) x_i w_i, \quad (7)$$

where w_i and x_i are our weights and abscissas, respectively.

The final emission spectrum is expressed as

$$\frac{F_p}{F_s} = \frac{I(\tau = 0)}{I_s} \times \left(\frac{R_p}{R_s} \right)^2, \quad (8)$$

where I_s is the specific intensity from the star in this work modeled using PHOENIX spectra (Allard et al. 2012).

B.2.2. Opacity Sources

Molecular opacity sources are included in both transmission and emission using their cross sections $\zeta_{i,\lambda}$. Their contribution to the optical depth is then given by

$$\tau_{\lambda,i}(z) = \int_z^{z_{\max}} \zeta_{i,\lambda}(z') \chi_i(z') \rho(z') dz', \quad (9)$$

where χ_i is the column density of the species i and ρ is the number density of the atmosphere. The contributions are integrated along the line of sight parameterized by dz' .

For the chemistry, we use the molecular line lists from the Exomol project (Tennyson et al. 2016; Chubb et al. 2021), HITEMP (Rothman & Gordon 2014), and HITRAN (Gordon et al. 2016). In the free retrievals, we consider molecular cross sections at resolution $R = 15,000$ for H₂O (Barton et al. 2017; Polyansky et al. 2018), CH₄ (Hill et al. 2013; Yurchenko & Tennyson 2014), CO (Li et al. 2015), CO₂ (Yurchenko et al. 2020), TiO (McKemmish et al. 2019), VO (McKemmish et al. 2016), FeH (Bernath 2020), and H⁻ (John 1988; Edwards et al. 2020) depending on the model considered. In the chemical equilibrium runs, additional molecules are considered: HCN (Barber et al. 2013), H₂CO (Al-Refaie et al. 2015), H₂S (Azzam et al. 2016), CN (Syme & McKemmish 2021), CP (Ram et al. 2014; Bernath 2020; Qin et al. 2021), C₂H₂ (Chubb et al. 2020b), C₂H₄ (Mant et al. 2018), NH₃ (Al Derzi et al. 2015; Coles et al. 2019), MgO (Li et al. 2019), AlO (Patrascu et al. 2015; Bowsman et al. 2021), SiO (Barton et al. 2013; Yurchenko et al. 2022), PH₃ (Sousa-Silva et al. 2015), ScH (Lodi et al. 2015), and CrH (Bernath 2020). Atomic and ionic species were not included as they do not absorb in the wavelength range considered here.

In this work, we assumed that the planets are mainly composed of hydrogen and helium with He/H₂ = 0.17. In addition to molecular opacities, we included collision-induced absorption (CIA) of the H₂–H₂ (Abel et al. 2011; Fletcher et al. 2018) and H₂–He (Abel et al. 2012) pairs as well as opacities induced by Rayleigh scattering (Cox 2015).

For planets with temperatures higher than 2000 K, the dayside is expected to be cloud free. For planets in lower-temperature regimes, we tested the presence of clouds on the dayside using two parametric models. We first tested a fully opaque gray cloud layer with a single free parameter, the cloud deck top pressure. Such a model is often used when analyzing HST data due to the small wavelength coverage in near-infrared. Because we also include the infrared bands from Spitzer in the eclipse analyses, we also tested a more realistic Mie model from Lee et al. (2013). The retrieved parameters for this model are cloud top pressure, cloud particle radius, and cloud mixing ratio. Comparing the Bayesian evidence of both of the cloudy retrievals with the cloud-free case, we did not find evidence in favor of clouds in any of the eclipse spectra. Therefore, for the rest of the paper, we did not include clouds for eclipse retrievals. We note, however, that tested cloud models only simulate extinction processes and do not account for complex scattering. In transit, because the observations are more sensitive to clouds, we included the fully opaque gray cloud model in all retrievals.

B.2.3. Retrieval Model Setups

In order to build our comparative study, we perform the same standardized retrievals for all the planets using Alfnor. All the planets in our study possess eclipse observations. The planet atmospheres are modeled using a plane-parallel assumption and composed of 100 layers spaced in log pressures from 10⁶ to 10⁻⁵ Pa. The stellar parameters and planetary mass are always fixed to literature values as dedicated studies provide better constraints than what can be recovered from our data (Changeat et al. 2020c).

In eclipse, due to the stronger degeneracies with the thermal profile, we fix the planetary radius to the literature values. We parameterize the temperature profile using an N -point point-free profile containing three nodes. This is a heuristic profile that linearly interpolates between N freely moving points. We perform a total of eight retrievals using four different models:

1. *Reduced*: This conservative model uses free chemistry with constant altitude mixing ratios. It includes the molecular opacities from H₂O, CH₄, CO, and CO₂ for a total of nine free parameters.
2. *Full*: This model uses free chemistry with constant altitude mixing ratios. In addition to the molecules of the reduced run, it includes the optical absorbers TiO, VO, FeH, and H⁻ for a total of 13 free parameters.
3. *Equilibrium (Eq)*: This model uses equilibrium chemistry from the GGChem model (Woitke et al. 2018). All the species available in GGChem were used to compute the chemistry and all the available opacity sources (see Appendix B.2.2) were included. To explore the thermal profile, we use the same N -point parameterization as for the free cases, so the total number of free parameters is 7.
4. *Blackbody*: For reference we perform a retrieval with no molecules and a simple isothermal profile (one free parameter). This is used as a reference to compare the Bayesian evidence of the other models.

For each of those different models, we run an HST-only case and an HST+Spitzer scenario. When Spitzer is included, we use the calibrated Spitzer instrument responses (Reach et al. 2005) to account for the wavelength-dependent behavior of the detector.

When available, we complement our eclipse retrievals with an analysis of the HST transit spectrum. In this case, we also retrieve the planet radius R_p and a gray opaque cloud deck as these observations are more sensitive to those properties. Because in transmission the impact of the temperature is mostly on the scale height, we restrain our model to an isothermal temperature structure (Rocchetto et al. 2016; Changeat et al. 2019). Here we only analyze the HST-WFC3 spectra and do not consider the additional Spitzer data. We run two separate retrievals:

1. *Full*: This model uses free chemistry with constant with altitude mixing ratios. We include all the absorbers: H_2O , CH_4 , CO , CO_2 , TiO , VO , FeH , and H^- , for a total of 11 free parameters.
2. *Equilibrium (Eq)*: This model uses equilibrium chemistry from the GGChem model (Woitke et al. 2018) and the same isothermal temperature profile. The number of free parameters is five.
3. *Featureless fit*: For reference, we performed a transit fit with no molecule, fitting only for a flat line. The number of free parameters is one.

B.2.4. Exploration of the Parameter Space

All the free parameters considered in this study are explored using uniform, noninformative priors. These are listed in more detail in Table B5. For the chemistry, because all the planets considered are large hot Jupiters, we assume a primary envelope and therefore limit the retrieved maximum bound of the considered active molecules to 0.01. We imposed stricter priors on the optical absorbers, limiting their abundance to a maximum of 10^{-4} as their abundance is expected to be much less (Woitke et al. 2018). For the lower bounds, we select 10^{-12} as such abundance is low enough to not leave any spectral features at the resolution and S/N considered. The sampling is done using the nested sampling algorithm *MultiNest* (Feroz et al. 2009) with 750 live points and a log-likelihood tolerance of 0.5. This ensures an optimal free exploration of the parameter space.

Because we use the nested sampling algorithm *MultiNest*, the computation of the Bayesian evidence for each model, here denoted E , is automatic. Then, the difference in $\ln(E)$ between two models M1 and M2 can be used for model selection and to compare the ability of the two models to explain the observed spectra (Jeffreys 1961; Kass & Raftery 1995; Feroz et al. 2009). The original Jeffreys' scale that we employ in this study is summarized in Table B5.

Appendix C Supplementary Text

C.1. Model Choices and Degeneracies

Atmospheric retrieval techniques were historically developed for Earth and solar system applications, where in situ and high-quality measurements provide a wealth of information. In this context, retrievals are used to infer probability distributions on a set of parameters for which prior knowledge is already available and tightly constraining. On the opposite, exoplanet retrievals must deal with low information content data sets and physical systems that are poorly understood. In this context, model assumptions are crucial (Min et al. 2020). These assumptions are user defined and should be selected carefully,

as a retrieval will always provide a model-dependent solution (Rocchetto et al. 2016; Changeat et al. 2019, 2020a). In general, free assumptions attempt to heuristically describe properties of exoplanets, such as thermal or chemical profiles, using as few assumptions as possible. Conversely, self-consistent models describe the given property using physically driven assumptions, for example, chemical equilibrium or radiative equilibrium. In a low prior knowledge case, free retrievals should be favored until the understanding of the system is high enough to justify the assumptions of self-consistent models. Another issue of self-consistent modeling in retrievals is that the addition of more physical descriptions comes at the cost of computational resources, which often limits the level of details that can be included. In this work, we chose to explore both options, using free and equilibrium chemistry retrievals. Often, we find that the free approach leads to a better Bayesian evidence, thus demonstrating that the added flexibility in the free models provides a better explanation of the data sets considered here.

In this work, we focus on eclipse spectra, which, as compared to transit observations, provide more constraints on the thermal profile (Burrows 2014; Rocchetto et al. 2016). Due to the narrow wavelength range of HST, only one broadband spectral feature is usually observed, which can be difficult to interpret without further constraints. In the HST-only case, the retrievals can easily be misguided, confusing for instance whether a single feature should be seen in emission or absorption. This is the case for HD 209458b (see corresponding section), where the HST-only retrievals converge to two different solutions depending on the opacities that are considered. When optical absorbers are included, the retrieval interprets the spectrum with an emission feature, while it is simply fit with the absorption of H_2O in the reduced run. Adding the Spitzer data, here, provides confidence that the second scenario is more likely, but such degeneracies are often difficult to disentangle. In this work, we performed retrievals using a reduced list of opacities and a full list, as well as HST-only and HST+Spitzer scenarios. In general, we find that a larger wavelength coverage is often required to extract information regarding the chemistry and thermal profile of the observed atmospheres in eclipse, and we therefore focus on the HST+Spitzer runs for the main part of this study.

C.2. Biases Arising from the Data Reduction

In previous works, data-reduction pipelines have led to different answers when used on the same raw data. When considering HST, different pipelines usually recover the same spectral shape, but differences can appear as flat offsets (Changeat et al. 2020b, e.g.). See also Figure Set B5, which compares our spectra with the ones obtained in the literature.

The observed flat offsets are usually attributed to differences in the background subtraction steps or different choices to model the HST ramps. A particularly striking example of such an offset can be seen in our reduction of the HD 209458b spectrum, which differs by about 160 ppm from the one obtained by Line et al. (2016). Such large offsets are difficult to explain by differences in the background subtraction alone. However, performing the reduction of the spectra using a quadratic trend for the long-term ramp, we obtained a similar flux level to Line et al. (2016). We also note that Line et al. (2016) fitted all the visits with a single transit model, which could have led to different results as their reduction did not rely

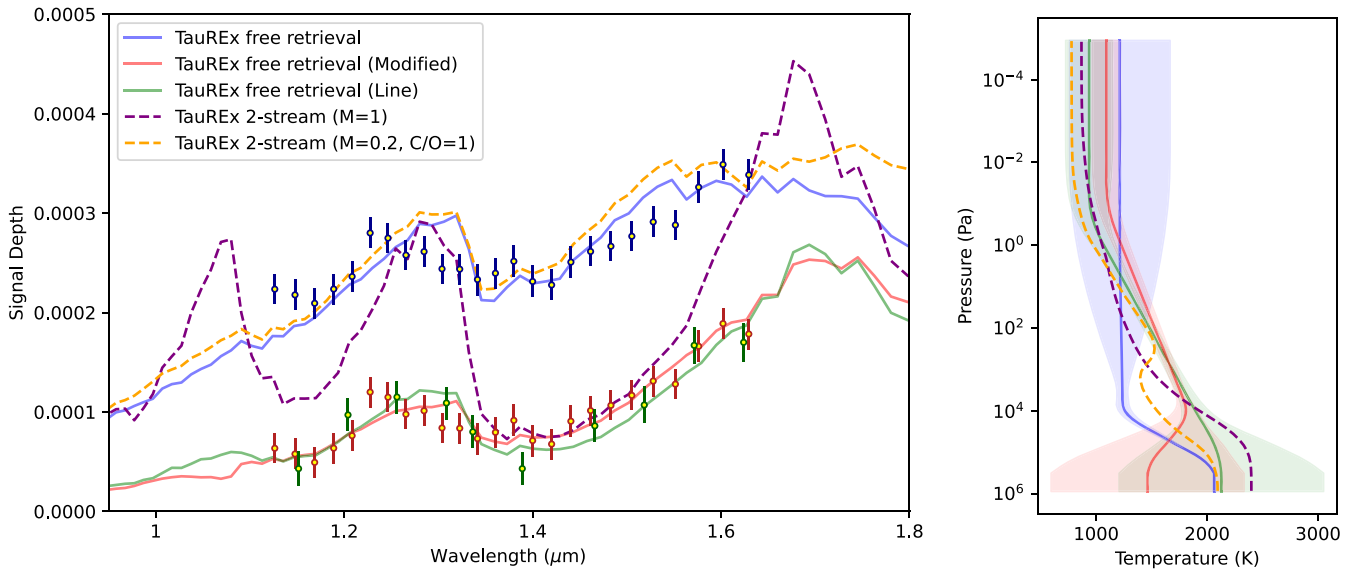


Figure C1. Simulated spectra (left) and thermal structure (right) for HD 209458b. The blue data points are our original Iraclis reduced spectrum. The green points are the Line et al. (2016) data. The red points are the Iraclis observations offset by 160 ppm to match the Line et al. (2016) absolute depth. The same color scheme is applied for our retrievals on those different data sets. We also added forward-model spectra computed from two-stream self-consistent approximations in dashed lines: solar in purple, and metallicity 0.2 and C/O = 1 in orange.

on a normalization of the white light-curve depths. While our pipeline does not offer this option at the moment, future investigations could assess the impact of performing joint or separate fits. In order to investigate further this particular case, we performed comparative retrievals on the Line et al. (2016) spectrum as well as our own spectrum offset by -160 ppm. In Figure C1 we show the results of this exercise.

In the same figure, we also show self-consistent estimates of the HD 209458b emission using a two-stream model available in TauREx. While not suitable for direct data analysis studies, self-consistent forward models provide important benchmark to compare retrieval outcomes. This forward model computes the thermal profile and chemistry in radiative and chemical equilibrium from the bulk and orbital parameters of the system, which are here taken from the literature. We show two models, one with solar metallicity and C/O and one with a metallicity 0.2 and a C/O of 1.0, which roughly matches the derived values of our full HST+Spitzer run. Those forward models predict a surface emission that might be compatible with the reduced observation we obtained from Iraclis. This exercise is by no means proving that our recovered spectrum is correct, but this highlights systematic biases that can arise from different assumptions in HST reduction pipeline.

These offsets can even be more difficult to handle when combining observations from different instruments in transit (Changeat et al. 2020b; Yip et al. 2020; Saba et al. 2021; Yip et al. 2021). In eclipse or the phase curve (Changeat et al. 2021), similar incompatibilities can occur depending on the different reduction techniques or input parameters. Similarly, if the observations are not carried out simultaneously, one encounters the risk of contamination from stellar or even planetary variabilities. Indeed, dynamic simulations predict that exoplanet atmospheres are subject to large variabilities, with time-dependent storms and modons (Cho et al. 2003, 2021). In this work, we do not investigate those phenomena further, and for simplicity, we assume that the obtained HST and Spitzer

observations are compatible. We, however, performed a few sensitivity tests.

In order to verify the stability of our results to potential offset biases in the Spitzer data, we performed complementary retrievals on the whole population. We applied the full scenario on the HST+Spitzer data, modifying the observed Spitzer data. In our first test, we doubled the error of the Spitzer data for all planets, which is equivalent to adding another source of unknown Gaussian noise. In the two supplementary tests, we tested potential biases in the Spitzer data by offsetting the eclipse depths of the Spitzer data by ± 100 ppm. In those three tests, we occasionally found different solutions for individual planets, but overall the trends reported using the unmodified Spitzer sets remained unchanged. This is shown in Figure C2, which displays the water-temperature map for our population in the case where the Spitzer noise has been doubled, and the case where Spitzer has been offset by $+100$ ppm.

C.3. On Constraining Metallicity and C/O from Free Retrievals

In our free runs, we also compute the metallicity as O/H and C/O following the standard practice in the field (Lee et al. 2013; MacDonald & Madhusudhan 2019). For each sample obtained during our retrieval exploration, we compute the metallicity, defined as the O/H normalized to the solar value of 4.9×10^{-4} (Asplund et al. 2009), and the C/O. Constraints on those parameters are important for planetary formation and evolution models.

The results of these calculations on our population are shown in Figure A8. We find that the estimates of metallicity and C/O from free retrievals heavily rely on the detected molecules (see the behavior of the C/O in individual planet analyses) and come with many simplifying assumptions. Often, when a single molecule is detected in the retrieval, the derived parameter will be heavily biased toward the elemental ratio of the detected molecule. For example, detecting only CO_2 will lead to a derived C/O of 0.5, which is spurious.

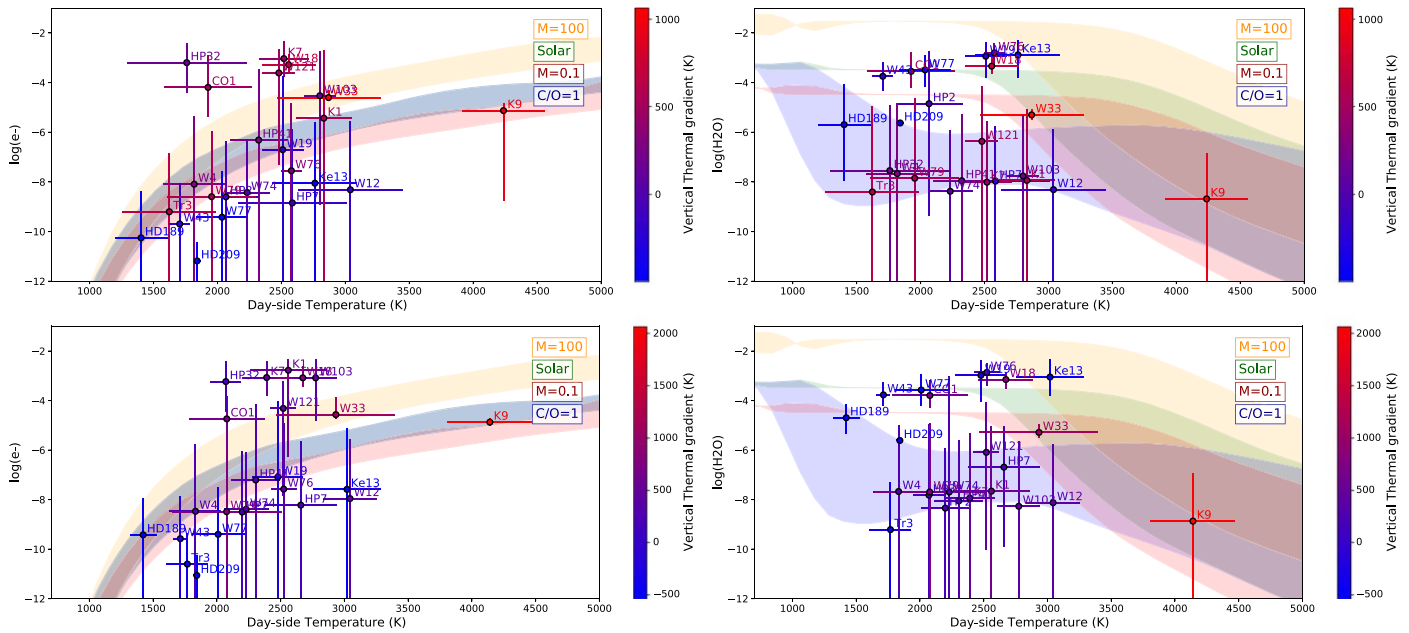


Figure C2. Recovered e^- (left) and H_2O (right) maps of our full retrieval performed on intentionally biased Spitzer data. Top: The noise of the Spitzer points has been doubled. Bottom: The eclipsed depth of the Spitzer points is offset by +100 ppm. While individual planet results can vary, the overall trends obtained from the unbiased Spitzer retrievals are conserved.

By comparing the derived metallicity to the one obtained by the equilibrium runs, we however believe this parameter is stable in the case where H_2O is clearly detected. This is shown in the top-left panel of Figure A8, where we show that the retrievals detecting H_2O to high accuracies lead to similar estimates of the metallicity in free and equilibrium runs. We attribute this to the good capabilities of HST to detect this particular molecule, and our better understanding of the class of planets between 1000 and 2000 K, which are believed to more closely following equilibrium chemistry.

Appendix D Individual Planet Analyses

Individual exoplanet retrieval results are described in these sections. Figure D1 shows the eclipse results and Figure D2 shows the transit results. Table D1 summarizes the recovered parameters and provides the Bayesian evidence of each model. For molecules, nondetections are characterized by a retrieved $\log(\text{VMR})$ below -8 for the mean and if the mean minus the sum of the 1σ uncertainties (on both sides) is lower than -12 . In this case, only the upper limit is provided.

D.1. Individual Analysis of CoRoT-1 b

The first transit of CoRoT-1 b was observed in 2008 (Barge et al. 2008), unveiling a $1.5 R_J$ inflated planet. Later observations from the ground indicated a significant emission signal, corresponding to a temperature of approximately 2300 K and potentially poor heat redistribution between the day- and nightsides (Alonso et al. 2009; Gillon et al. 2009). The planet transit from HST-WFC3 (PN: 12181, PI: Deming 2010) was previously studied but no evidence for molecular absorption was found due to the high uncertainties on the data (Ranjan et al. 2014). The same proposal included eclipse observations, but no analysis of these has since been published. However, a follow-up study in 2010 analyzed Spitzer eclipse observations

(Deming et al. 2010) and found potential evidence for high-altitude absorbers or an isothermal region in the atmosphere. We analyze the transmission and emission HST visits using our standardized pipeline and performed retrieval analyses (see Materials and Methods section). For the eclipse, we considered the Spitzer observations reduced in Deming et al. (2010), which are taken without modifications.

On the dayside, the HST and HST+Spitzer are consistent with a thermal inversion. The posterior distributions indicate spectral signatures for H_2O , VO, and H^- opacities, which is consistent with the findings in Deming et al. (2010). The retrieved temperatures of about 2000 K could explain the presence of the detected absorbers. For the free runs including the full list of opacities, the chemistry is consistent with a solar metallicity and a subsolar C/O. We note that, because no C-bearing species are detected, the C/O from the free runs is likely biased. When equilibrium chemistry is used, a thermal inversion is also recovered, with different thermal profiles depending on whether Spitzer is included or not. The equilibrium retrievals tend to converge toward an atmosphere with solar or enriched metallicity and a C/O of about 1. Our analysis provides decisive evidence in favor of the free model that includes H_2O and the optical absorbers VO and H^- .

For the transit observation, the spectrum shows a downward slope toward the red end of the spectrum. In the free run, it is best fit with a cloudy atmosphere and a potential contribution from VO. This result is consistent with the detected absorption of VO on the dayside and the recovered temperature of around 1800 K. In this free scenario, the atmosphere might be consistent with a solar metallicity and C/O, but we note that the uncertainties on those derived parameters are large, also allowing for subsolar to supersolar C/O. The equilibrium run leads to similar estimates of the metallicity and the C/O, with better constraints, but the recovered temperature is unphysical, with a mean higher than that at the dayside.

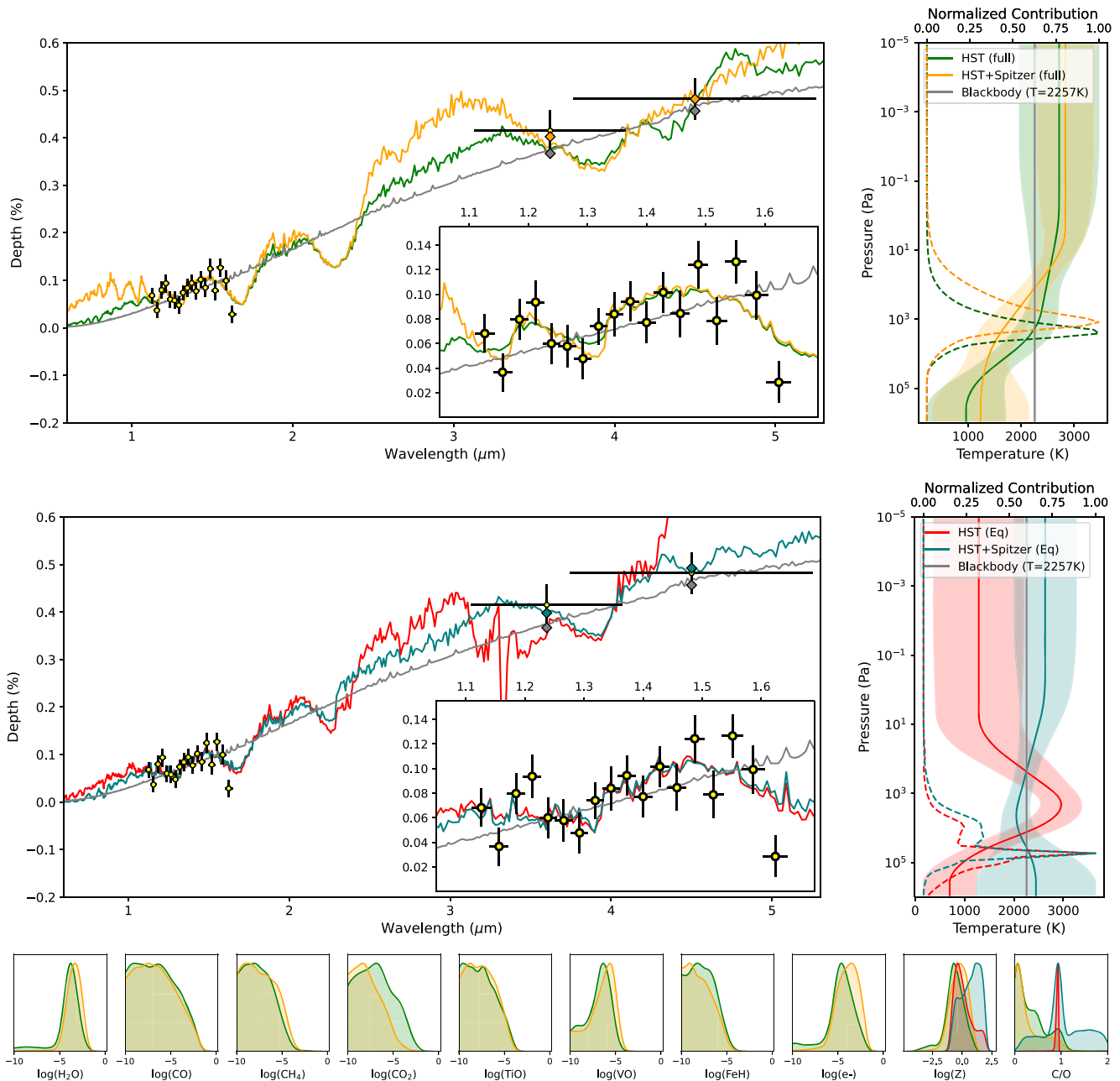


Figure D1. Retrieval results for CoRoT-1 b. Top: best-fit eclipse spectra (left) and thermal structure (right) for the free retrievals. Middle: best-fit eclipse spectra (left) and thermal structure (right) for the equilibrium retrievals. Bottom: posterior distributions of these runs. The complete figure set (25 images) is available. (The complete figure set (25 images) is available.)

D.2. Individual Analysis of HAT-P-2 b

HAT-P-2 b was discovered in 2007 by Bakos et al. (2007). It is a massive hot Jupiter ($9.1 M_J$) that orbits its host star in a highly eccentric orbit ($e = 0.52$) in about 5.6 days. Due to its large density, the planet is believed to require the presence of a large core. This large mass, combined with the highly eccentric orbit, raises many questions regarding the physics of this planet and its formation. For instance, along its entire orbit, the planet's equilibrium temperature varies from 1240 K to 2150 K Bakos et al. (2007). Studying the Rossiter–McLaughlin effect, Winn et al. (2007) and Loeillet et al. (2008) found that the stellar spin axis and orbital axis of the planet should be aligned,

thus implying that the planet did not evolve through scattering or Kozai migration.

While being a very interesting planet, the atmosphere of HAT-P-2 b was not studied with many instruments. A phase-curve observation with Spitzer at 3.6, 4.5, 5.6, and $8 \mu\text{m}$ was presented in Lewis et al. (2013), highlighting a very complex atmosphere due to the particular orbital configuration of this planet. The study also suggested the planet might experience a temporary dayside thermal inversion near periapease. In a follow-up work, Lewis et al. (2014) performed a complementary analysis with GCMs to evaluate the impact of the eccentricity on the chemistry and the thermal structure of this planet,

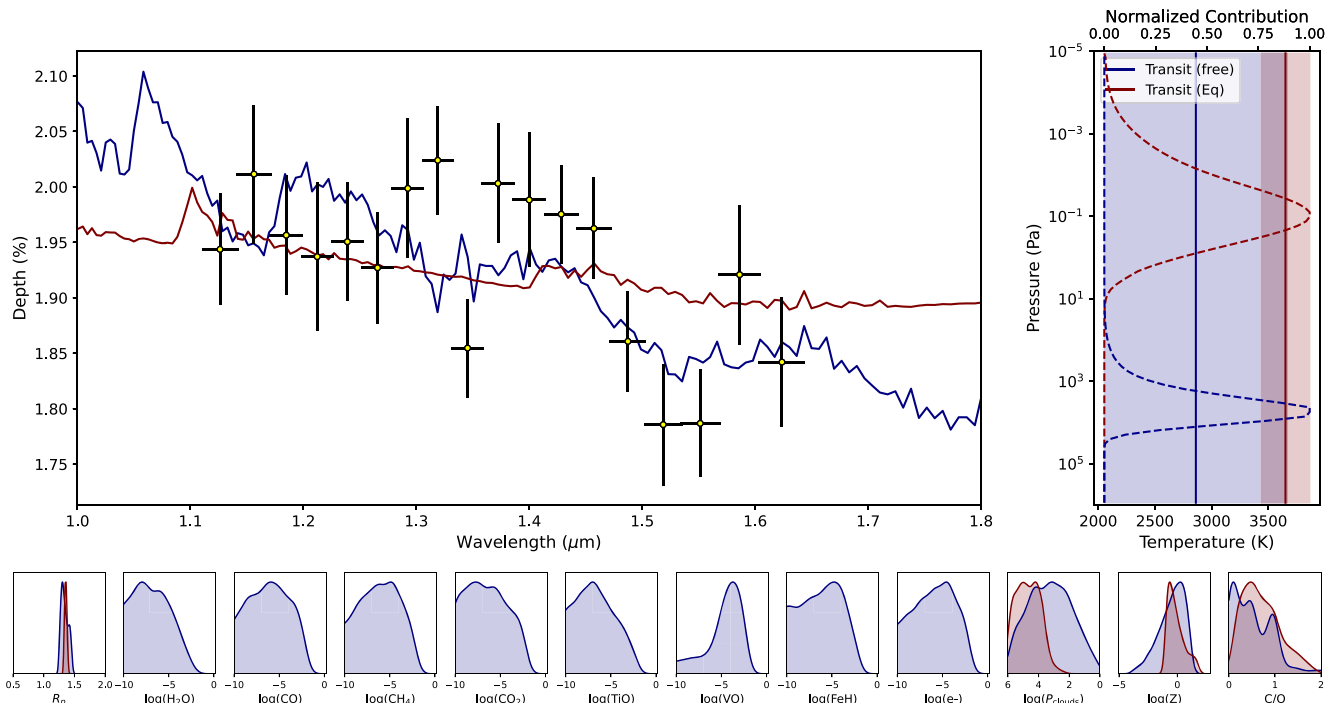


Figure D2. Top: best-fit spectra (left) and thermal structure (right) for the transit retrievals. Bottom: posterior distributions of these runs.

(The complete figure set (17 images) is available.)

highlighting that disequilibrium processes on this planet might be important.

Recently, a partial phase curve was acquired with HST using grism G141 (PN: 16194, PI: Desert et al. 2020). We fitted the publicly available data using our standardized Iraclis pipeline. These data were complemented with the Spitzer observations, taken as they are from Lewis et al. (2013).

We performed our retrieval of this planet with Alfnor. All our retrieval models provide the same interpretation of the data, and the HAT-P-2 b eclipse spectrum does not show clear signatures for any molecule. The atmosphere is best interpreted by an isothermal profile, with eventually some marginal water feature. However, comparisons of the Bayesian evidence indicate that the detection is tentative at best. The spectrum is well explained by a simple blackbody fit, and we are not able to confirm the thermally inverted profile predicted by Lewis et al. (2013). Due to the fact that the HST and Spitzer observations were not carried out simultaneously, we note that the atmospheric conditions might have changed between the different observations, in particular considering the additional variability introduced by the highly eccentric orbit.

D.3. Individual Analysis of HAT-P-7 b

HAT-P-7 b is an inflated hot Jupiter of $1.4 R_J$ (Pál et al. 2008), which was first studied in emission during the commissioning program of Kepler when the satellite detected the eclipse as part of an optical phase curve (Borucki et al. 2009). These measurements indicated that HAT-P-7 b could have a dayside temperature of around 2650 K, which confirmed predictions from (Fortney et al. 2008; Pál et al. 2008). This optical eclipse measurement was combined with Spitzer photometry over $3.5\text{--}8 \mu\text{m}$ to infer the presence of a thermal inversion (Christiansen et al. 2010), suggested by the high flux

ratio in the $4.5 \mu\text{m}$ channel of Spitzer compared to that in the $3.6 \mu\text{m}$ channel. In their paper, chemical equilibrium models associated these emission features with CO, H_2O , and CH_4 . A thermal inversion was also reported to provide the best fit to this data by the atmospheric models of Spiegel & Burrows (2010) and Madhusudhan & Seager (2010) but all three studies noted that models without a thermal inversion could also explain well the data though only with an extremely high abundance of CH_4 . Further Kepler phase curves identified an offset in the dayside hot spot (Esteves et al. 2013, 2015) as well as changes in its location (Armstrong et al. 2016), highlighting the complex dynamics of hot-Jupiter atmospheres. However, while Spitzer phase curves at 3.5 and $4.5 \mu\text{m}$ were also best fitted with a thermal inversion on the dayside and relatively inefficient day–night recirculation, Wong et al. (2016) did not find evidence of a hot-spot offset. Two eclipses were then obtained using HST-WFC3 G141 which, when combined with previous observations, were found to be best fit with a thermal inversion due to optical absorbers but at a low significance when compared to a baseline blackbody fit (Mansfield et al. 2018).

We fitted the two scanning mode eclipse observations of HAT-P-7 b (PN: 14792, PI: Bean et al. 2016). We note that three staring mode eclipse observations were also taken (PN: 12181, PI: Deming 2010), but we ignore these given the higher precision of the scanning mode observations. Additionally, a staring mode transmission spectrum had been taken (PN: 12181, PI: Deming 2010) but there was no postgress orbit and, due to significant systematics, our fit of the data presents large uncertainties. Models of HAT-P-7 b suggest the terminator region should have patchy clouds with water being well mixed throughout the atmosphere (Helling et al. 2019).

Table D1
Table of the Retrieval Results for the 24 Planets

Parameter	HST	HST+Spitzer (red)	HST	HST+Spitzer (full)	HST	HST+Spitzer (eq)	Transit (free)	Transit (eq)
CoRoT-1 b^a								
log(H ₂ O)	<-7.3	<-7.0	-3.9 ^{+0.7} _{-0.8}	-3.4 ^{+0.7} _{-0.7}	<-4.9	...
log(CH ₄)	-5.1 ^{+2.0} _{-4.1}	<-4.5	<-6.2	<-5.7	<-3.9	...
log(CO)	<-3.9	<-3.5	<-4.5	<-4.6	<-3.8	...
log(CO ₂)	<-5.1	<-3.6	<-5.1	<-6.5	<-4.0	...
log(TiO)	<-6.2	<-6.1	<-4.5	...
log(VO)	-6.8 ^{+1.0} _{-2.5}	-6.4 ^{+1.1} _{-2.7}	-4.3 ^{+1.3} _{-3.0}	...
log(FeH)	<-6.5	<-6.8	<-3.9	...
log(e ⁻)	-4.6 ^{+1.2} _{-1.5}	-3.9 ^{+1.1} _{-1.2}	-6.2 ^{+2.5} _{-3.5}	...
log(Z)	-1.7 ^{+1.4} _{-1.4}	-1.2 ^{+1.5} _{-1.5}	-0.6 ^{+0.8} _{-0.8}	-0.3 ^{+0.7} _{-0.7}	-0.1 ^{+1.0} _{-0.5}	0.8 ^{+0.8} _{-1.1}	-0.5 ^{+1.1} _{-1.1}	-0.3 ^{+0.9} _{-0.5}
C/O	1.0 ^{+0.5} _{-0.5}	0.9 ^{+0.5} _{-0.5}	0.3 ^{+0.3} _{-0.3}	0.3 ^{+0.3} _{-0.3}	0.9 ^{+0.0} _{-0.0}	0.9 ^{+0.7} _{-0.3}	0.5 ^{+0.5} _{-0.5}	0.6 ^{+0.5} _{-0.3}
ln(<i>E</i>)	118.1	125.6	119.1	132.4	116.8	127.7	100.0	96.9
HAT-P-2 b^b								
log(H ₂ O)	<-4.3	-5.8 ^{+1.9} _{-4.1}	-5.5 ^{+2.0} _{-4.1}	-3.7 ^{+1.1} _{-3.8}
log(CH ₄)	<-5.4	<-7.1	<-5.0	<-6.1
log(CO)	<-3.6	<-4.8	<-3.9	<-3.7
log(CO ₂)	<-3.2	<-6.6	<-3.1	<-5.5
log(TiO)	<-7.0	<-6.8
log(VO)	<-6.8	<-6.0
log(FeH)	<-6.8	<-7.1
log(e ⁻)	<-6.8	<-6.7
log(Z)	-0.8 ^{+1.3} _{-1.3}	-1.6 ^{+1.3} _{-1.3}	-0.8 ^{+1.4} _{-1.4}	-0.6 ^{+1.3} _{-1.3}	0.5 ^{+1.1} _{-1.2}	0.3 ^{+1.0} _{-0.9}
C/O	0.7 ^{+0.4} _{-0.4}	0.6 ^{+0.5} _{-0.5}	0.6 ^{+0.4} _{-0.4}	0.4 ^{+0.4} _{-0.4}	0.6 ^{+0.3} _{-0.3}	0.5 ^{+0.3} _{-0.2}
ln(<i>E</i>)	216.6	244.8	216.4	244.5	216.9	245.7
HAT-P-7 b^c								
log(H ₂ O)	<-6.1	<-6.9	<-3.3	-6.0 ^{+1.0} _{-3.4}	-5.3 ^{+2.3} _{-3.5}	...
log(CH ₄)	<-6.5	-5.9 ^{+0.7} _{-2.2}	<-4.9	<-6.9	<-3.6	...
log(CO)	<-3.9	<-4.8	<-4.1	<-3.8	<-4.6	...
log(CO ₂)	<-5.6	<-6.2	<-3.2	-2.5 ^{+0.3} _{-1.1}	<-3.6	...
log(TiO)	<-6.4	<-6.7	<-5.2	...
log(VO)	<-6.1	<-8.1	<-4.7	...
log(FeH)	<-5.1	-4.8 ^{+0.5} _{-0.6}	<-4.6	...
log(e ⁻)	<-4.2	<-5.9	<-3.9	...
log(Z)	-1.8 ^{+1.2} _{-1.2}	-2.4 ^{+1.1} _{-1.1}	-0.8 ^{+1.4} _{-1.4}	0.5 ^{+1.1} _{-1.1}	0.8 ^{+0.6} _{-0.9}	-0.4 ^{+1.1} _{-0.5}	-0.5 ^{+1.2} _{-1.2}	0.4 ^{+1.1} _{-0.9}
C/O	0.8 ^{+0.4} _{-0.4}	1.1 ^{+0.6} _{-0.6}	0.6 ^{+0.5} _{-0.5}	0.5 ^{+0.2} _{-0.2}	1.6 ^{+0.2} _{-0.3}	1.4 ^{+0.3} _{-0.3}	0.5 ^{+0.5} _{-0.5}	0.9 ^{+0.7} _{-0.5}
ln(<i>E</i>)	208.4	230.6	208.1	231.6	207.9	228.8	156.7	157.1
HAT-P-32 b^d								
log(H ₂ O)	<-7.4	<-6.8	<-5.7	<-4.9	-2.9 ^{+0.6} _{-0.7}	...
log(CH ₄)	<-6.8	<-7.8	<-5.4	-5.7 ^{+1.2} _{-3.7}	<-6.3	...
log(CO)	<-3.9	<-3.7	<-4.2	<-4.4	<-4.5	...
log(CO ₂)	-3.5 ^{+0.7} _{-0.8}	-2.8 ^{+0.5} _{-0.5}	<-4.5	<-7.0	<-4.9	...
log(TiO)	<-6.9	<-6.8	<-6.3	...
log(VO)	<-5.3	-6.6 ^{+1.5} _{-3.3}	<-7.1	...
log(FeH)	<-5.0	<-6.8	-7.9 ^{+1.4} _{-2.2}	...
log(e ⁻)	-3.8 ^{+1.2} _{-4.6}	-3.2 ^{+0.8} _{-1.0}	<-5.8	...
log(Z)	-0.1 ^{+0.9} _{-0.9}	0.6 ^{+0.6} _{-0.6}	-1.6 ^{+1.3} _{-1.3}	-1.8 ^{+1.1} _{-1.1}	1.0 ^{+0.6} _{-1.1}	0.4 ^{+1.0} _{-0.9}	0.1 ^{+0.6} _{-0.6}	-0.1 ^{+1.2} _{-0.7}
C/O	0.6 ^{+0.2} _{-0.2}	0.5 ^{+0.1} _{-0.1}	0.7 ^{+0.4} _{-0.4}	0.8 ^{+0.7} _{-0.7}	1.6 ^{+0.3} _{-0.3}	1.5 ^{+0.3} _{-0.3}	0.2 ^{+0.2} _{-0.2}	0.5 ^{+0.3} _{-0.3}
ln(<i>E</i>)	181.8	192.3	179.9	193.4	176.8	189.9	179.4	181.7
HAT-P-41 b^e								
log(H ₂ O)	<-6.9	<-6.9	<-4.8	<-5.6	-2.7 ^{+0.5} _{-0.6}	...
log(CH ₄)	<-6.9	<-6.7	<-4.1	<-6.1	<-5.2	...
log(CO)	<-4.7	<-5.5	<-4.1	<-4.8	<-4.3	...
log(CO ₂)	<-4.9	<-7.6	<-4.0	<-7.3	<-4.6	...
log(TiO)	<-7.1	<-6.0	<-6.8	...
log(VO)	-6.0 ^{+1.0} _{-2.8}	-6.0 ^{+1.5} _{-3.5}	<-7.2	...
log(FeH)	-5.7 ^{+1.2} _{-3.1}	-5.3 ^{+0.8} _{-2.6}	<-7.1	...
log(e ⁻)	-5.9 ^{+2.6} _{-3.3}	<-5.3	<-4.6	...
log(Z)	-1.9 ^{+1.2} _{-1.2}	-2.5 ^{+1.2} _{-1.2}	-1.2 ^{+1.2} _{-1.2}	-1.7 ^{+1.0} _{-1.0}	0.5 ^{+0.9} _{-0.9}	0.7 ^{+0.8} _{-0.9}	0.3 ^{+0.6} _{-0.6}	1.0 ^{+0.5} _{-1.1}

Table D1
(Continued)

Parameter	HST	HST+Spitzer (red)	HST	HST+Spitzer (full)	HST	HST+Spitzer (eq)	Transit (free)	Transit (eq)
C/O	$0.8^{+0.4}_{-0.4}$	$0.8^{+0.5}_{-0.5}$	$0.7^{+0.5}_{-0.5}$	$0.5^{+0.5}_{-0.5}$	$1.3^{+0.4}_{-0.8}$	$1.6^{+0.3}_{-0.3}$	$0.2^{+0.2}_{-0.2}$	$0.5^{+0.3}_{-0.2}$
$\ln(E)$	187.2	200.9	188.4	200.3	186.4	200.3	190.6	193.4
HAT-P-70 b^f								
$\log(\text{H}_2\text{O})$	<-5.8	...	<-5.0
$\log(\text{CH}_4)$	$-4.4^{+0.6}_{-3.1}$...	<-4.8
$\log(\text{CO})$	<-2.6	...	<-4.1
$\log(\text{CO}_2)$	<-3.6	...	<-3.3
$\log(\text{TiO})$	<-6.4
$\log(\text{VO})$	<-6.0
$\log(\text{FeH})$	<-7.5
$\log(e^-)$	$-3.1^{+0.7}_{-0.8}$
$\log(Z)$	$-0.8^{+1.4}_{-1.4}$...	$-1.2^{+1.4}_{-1.4}$...	$-0.5^{+0.6}_{-0.4}$
C/O	$1.0^{+0.5}_{-0.5}$...	$0.7^{+0.4}_{-0.4}$...	$1.0^{+0.05}_{-0.05}$
$\ln(E)$	198.3	...	201.5	...	200.0
HD 189733b^e								
$\log(\text{H}_2\text{O})$	<-6.3	$-5.4^{+0.5}_{-0.5}$	<-4.2	$-4.6^{+0.5}_{-0.6}$	$-2.6^{+0.4}_{-0.6}$...
$\log(\text{CH}_4)$	$-6.4^{+1.9}_{-3.6}$	<-8.3	<-4.0	<-8.0	<-5.3	...
$\log(\text{CO})$	<-3.6	<-3.7	<-4.3	<-3.1	<-4.3	...
$\log(\text{CO}_2)$	<-4.4	$-5.8^{+2.4}_{-0.6}$	<-4.0	$-2.5^{+0.3}_{-0.6}$	<-4.1	...
$\log(\text{TiO})$	<-5.5	<-6.4	<-5.2	...
$\log(\text{VO})$	<-5.8	<-7.2	$-7.4^{+1.4}_{-2.6}$...
$\log(\text{FeH})$	<-6.0	$-6.9^{+1.0}_{-2.3}$	<-7.2	...
$\log(e^-)$	$-3.5^{+1.0}_{-4.8}$	<-8.1	<-8.2	...
$\log(Z)$	$-1.5^{+1.4}_{-1.4}$	$-1.2^{+1.2}_{-1.2}$	$-1.2^{+1.3}_{-1.3}$	$0.8^{+0.7}_{-0.7}$	$-0.4^{+1.2}_{-0.4}$	$1.7^{+0.2}_{-0.3}$	$0.5^{+0.5}_{-0.5}$	$0.7^{+0.7}_{-1.0}$
C/O	$0.8^{+0.5}_{-0.5}$	$0.5^{+0.3}_{-0.3}$	$0.6^{+0.5}_{-0.5}$	$0.5^{+0.1}_{-0.1}$	$1.4^{+0.4}_{-0.3}$	$0.8^{+0.1}_{-0.2}$	$0.2^{+0.2}_{-0.2}$	$0.5^{+0.6}_{-0.3}$
$\ln(E)$	147.5	177.1	146.3	178.1	146.6	176.3	193.0	195.1
HD 209458b^h								
$\log(\text{H}_2\text{O})$	$-5.56^{+0.09}_{-0.08}$	$-5.6^{+0.06}_{-0.06}$	<-8.43	$-5.61^{+0.06}_{-0.06}$	$-2.69^{+0.41}_{-0.75}$...
$\log(\text{CH}_4)$	<-7.58	$-6.66^{+0.22}_{-0.25}$	<-7.78	$-6.68^{+0.22}_{-0.25}$	<-4.7	...
$\log(\text{CO})$	$-5.19^{+1.54}_{-4.42}$	$-3.77^{+0.4}_{-0.53}$	<-6.27	$-3.72^{+0.38}_{-0.5}$	<-4.34	...
$\log(\text{CO}_2)$	<-5.37	<-6.44	<-5.88	<-6.51	<-4.86	...
$\log(\text{TiO})$	<-9.05	<-9.65	<-5.57	...
$\log(\text{VO})$	<-9.41	<-10.4	<-7.66	...
$\log(\text{FeH})$	$-9.56^{+0.3}_{-0.45}$	<-10.69	<-7.69	...
$\log(e^-)$	$-6.56^{+0.06}_{-0.06}$	<-10.33	<-7.3	...
$\log(Z)$	$-1.52^{+0.85}_{-0.85}$	$-0.74^{+0.48}_{-0.48}$	$-2.74^{+0.74}_{-0.74}$	$-0.69^{+0.46}_{-0.46}$	$1.97^{+0.03}_{-0.05}$	$-0.99^{+0.02}_{-0.01}$	$0.3^{+0.53}_{-0.53}$	$0.04^{+0.77}_{-0.69}$
C/O	$0.66^{+0.35}_{-0.35}$	$0.95^{+0.13}_{-0.13}$	$0.73^{+0.4}_{-0.4}$	$0.96^{+0.11}_{-0.11}$	$0.77^{+0.03}_{-0.03}$	$0.92^{+0.01}_{-0.01}$	$0.18^{+0.21}_{-0.21}$	$0.43^{+0.3}_{-0.23}$
$\ln(E)$	198.76	236.92	224.61	232.58	187.72	193.11	208.8	210.8
KELT-1 bⁱ								
$\log(\text{H}_2\text{O})$	<-5.9	<-6.0	<-4.9	<-4.5	<-3.9	...
$\log(\text{CH}_4)$	<-4.0	<-7.1	<-5.3	$-6.1^{+1.8}_{-3.5}$	<-4.2	...
$\log(\text{CO})$	<-2.8	<-5.6	<-4.0	<-5.0	<-4.0	...
$\log(\text{CO}_2)$	$-2.3^{+0.2}_{-0.2}$	$-2.3^{+0.2}_{-0.2}$	<-4.0	<-3.5	<-4.0	...
$\log(\text{TiO})$	<-7.2	<-7.1	<-4.2	...
$\log(\text{VO})$	$-6.1^{+0.6}_{-2.3}$	$-6.2^{+0.6}_{-1.7}$	<-3.6	...
$\log(\text{FeH})$	$-5.2^{+0.8}_{-1.1}$	$-6.0^{+0.8}_{-1.8}$	<-3.9	...
$\log(e^-)$	<-3.0	<-2.8	<-4.1	...
$\log(Z)$	$1.1^{+0.2}_{-0.2}$	$1.1^{+0.4}_{-0.4}$	$-1.3^{+1.2}_{-1.2}$	$-1.4^{+1.3}_{-1.3}$	$-0.4^{+0.3}_{-0.2}$	$1.0^{+0.5}_{-0.6}$	$-0.6^{+1.2}_{-1.2}$	$0.5^{+1.0}_{-0.9}$
C/O	$0.5^{+0.1}_{-0.1}$	$0.5^{+0.1}_{-0.1}$	$0.6^{+0.4}_{-0.4}$	$0.6^{+0.6}_{-0.6}$	$1.8^{+0.1}_{-0.2}$	$0.4^{+0.2}_{-0.2}$	$0.5^{+0.5}_{-0.5}$	$1.0^{+0.7}_{-0.5}$
$\ln(E)$	189.3	199.8	193.2	206.9	186.9	198.3	191.1	190.5
KELT-7 b^j								
$\log(\text{H}_2\text{O})$	<-6.9	<-6.1	<-5.3	<-5.5	$-4.4^{+1.2}_{-3.8}$...
$\log(\text{CH}_4)$	<-6.0	<-7.3	<-5.1	$-6.0^{+1.7}_{-3.7}$	<-5.9	...
$\log(\text{CO})$	<-3.5	<-2.9	<-3.9	<-6.2	<-4.4	...
$\log(\text{CO}_2)$	<-4.1	$-2.6^{+0.4}_{-0.6}$	<-4.0	<-7.7	<-5.0	...
$\log(\text{TiO})$	<-6.0	$-5.1^{+0.7}_{-1.1}$	<-5.5	...

Table D1
(Continued)

Parameter	HST	HST+Spitzer (red)	HST	HST+Spitzer (full)	HST	HST+Spitzer (eq)	Transit (free)	Transit (eq)
log(VO)	<-7.1	$-7.0^{+1.5}_{-3.0}$	<-7.1	...
log(FeH)	<-7.6	<-6.2	<-5.5	...
log(e-)	$-2.9^{+0.6}_{-0.7}$	$-3.0^{+0.6}_{-0.8}$	$-3.8^{+1.2}_{-1.9}$...
log(Z)	$-1.2^{+1.2}_{-1.2}$	$0.7^{+0.7}_{-0.7}$	$-1.4^{+1.3}_{-1.3}$	$-1.8^{+0.7}_{-0.7}$	$0.7^{+0.8}_{-0.8}$	$0.7^{+0.7}_{-0.6}$	$-0.9^{+1.1}_{-1.1}$	$0.7^{+0.7}_{-0.9}$
C/O	$0.8^{+0.4}_{-0.4}$	$0.6^{+0.2}_{-0.2}$	$0.7^{+0.4}_{-0.4}$	$0.8^{+0.8}_{-0.8}$	$1.0^{+0.0}_{-0.0}$	$1.6^{+0.3}_{-0.3}$	$0.5^{+0.4}_{-0.4}$	$0.7^{+0.8}_{-0.4}$
ln(E)	208.5	218.1	209.7	222.7	204.6	215.3	200.6	185.8
KELT-9 b^k								
log(H ₂ O)	$-5.5^{+0.1}_{-0.2}$	$-3.9^{+0.5}_{-0.2}$	<-5.2	<-7.0
log(CH ₄)	<-4.1	$-2.9^{+0.2}_{-0.1}$	<-3.7	<-6.1
log(CO)	$-2.3^{+0.2}_{-0.4}$	<-3.2	<-4.0	<-4.7
log(CO ₂)	$-3.7^{+0.6}_{-0.2}$	$-2.1^{+0.0}_{-0.2}$	<-6.2	<-6.2
log(TiO)	$-3.7^{+0.5}_{-0.8}$	$-6.8^{+0.3}_{-0.3}$
log(VO)	$-3.8^{+0.5}_{-0.7}$	$-6.6^{+0.2}_{-0.2}$
log(FeH)	$-5.1^{+1.3}_{-2.8}$	$-8.0^{+1.1}_{-2.0}$
log(e-)	<-4.2	$-4.9^{+0.2}_{-0.1}$
log(Z)	$0.9^{+0.2}_{-0.2}$	$1.2^{+0.4}_{-0.4}$	$-0.3^{+0.6}_{-0.6}$	$-2.5^{+1.0}_{-1.0}$	$-0.3^{+0.2}_{-0.2}$	$1.6^{+0.2}_{-0.4}$
C/O	$0.9^{+0.4}_{-0.1}$	$0.7^{+0.4}_{-0.4}$	$0.5^{+0.6}_{-0.6}$	$0.6^{+0.5}_{-0.5}$	$1.0^{+0.0}_{-0.0}$	$1.1^{+0.6}_{-0.6}$
ln(E)	183.0	147.6	207.1	214.2	169.3	-2844.3
Kepler-13A b^l								
log(H ₂ O)	$-4.1^{+1.5}_{-0.5}$	$-3.9^{+0.8}_{-0.5}$	$-2.7^{+0.5}_{-0.9}$	$-3.2^{+0.8}_{-0.7}$
log(CH ₄)	<-5.7	<-5.6	<-4.8	<-5.5
log(CO)	<-4.4	<-5.2	<-4.2	<-4.7
log(CO ₂)	<-4.6	<-6.7	<-4.3	<-6.4
log(TiO)	$-7.6^{+1.8}_{-2.3}$	<-6.5
log(VO)	<-7.2	<-7.4
log(FeH)	<-7.2	<-7.4
log(e-)	<-5.1	<-5.4
log(Z)	$-0.5^{+0.8}_{-0.8}$	$-0.6^{+0.7}_{-0.7}$	$0.3^{+0.6}_{-0.6}$	$-0.1^{+0.7}_{-0.7}$	$-0.2^{+1.1}_{-0.5}$	$-0.1^{+0.8}_{-0.5}$
C/O	$0.3^{+0.3}_{-0.3}$	$0.2^{+0.3}_{-0.3}$	$0.2^{+0.3}_{-0.3}$	$0.2^{+0.3}_{-0.3}$	$0.5^{+0.2}_{-0.2}$	$0.4^{+0.2}_{-0.2}$
ln(E)	114.2	126.9	113.3	126.4	115.6	128.2
TrES-3 b^m								
log(H ₂ O)	$-3.6^{+1.1}_{-0.9}$	<-7.5	$-2.6^{+0.4}_{-0.6}$	<-7.7
log(CH ₄)	<-5.2	<-7.9	<-4.5	<-8.0
log(CO)	<-4.8	<-5.1	<-4.0	<-2.8
log(CO ₂)	<-4.8	<-6.8	<-4.3	<-6.0
log(TiO)	<-5.9	<-6.6
log(VO)	<-7.3	$-8.9^{+1.0}_{-1.9}$
log(FeH)	$-6.9^{+1.1}_{-2.6}$	$-7.9^{+0.5}_{-1.3}$
log(e-)	<-4.2	<-9.1
log(Z)	$-0.4^{+0.9}_{-0.9}$	$-2.3^{+1.4}_{-1.4}$	$0.4^{+0.5}_{-0.5}$	$-1.5^{+1.7}_{-1.7}$	$-0.3^{+0.9}_{-0.5}$	$1.2^{+0.5}_{-0.6}$
C/O	$0.2^{+0.3}_{-0.3}$	$0.8^{+0.4}_{-0.4}$	$0.2^{+0.3}_{-0.3}$	$0.7^{+0.4}_{-0.4}$	$0.6^{+0.2}_{-0.3}$	$1.6^{+0.3}_{-0.3}$
ln(E)	116.5	130.8	117.7	131.2	118.7	129.7
WASP-4 bⁿ								
log(H ₂ O)	<-5.8	<-6.4	<-4.5	<-5.2
log(CH ₄)	<-3.5	<-7.6	<-4.3	<-5.9
log(CO)	<-4.4	<-3.9	<-4.0	<-3.9
log(CO ₂)	<-5.1	<-6.3	<-3.3	$-3.7^{+0.9}_{-3.5}$
log(TiO)	$-6.2^{+1.3}_{-3.0}$	$-6.7^{+1.5}_{-3.2}$
log(VO)	<-6.5	<-7.0
log(FeH)	<-6.3	<-6.8
log(e-)	$-5.7^{+2.6}_{-3.7}$	<-5.9
log(Z)	$-1.7^{+1.4}_{-1.4}$	$-2.0^{+1.3}_{-1.3}$	$-1.0^{+1.3}_{-1.3}$	$-0.3^{+1.1}_{-1.1}$	$0.2^{+1.1}_{-0.8}$	$1.2^{+0.5}_{-0.6}$
C/O	$0.8^{+0.5}_{-0.5}$	$0.8^{+0.3}_{-0.3}$	$0.6^{+0.5}_{-0.5}$	$0.6^{+0.3}_{-0.3}$	$1.5^{+0.3}_{-0.4}$	$1.5^{+0.3}_{-0.4}$
ln(E)	119.6	131.7	119.8	130.4	121.1	131.5
WASP-12 b^o								
log(H ₂ O)	<-7.0	<-7.7	<-4.0	<-5.7	$-2.8^{+0.5}_{-0.6}$...

Table D1
(Continued)

Parameter	HST	HST+Spitzer (red)	HST	HST+Spitzer (full)	HST	HST+Spitzer (eq)	Transit (free)	Transit (eq)
log(CH ₄)	<-5.2	<-6.2	-4.4 ^{+1.9} _{-4.7}	<-4.7	<-5.6	...
log(CO)	<-2.9	<-5.1	<-4.0	<-3.9	<-4.7	...
log(CO ₂)	<-5.7	-7.1 ^{+1.2} _{-1.5}	<-3.9	-3.2 ^{+0.7} _{-1.2}	<-4.8	...
log(TiO)	<-5.8	<-6.2	<-7.1	...
log(VO)	-7.7 ^{+1.8} _{-2.3}	<-6.2	<-7.1	...
log(FeH)	-7.3 ^{+1.9} _{-2.6}	-6.2 ^{+1.3} _{-2.6}	<-5.8	...
log(e ⁻)	-6.1 ^{+2.4} _{-3.1}	<-5.6	<-5.3	...
log(Z)	-1.3 ^{+1.5} _{-1.5}	-2.6 ^{+1.0} _{-1.0}	-1.1 ^{+1.3} _{-1.3}	0.1 ^{+0.8} _{-0.8}	-0.0 ^{+0.9} _{-0.6}	-0.1 ^{+1.3} _{-0.7}	0.2 ^{+0.6} _{-0.6}	0.2 ^{+0.9} _{-0.8}
C/O	0.9 ^{+0.4} _{-0.4}	0.9 ^{+0.4} _{-0.4}	0.7 ^{+0.6} _{-0.6}	0.6 ^{+0.3} _{-0.3}	0.7 ^{+0.2} _{-0.2}	1.0 ^{+0.0} _{-0.0}	0.2 ^{+0.2} _{-0.2}	0.5 ^{+0.3} _{-0.3}
ln(<i>E</i>)	119.7	139.3	119.2	140.1	118.5	132.6	196.0	197.3
WASP-18 b^p								
log(H ₂ O)	<-7.4	<-7.4	-3.3 ^{+0.4} _{-0.4}	-3.3 ^{+0.2} _{-0.4}	<-4.2	...
log(CH ₄)	<-4.8	<-7.3	<-5.4	<-5.5	<-3.8	...
log(CO)	-2.1 ^{+0.1} _{-0.1}	-2.1 ^{+0.1} _{-0.1}	-7.9 ^{+1.8} _{-1.8}	<-4.8	<-4.2	...
log(CO ₂)	-3.9 ^{+0.4} _{-5.2}	-3.4 ^{+0.2} _{-0.2}	<-4.4	<-6.0	<-4.5	...
log(TiO)	<-7.3	<-7.4	<-4.1	...
log(VO)	<-7.2	<-7.0	<-5.2	...
log(FeH)	-8.9 ^{+1.4} _{-1.7}	<-7.5	<-4.1	...
log(e ⁻)	-3.2 ^{+0.4} _{-0.4}	-3.2 ^{+0.3} _{-0.3}	<-3.8	...
log(Z)	1.0 ^{+0.1} _{-0.1}	1.0 ^{+0.1} _{-0.1}	-0.2 ^{+0.4} _{-0.4}	-0.2 ^{+0.3} _{-0.3}	-0.1 ^{+0.3} _{-0.4}	0.2 ^{+0.2} _{-0.2}	-0.9 ^{+1.3} _{-1.3}	0.4 ^{+1.1} _{-0.9}
C/O	1.0 ^{+0.0} _{-0.0}	0.9 ^{+0.0} _{-0.0}	0.2 ^{+0.2} _{-0.2}	0.2 ^{+0.2} _{-0.2}	0.9 ^{+0.0} _{-0.0}	0.9 ^{+0.0} _{-0.0}	0.6 ^{+0.5} _{-0.5}	1.1 ^{+0.6} _{-0.6}
ln(<i>E</i>)	197.6	215.9	207.3	237.4	207.0	232.8	209.8	209.8
WASP-19 b^q								
log(H ₂ O)	<-4.8	-5.4 ^{+0.8} _{-2.0}	-3.2 ^{+0.7} _{-3.0}	-3.0 ^{+0.6} _{-1.0}	-2.7 ^{+0.5} _{-0.7}	...
log(CH ₄)	<-6.1	<-6.6	<-3.9	<-4.8	<-5.6	...
log(CO)	<-4.2	<-4.3	<-4.2	<-3.8	<-3.8	...
log(CO ₂)	<-5.2	<-6.5	<-4.2	-6.0 ^{+1.9} _{-3.5}	<-4.5	...
log(TiO)	<-5.9	<-6.7	<-6.5	...
log(VO)	<-6.4	<-6.5	<-7.2	...
log(FeH)	-7.0 ^{+1.8} _{-2.7}	<-5.6	<-5.6	...
log(e ⁻)	-6.1 ^{+2.4} _{-3.2}	<-3.8	<-5.0	...
log(Z)	-1.6 ^{+1.2} _{-1.2}	-1.8 ^{+1.0} _{-1.0}	-0.2 ^{+1.1} _{-1.1}	0.0 ^{+0.9} _{-0.9}	0.7 ^{+0.8} _{-0.9}	0.6 ^{+0.8} _{-0.8}	0.3 ^{+0.6} _{-0.6}	0.5 ^{+0.8} _{-0.9}
C/O	0.7 ^{+0.4} _{-0.4}	0.5 ^{+0.4} _{-0.4}	0.4 ^{+0.4} _{-0.4}	0.3 ^{+0.3} _{-0.3}	0.7 ^{+0.7} _{-0.3}	0.5 ^{+0.2} _{-0.2}	0.2 ^{+0.2} _{-0.2}	0.4 ^{+0.3} _{-0.2}
ln(<i>E</i>)	170.9	194.9	171.4	195.0	172.0	196.3	169.4	170.4
WASP-33 b^r								
log(H ₂ O)	-5.8 ^{+0.1} _{-0.1}	-5.8 ^{+0.1} _{-0.1}	-5.4 ^{+0.2} _{-0.2}	-5.4 ^{+0.2} _{-0.3}
log(CH ₄)	<-7.4	<-7.3	<-6.1	<-6.6
log(CO)	-2.6 ^{+0.2} _{-0.2}	-2.5 ^{+0.3} _{-0.3}	<-5.0	<-5.0
log(CO ₂)	<-4.7	-4.4 ^{+0.2} _{-0.3}	<-5.7	<-6.9
log(TiO)	-7.4 ^{+0.5} _{-0.3}	-7.2 ^{+0.9} _{-0.3}
log(VO)	<-8.5	-9.2 ^{+1.1} _{-1.7}
log(FeH)	<-9.8	<-9.6
log(e ⁻)	-4.7 ^{+0.3} _{-0.2}	-4.6 ^{+0.6} _{-0.2}
log(Z)	0.5 ^{+0.2} _{-0.2}	0.6 ^{+0.3} _{-0.3}	-1.9 ^{+0.7} _{-0.7}	-2.0 ^{+0.7} _{-0.7}	-0.9 ^{+0.1} _{-0.1}	-0.7 ^{+0.4} _{-0.2}
C/O	1.0 ^{+0.0} _{-0.0}	1.0 ^{+0.0} _{-0.0}	0.5 ^{+0.4} _{-0.4}	0.4 ^{+0.4} _{-0.4}	0.9 ^{+0.0} _{-0.0}	0.9 ^{+0.0} _{-0.0}
ln(<i>E</i>)	15.7	26.0	54.8	67.4	67.9	77.0
WASP-43 b^s								
log(H ₂ O)	-4.3 ^{+0.8} _{-0.6}	-4.0 ^{+0.4} _{-0.4}	<-7.5	-3.7 ^{+0.5} _{-0.4}	-4.5 ^{+2.0} _{-4.5}	...
log(CH ₄)	<-3.9	<-7.5	<-6.6	<-7.2	<-4.8	...
log(CO)	<-3.3	<-3.0	<-4.0	<-3.4	<-4.1	...
log(CO ₂)	<-3.0	-2.6 ^{+0.4} _{-0.7}	<-5.5	-2.4 ^{+0.3} _{-0.4}	<-4.5	...
log(TiO)	<-8.2	<-7.0	<-4.3	...
log(VO)	-9.0 ^{+1.0} _{-1.7}	<-8.7	<-5.8	...
log(FeH)	-7.8 ^{+0.7} _{-0.4}	<-8.7	<-5.1	...
log(e ⁻)	<-7.7	<-7.8	<-4.1	...
log(Z)	-0.3 ^{+0.9} _{-0.9}	0.8 ^{+0.5} _{-0.5}	-1.9 ^{+1.3} _{-1.3}	1.0 ^{+0.4} _{-0.4}	0.5 ^{+1.2} _{-1.3}	1.8 ^{+0.2} _{-0.4}	-0.4 ^{+1.2} _{-1.2}	0.4 ^{+0.9} _{-0.9}
C/O	0.6 ^{+0.3} _{-0.3}	0.5 ^{+0.2} _{-0.2}	0.8 ^{+0.4} _{-0.4}	0.5 ^{+0.1} _{-0.1}	0.5 ^{+0.3} _{-0.2}	0.7 ^{+0.1} _{-0.2}	0.5 ^{+0.5} _{-0.5}	0.6 ^{+0.8} _{-0.4}
ln(<i>E</i>)	195.8	205.5	196.1	204.5	193.9	201.9	202.4	199.0

Table D1
(Continued)

Parameter	HST	HST+Spitzer	HST	HST+Spitzer	HST	HST+Spitzer	Transit (free)	Transit (eq)
		(red)		(full)		(eq)		
WASP-74 b^t								
log(H ₂ O)	-7.3 ^{+1.4} _{-3.0}	-7.4 ^{+1.6} _{-2.9}	<-5.1	-2.8 ^{+0.5} _{-0.6}	-3.9 ^{+1.3} _{-4.7}	...
log(CH ₄)	<-6.3	-6.4 ^{+0.6} _{-0.6}	<-4.2	-2.6 ^{+0.4} _{-0.7}	<-4.6	...
log(CO)	<-4.9	<-6.3	<-3.9	<-3.5	<-4.1	...
log(CO ₂)	<-5.5	<-8.3	<-3.9	-6.3 ^{+2.0} _{-3.5}	<-4.3	...
log(TiO)	<-5.9	<-5.9	<-4.8	...
log(VO)	<-6.4	<-6.8	<-6.1	...
log(FeH)	<-4.9	<-6.2	-6.0 ^{+1.9} _{-2.9}	...
log(e ⁻)	-3.4 ^{+0.9} _{-1.8}	<-4.6	<-5.1	...
log(Z)	-2.1 ^{+1.1} _{-1.1}	-2.7 ^{+0.8} _{-0.8}	-1.2 ^{+1.3} _{-1.3}	0.4 ^{+0.5} _{-0.5}	1.0 ^{+0.6} _{-1.0}	0.6 ^{+0.9} _{-1.2}	-0.4 ^{+1.2} _{-1.2}	0.2 ^{+1.1} _{-0.9}
C/O	0.7 ^{+0.5} _{-0.5}	0.8 ^{+0.7} _{-0.7}	0.7 ^{+0.5} _{-0.5}	1.2 ^{+0.7} _{-0.7}	0.7 ^{+0.9} _{-0.4}	1.4 ^{+0.4} _{-0.3}	0.4 ^{+0.5} _{-0.5}	0.6 ^{+0.7} _{-0.3}
ln(<i>E</i>)	202.8	216.3	202.5	215.4	202.0	213.6	196.9	196.7
WASP-76 b^u								
log(H ₂ O)	<-6.9	<-5.4	-2.9 ^{+0.4} _{-0.6}	-3.1 ^{+0.4} _{-0.6}	-2.9 ^{+0.4} _{-0.6}	...
log(CH ₄)	-3.4 ^{+0.3} _{-0.3}	-2.9 ^{+0.4} _{-0.2}	<-4.5	<-6.3	<-5.5	...
log(CO)	-5.6 ^{+2.3} _{-2.5}	<-4.6	<-4.0	<-3.8	<-6.6	...
log(CO ₂)	<-6.4	<-6.9	<-4.4	<-4.9	<-5.1	...
log(TiO)	-4.8 ^{+0.5} _{-1.0}	-4.7 ^{+0.5} _{-0.7}	-8.0 ^{+1.7} _{-2.0}	...
log(VO)	<-7.7	<-8.1	<-7.1	...
log(FeH)	<-6.6	<-5.4	<-7.3	...
log(e ⁻)	<-3.7	<-4.9	<-5.2	...
log(Z)	-1.7 ^{+1.4} _{-1.4}	-2.1 ^{+1.2} _{-1.2}	0.2 ^{+0.5} _{-0.5}	0.1 ^{+0.6} _{-0.6}	0.8 ^{+0.8} _{-1.1}	-0.1 ^{+0.6} _{-0.5}	0.1 ^{+0.5} _{-0.5}	1.7 ^{+0.2} _{-0.3}
C/O	1.4 ^{+0.6} _{-0.6}	1.7 ^{+0.5} _{-0.5}	0.3 ^{+0.3} _{-0.3}	0.3 ^{+0.3} _{-0.3}	0.7 ^{+0.4} _{-0.4}	1.2 ^{+0.4} _{-0.1}	0.1 ^{+0.2} _{-0.2}	0.5 ^{+0.2} _{-0.3}
ln(<i>E</i>)	183.9	201.2	189.5	199.7	188.5	203.0	197.7	204.6
WASP-77 A b^v								
log(H ₂ O)	-4.1 ^{+0.5} _{-0.4}	-4.1 ^{+1.7} _{-0.6}	-3.9 ^{+0.9} _{-0.5}	-3.5 ^{+0.6} _{-0.6}
log(CH ₄)	<-6.4	-4.7 ^{+1.6} _{-1.0}	<-5.9	-4.2 ^{+0.7} _{-0.8}
log(CO)	<-4.3	<-3.8	<-3.9	<-2.8
log(CO ₂)	<-5.0	-4.3 ^{+1.3} _{-1.9}	<-3.5	-3.8 ^{+0.7} _{-1.2}
log(TiO)	-6.0 ^{+0.9} _{-0.4}	-5.3 ^{+0.7} _{-0.8}
log(VO)	<-9.0	<-8.7
log(FeH)	<-8.3	<-8.1
log(e ⁻)	<-7.9	<-7.6
log(Z)	-0.8 ^{+0.5} _{-0.5}	-0.2 ^{+1.0} _{-1.0}	-0.3 ^{+0.8} _{-0.8}	0.2 ^{+0.6} _{-0.6}	1.3 ^{+0.4} _{-0.5}	-0.6 ^{+0.3} _{-0.2}
C/O	0.3 ^{+0.3} _{-0.3}	0.4 ^{+0.2} _{-0.2}	0.4 ^{+0.3} _{-0.3}	0.5 ^{+0.2} _{-0.2}	0.5 ^{+0.2} _{-0.3}	0.8 ^{+0.1} _{-0.1}
ln(<i>E</i>)	197.0	206.0	202.5	212.5	200.6	209.0
WASP-79 b^w								
log(H ₂ O)	-4.4 ^{+0.9} _{-0.7}	-3.4 ^{+0.7} _{-0.8}	<-4.8	<-4.2	-2.6 ^{+0.4} _{-0.5}	...
log(CH ₄)	-5.6 ^{+2.2} _{-3.9}	<-3.0	<-5.0	<-6.0	<-5.9	...
log(CO)	<-3.1	<-3.8	<-3.9	<-4.2	<-4.6	...
log(CO ₂)	<-3.4	<-5.7	<-4.2	<-7.0	<-4.9	...
log(TiO)	<-6.7	<-6.8	<-5.4	...
log(VO)	-5.1 ^{+0.6} _{-0.8}	-5.3 ^{+0.6} _{-0.6}	<-7.6	...
log(FeH)	-5.3 ^{+0.7} _{-1.2}	-5.7 ^{+0.8} _{-1.6}	<-5.6	...
log(e ⁻)	<-5.6	<-5.4	-5.9 ^{+2.4} _{-2.8}	...
log(Z)	-0.4 ^{+0.9} _{-0.9}	-0.1 ^{+0.7} _{-0.7}	-1.1 ^{+1.0} _{-1.0}	-1.5 ^{+1.0} _{-1.0}	1.1 ^{+0.6} _{-0.9}	0.2 ^{+0.8} _{-0.7}	0.5 ^{+0.4} _{-0.4}	0.5 ^{+0.9} _{-0.9}
C/O	0.8 ^{+0.6} _{-0.6}	0.8 ^{+0.7} _{-0.7}	0.6 ^{+0.4} _{-0.4}	0.5 ^{+0.5} _{-0.5}	0.4 ^{+0.2} _{-0.2}	0.3 ^{+0.2} _{-0.2}	0.1 ^{+0.2} _{-0.2}	0.3 ^{+0.3} _{-0.2}
ln(<i>E</i>)	136.9	151.9	141.9	156.4	136.0	151.0	191.7	184.6
WASP-103 b^x								
log(H ₂ O)	<-7.4	<-6.9	<-5.4	<-5.4	<-3.7	...
log(CH ₄)	<-7.1	<-5.8	<-4.1	-6.4 ^{+2.5} _{-3.1}	<-5.4	...
log(CO)	<-5.4	<-3.8	<-3.8	<-4.1	<-4.7	...
log(CO ₂)	<-4.5	-2.3 ^{+0.2} _{-0.5}	<-4.2	-3.6 ^{+1.0} _{-1.6}	<-4.4	...
log(TiO)	<-6.2	<-6.8	-4.4 ^{+1.3} _{-3.9}	...
log(VO)	-4.8 ^{+0.5} _{-0.6}	-5.8 ^{+0.9} _{-2.5}	-4.2 ^{+1.0} _{-1.1}	...
log(FeH)	-6.1 ^{+1.3} _{-2.7}	-7.6 ^{+2.0} _{-2.4}	<-4.9	...
log(e ⁻)	<-3.5	-3.4 ^{+0.9} _{-3.8}	-6.0 ^{+2.6} _{-3.4}	...

Table D1
(Continued)

Parameter	HST	HST+Spitzer (red)	HST	HST+Spitzer (full)	HST	HST+Spitzer (eq)	Transit (free)	Transit (eq)
log(<i>Z</i>)	$-2.1^{+1.1}_{-1.1}$	$0.9^{+0.5}_{-0.5}$	$-1.0^{+0.9}_{-0.9}$	$-0.3^{+1.1}_{-1.1}$	$-0.4^{+0.7}_{-0.4}$	$-0.3^{+0.7}_{-0.4}$	$-0.3^{+0.9}_{-0.9}$	$-0.4^{+0.7}_{-0.5}$
C/O	$0.7^{+0.4}_{-0.4}$	$0.5^{+0.1}_{-0.1}$	$0.6^{+0.5}_{-0.5}$	$0.6^{+0.3}_{-0.3}$	$1.0^{+0.0}_{-0.0}$	$1.0^{+0.0}_{-0.0}$	$0.3^{+0.4}_{-0.4}$	$0.6^{+0.4}_{-0.4}$
ln(<i>E</i>)	187.1	199.2	189.8	201.6	184.7	198.0	173.4	166.3
WASP-121 b^v								
log(H ₂ O)	< -8.3	< -8.1	$-4.2^{+0.4}_{-1.4}$	< -4.6	$-2.7^{+0.5}_{-0.7}$...
log(CH ₄)	< -7.2	< -6.6	< -5.4	< -6.8	< -6.0	...
log(CO)	< -5.0	$-6.2^{+2.3}_{-3.5}$	< -4.2	< -3.6	< -4.5	...
log(CO ₂)	< -6.2	< -6.7	< -4.5	< -6.4	< -4.8	...
log(TiO)	< -7.7	$-4.5^{+0.3}_{-0.5}$	< -6.3	...
log(VO)	$-6.9^{+0.5}_{-2.6}$	$-4.8^{+0.3}_{-0.4}$	$-7.9^{+1.5}_{-2.4}$...
log(FeH)	< -8.5	< -7.4	< -7.1	...
log(e ⁻)	$-2.8^{+0.5}_{-0.7}$	$-4.2^{+0.7}_{-0.7}$	$-5.2^{+1.9}_{-2.6}$...
log(<i>Z</i>)	$-2.4^{+1.0}_{-1.0}$	$-2.0^{+1.2}_{-1.2}$	$-0.9^{+0.8}_{-0.8}$	$-0.9^{+0.6}_{-0.6}$	$0.7^{+0.9}_{-0.7}$	$1.7^{+0.2}_{-0.3}$	$0.3^{+0.5}_{-0.5}$	$0.5^{+1.0}_{-0.9}$
C/O	$0.8^{+0.4}_{-0.4}$	$0.9^{+0.4}_{-0.4}$	$0.5^{+0.4}_{-0.4}$	$0.4^{+0.4}_{-0.4}$	$1.6^{+0.3}_{-0.2}$	$1.3^{+0.1}_{-0.1}$	$0.2^{+0.2}_{-0.2}$	$0.4^{+0.4}_{-0.2}$
ln(<i>E</i>)	198.1	306.7	201.4	313.8	183.0	289.5	193.4	189.6

Notes.

^a CoRoT-1 b: For comparison, the HST blackbody fit obtains ln(*E*) = 112.5, the HST+Spitzer blackbody fit obtains ln(*E*) = 125.5, and the featureless transit fit obtains ln(*E*) = 96.4.

^b HAT-P-2 b: For comparison, the HST blackbody fit obtains ln(*E*) = 215.5, and the HST+Spitzer blackbody fit obtains ln(*E*) = 243.3.

^c HAT-P-7 b: For comparison, the HST blackbody fit obtains ln(*E*) = 207.2, the HST+Spitzer blackbody fit obtains ln(*E*) = 225.3, and the featureless transit fit obtains ln(*E*) = 156.7.

^d HAT-P-32 b: For comparison, the HST blackbody fit obtains ln(*E*) = 174.1, the HST+Spitzer blackbody fit obtains ln(*E*) = 188.8, and the featureless transit fit obtains ln(*E*) = 157.2.

^e HAT-P-41 b: For comparison, the HST blackbody fit obtains ln(*E*) = 185.1, the HST+Spitzer blackbody fit obtains ln(*E*) = 194.7, and the featureless transit fit obtains ln(*E*) = 182.5.

^f HAT-P-70 b: For comparison, the HST blackbody fit obtains ln(*E*) = 191.6.

^g HD 189733b: For comparison, the HST blackbody fit obtains ln(*E*) = 146.4, the HST+Spitzer blackbody fit obtains ln(*E*) = 137.0, and the featureless transit fit obtains ln(*E*) = 184.6.

^h HD 209458b: For comparison, the HST blackbody fit obtains ln(*E*) = 9.3, the HST+Spitzer blackbody fit obtains ln(*E*) = -400.0, and the featureless transit fit obtains ln(*E*) = 190.0.

ⁱ KELT-1 b: For comparison, the HST blackbody fit obtains ln(*E*) = 177.7, the HST+Spitzer blackbody fit obtains ln(*E*) = 192.2, and the featureless transit fit obtains ln(*E*) = 190.5.

^j KELT-7 b: For comparison, the HST blackbody fit obtains ln(*E*) = 182.7, the HST+Spitzer blackbody fit obtains ln(*E*) = 144.1, and the featureless transit fit obtains ln(*E*) = 185.7.

^k KELT-9 b: For comparison, the HST blackbody fit obtains ln(*E*) = 8.9, and the HST+Spitzer blackbody fit obtains ln(*E*) = 13.6.

^l Kepler-13 A b: For comparison, the HST blackbody fit obtains ln(*E*) = 101.3, and the HST+Spitzer blackbody fit obtains ln(*E*) = 115.0.

^m TrES-3 b: For comparison, the HST blackbody fit obtains ln(*E*) = 106.9, and the HST+Spitzer blackbody fit obtains ln(*E*) = 118.7.

ⁿ WASP-4 b: For comparison, the HST blackbody fit obtains ln(*E*) = 119.0, and the HST+Spitzer blackbody fit obtains ln(*E*) = 124.3.

^o WASP-12 b: For comparison, the HST blackbody fit obtains ln(*E*) = 119.1, the HST+Spitzer blackbody fit obtains ln(*E*) = 117.5, and the featureless transit fit obtains ln(*E*) = 168.9.

^p WASP-18 b: For comparison, the HST blackbody fit obtains ln(*E*) = 146.9, the HST+Spitzer blackbody fit obtains ln(*E*) = 172.7, and the featureless transit fit obtains ln(*E*) = 209.7.

^q WASP-19 b: For comparison, the HST blackbody fit obtains ln(*E*) = 171.1, the HST+Spitzer blackbody fit obtains ln(*E*) = 189.2, and the featureless transit fit obtains ln(*E*) = 164.8.

^r WASP-33 b: For comparison, the HST blackbody fit obtains ln(*E*) = -178.0, and the HST+Spitzer blackbody fit obtains ln(*E*) = -169.4.

^s WASP-43 b: For comparison, the HST blackbody fit obtains ln(*E*) = 183.1, the HST+Spitzer blackbody fit obtains ln(*E*) = 163.9, and the featureless transit fit obtains ln(*E*) = 196.8.

^t WASP-74 b: For comparison, the HST blackbody fit obtains ln(*E*) = 200.6, the HST+Spitzer blackbody fit obtains ln(*E*) = 192.5, and the featureless transit fit obtains ln(*E*) = 195.7.

^u WASP-76 b: For comparison, the HST blackbody fit obtains ln(*E*) = 180.8, the HST+Spitzer blackbody fit obtains ln(*E*) = 195.0, and the featureless transit fit obtains ln(*E*) = 175.0.

^v WASP-77 A b: For comparison, the HST blackbody fit obtains ln(*E*) = 157.0, and the HST+Spitzer blackbody fit obtains ln(*E*) = 65.7.

^w WASP-79 b: For comparison, the HST blackbody fit obtains ln(*E*) = 124.2, the HST+Spitzer blackbody fit obtains ln(*E*) = 137.9 and the featureless transit fit obtains ln(*E*) = 172.9.

^x WASP-103 b: For comparison, the HST blackbody fit obtains ln(*E*) = 174.0, the HST+Spitzer blackbody fit obtains ln(*E*) = 185.3, and the featureless transit fit obtains ln(*E*) = 161.8.

^y WASP-121 b: For comparison, the HST blackbody fit obtains ln(*E*) = 91.1, the HST+Spitzer blackbody fit obtains ln(*E*) = 140.0, and the featureless transit fit obtains ln(*E*) = 173.2.

(This table is available in machine-readable form.)

This planet, which was extensively observed with Spitzer, was not included in the population study from G20. We therefore considered the observations from Christiansen et al. (2010), which cover the wavelength range from 3.6 to 8 μ m. In their paper, on top of the standard MCMC technique, they used

the “rosary bead” residual permutation method (Winn et al. 2008) to quantify potential remaining systematic errors. Their results highlighted differences in the 8 μ m point, so we use the 8 μ m channel from the rosary technique, as suggested in Christiansen et al. (2010).

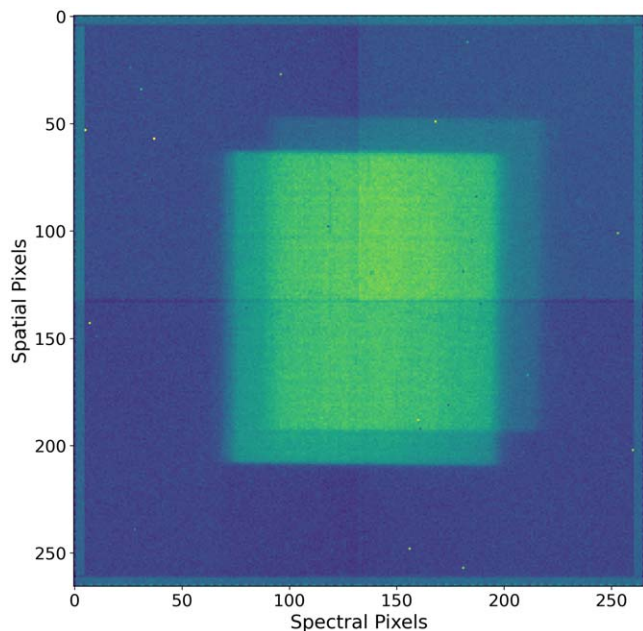


Figure D3. Example spatial scan from the second eclipse observation of WASP-77 A b. The contributions from WASP-77 A and WASP-77 B can clearly be seen to overlap.

We performed our standardised retrieval study of this planet. Analyzing the full HST-only run does not clearly favor a molecule and leads to an isothermal atmosphere. When Spitzer is included, however, additional constraints can be extracted from the four Spitzer photometric channels. The retrievals now include some evidence for the subsolar abundance of H_2O , high abundance of CO_2 , and the presence of FeH. The associated temperature profile to best fit the HST+Spitzer data set contains a localized thermal inversion. While the recovered temperature reaches 2500 K, we do not find evidence for H^- opacities. Comparing the Bayesian evidence of the free models, it is not possible to validate the detection of molecular species from the HST-only data set, thus demonstrating that the HST spectrum is, in this case, uninformative and consistent with a blackbody. It is only when Spitzer is included that we find strong evidence in favor of the models with molecular opacities. The derived metallicity for the free models is only constrained when HST+Spitzer data are considered, favoring a supersolar metallicity. Due to the detection of large abundances of CO_2 in the model that includes Spitzer data, the derived C/O takes a value close to 0.5. When testing the equilibrium retrievals, the thermal profile is decreasing with altitude if Spitzer is included or possesses a localized thermal inversion if only HST is considered. In both runs, the additional constraints of this chemical model do not allow to clarify the metallicity of this atmosphere, but the associated C/O is restricted to high values. Looking at the spectra, the solution obtained by the equilibrium chemistry retrievals obtains a much worse fit of the observed Spitzer data, which is also confirmed by the lower Bayesian evidence.

At the terminator, we do not recover the presence of any molecular species, the spectrum consistent with being flat. The planet could therefore have high-altitude clouds at the terminator.

D.4. Individual Analysis of HAT-P-32 b

The planet HAT-P-32 b was first reported in 2011 (Hartman et al. 2011) and presents a particularly large radius: $1.98 R_J$ (Wang et al. 2019). The planet eclipse was then observed with HST-WFC3 (Nikolov et al. 2018) and Spitzer (Zhao et al. 2014). Both analyses suggested that thermal inversions could be present on this planet. The terminator region was also observed with HST-WFC3, and it is consistent with a significant water feature at $1.4 \mu\text{m}$ (Damiano et al. 2017; Tsiaras et al. 2018). These data were analyzed together with HST STIS and Spitzer-IRAC data, which showed a thick cloud layer and a supersolar metallicity (Alam et al. 2020).

Because the transmission spectrum (PN: 14260, PI: Deming et al. 2015) was part of the Tsiaras et al. 2018 study and was already reduced with Iraclis, we took the spectrum “as is,” directly from this paper. For the eclipse (PN: 14767, PI: Sing et al. 2016b), we reanalyzed the raw images using Iraclis following our standardized reduction technique. We include the Spitzer data from Zhao et al. (2014) in our spectral retrieval analysis.

For the eclipse, we show the fitted spectra, the temperature profiles, and the posteriors in Figure Set D1. In the full runs, the recovered temperature profile is slightly inverted and is similar between the HST and HST+Spitzer runs. In addition, both runs are consistent with H^- , which could be causing the observed thermal inversion. We note, however, that the recovered temperatures for this atmosphere are below the predictions for H_2 dissociation in Parmentier et al. (2018). Such results are surprising, but given the small differences in Bayesian evidence with the reduced model, we believe this detection to be marginal. The addition of the Spitzer photometric points lead to some hints for VO and CH_4 , but these detections also remain weak, with large tails in the posterior distributions. When comparing the full runs to the reduced runs, the inclusion of the Spitzer points favors the models with optical absorbers, but this is not the case when only HST is considered. For the free runs, we find that the full runs prefer a subsolar-metallicity case, which contrasts with the results from equilibrium chemistry retrievals. In terms of C/O, solar values are also allowed with large uncertainties for the full runs, while equilibrium chemistry retrievals require a supersolar C/O that is unlikely from a planetary formation perspective. The equilibrium chemistry runs also feature a decreasing temperature structure, as opposed to the full free runs. In any case, looking at the Bayesian evidence obtained by the reference blackbody fits, we conclude on the likely presence of molecular absorption on this planet.

For the transmission, which is shown in Figure Set D2, our analysis recovers a large abundance of water vapor and high-altitude opaque clouds, consistent with previous analyses of the planet. We also find marginal evidence for FeH absorption, which is surprising as it is not detected on the dayside. This might be linked to circulation processes that prevent the molecule from being seen on the dayside, or it could come from an unfortunate fitting of the scattered data points between 1.1 and $1.3 \mu\text{m}$. Constraints on the other near-optical absorbers are however relatively strong, with abundances restricted to less than 10^{-5} for all of them. In terms of elemental ratios, both free and equilibrium chemistry are consistent with a large range of metallicities (from sub to supersolar). However, the C/O for

the free run is subsolar, which is inconsistent with the equilibrium chemistry scenario.

D.5. Individual Analysis of HAT-P-41 b

In 2012 August the HATnet survey reported the identification of three new inflated, transiting hot Jupiters orbiting bright F-type hosts. One of those systems hosts HAT-P-41 b, which is in fact part of a binary system, with a K-dwarf companion (Hartman et al. 2012; Evans et al. 2016a). The HST-WFC3 transmission spectrum was studied in Tsiaras et al. 2018, finding the presence of water vapor and high-altitude clouds. In 2020, additional transmission data was obtained using the G280 grism (200–400 nm) on board HST/WFC3 and analyzed in conjunction with the Spitzer photometry (3.6 and 4.5 μm). Their best fit of the transmission spectrum, obtained using a grid of self-consistent models, confirmed the presence of clouds and water and contained evidence for molecular absorption from VO/TiO and CO₂ (Wakeford et al. 2020).

As part of our work, we obtained the HST transmission spectrum from Tsiaras et al. 2018 and reduced the G141 observation of the eclipse from the raw data using our Iraclis pipeline (PN: 14767, PI: Sing et al. 2016b). The Spitzer data were obtained from the G20 population study of Spitzer eclipses. We then performed our retrieval analysis of the transit and eclipse spectra with TauREx3 via the Alfnor pipeline.

For the dayside, our full scenarios agreed on a thermal inversion in both HST and HST+Spitzer cases. The solutions display evidence for optical absorbers such as VO or FeH, but there remain large tails indicating the degeneracies between those two molecules. The full runs are, however, not statistically significant as they lead to similar Bayesian evidence to the reduced cases. In the reduced cases, the retrievals do not find evidence for any molecule and seem consistent with emission from continuous CIA and Rayleigh absorption with a decreasing thermal profile. The metallicity for the free cases is solar to subsolar, and as expected from the poor features in this spectrum, the C/O of the planet remains unconstrained. The equilibrium chemistry runs are consistent with a decrease to an isothermal thermal structure, more similar to the free reduced case. For this planet, equilibrium chemistry provides a very good fit for the HST+Spitzer data set, with a $\ln(E)$ comparable to the analogous free runs. Assuming equilibrium chemistry, the atmosphere is found to have a solar-like metallicity but a relatively high C/O.

When analyzing the terminator of the planet, we confirm the results from Tsiaras et al. 2018, finding a strong H₂O feature and evidence for high-altitude clouds. In the WFC3 data, VO/TiO or CO₂ is not detected, suggesting that the additional constraints found in Wakeford et al. (2020) come from the addition of the G280 grism and the Spitzer data. The metallicity of the planet is consistent with solar abundances, while the C/O is difficult to constrain, ranging from subsolar in the free run to solar with large uncertainties in the equilibrium case.

D.6. Individual Analysis of HAT-P-70 b

HAT-P-70 b is a very large ultra-hot Jupiter (1.87 R_J) orbiting an A-type star that was recently detected by TESS and the HATNet program. While radial velocity measurements of the star were performed in the discovery paper Zhou et al. (2019), only an upper limit on the mass of the planet ($M_p < 6.78 M_J$) could be obtained.

The planet was observed again in 2020 at high resolution with the HARPS-N spectrograph (Bello-Arufe et al. 2022). These observations detected a number of atomic and ionic species (Ca II, Cr I, Cr II, Fe I, Fe II, H I, Mg I, Na I, and V I) and constrained further the orbital configuration of the system. The planet is in a highly misaligned orbit.

In 2021 July, the eclipse of HAT-P-70 b was observed with HST as part of the proposal (PN: 16307, PI: Fu et al. 2020). We analyzed the raw images from this proposal using our Iraclis pipeline. Due to the retirement of Spitzer, this planet is the only one in our sample that was not observed with this telescope. We therefore include the results from the HST-only full case in the population study. Additionally, as of today, the planet's mass is still not known precisely. We tested different values, up to 6.78 M_J , to verify the impact of those uncertainties on our retrievals. Due to the geometry in eclipse, we did not find major differences in our test, and we therefore assume a mass of 1 M_J for this study.

From our retrievals, the full model recovers an inverted thermal profile with H⁻ emission. This detection is not decisive as the reduced run is not consistent with this picture and obtains a $\Delta\ln(E) = 3.2$. For the full model, the metallicity is subsolar and the C/O is consistent with solar. While the equilibrium chemistry run also presents a thermal inversion, this retrieval is consistent with a C/O of 1.

D.7. Individual Analysis of HD 189733b

HD 189733b is one of the most-studied exoplanets and was the first planet to exhibit evidence of molecular absorption (Tinetti et al. 2007). The water detection for the Spitzer-IRAC data was subsequently confirmed by transit observations with HST-WFC3 (McCullough et al. 2014), while HST-NICMOS data showed evidence for methane (Swain et al. 2008b).

In eclipse (PN: 12881, PI: McCullough 2012), the HST-WFC3 spectrum was analyzed by Crouzet et al. (2014), which highlighted marginal evidence for water. In their analysis, they combined with the Spitzer data from Charbonneau et al. (2008), which provide photometric data up to 24 μm , a rarity in the exoplanet world. Additional eclipse observations were also obtained with HST-NICMOS (Swain et al. 2008c), Spitzer-IRS (Grillmair et al. 2008; Todorov et al. 2014), and other instruments (Swain et al. 2010). For the Spitzer-IRS data set, the reanalysis presented in Grillmair et al. (2008) led to differences in the recovered spectrum. Overall, the observed fluxes were consistent in terms of shape but the flux ratios appeared to be 20% lower in the later study. Sources of these discrepancies could come from the additional data considered (stellar variability) or differences in the reduction techniques (ramp models). Either way, this example highlights the difficulties of analyzing combined data sets from different sources or taken at different epochs.

As the HST transit data (PN: 12881, PI: McCullough 2012) were previously analyzed with Iraclis in Tsiaras et al. 2018, we take the data directly from this paper. For the eclipse, we perform our standard reduction of the visit and obtain the emission spectrum. We note that our recovered emission spectrum of the G141 grism is consistent with the one from Crouzet et al. (2014). For the Spitzer data, we use the latest reduction from Charbonneau et al. (2008) consisting of the 3.6, 4.5, 5.8, 8, 16, and 24 μm photometric channels.

When performing the retrieval analysis of the emission spectrum, we find that the HST spectrum is almost

uninformative. On the HST spectrum only, the free and equilibrium runs lead to an isothermal temperature structure, and the solutions found do not lead to higher evidence than the simpler blackbody fits. There is some slight indication that CH₄ might be there due to the modulation at 1.4 μm and the increased absorption around 1.6 μm , where CH₄ possesses absorbing properties. When the Spitzer data are included, however, the free retrievals detect H₂O in low abundance, around 10^{-5} along with CO₂. There might also be some hints of FeH; however, the latter molecule is not required as shown by the almost similar Bayesian evidence between the reduced and full runs. The derived metallicity in the full HST+Spitzer run is slightly supersolar, which matches the findings from the equivalent equilibrium run. However, the C/O is found to be 0.5 due to CO₂ being the only species detected in those observations. In the equilibrium case, the thermal profile displays a localized inversion and the C/O is much more constrained to supersolar values.

Our retrieval analysis of the transmission spectrum gives similar results to the one in Tsiaras et al. 2018. The free retrieval indicated that the terminator is cloudy with a large water absorption feature at 1.4 μm , thus matching the findings from the eclipse retrievals that include Spitzer. The rest of the molecules are not detected, but strong upper limits on the optical absorbers and H⁻ can be extracted. The equilibrium retrieval suggests a deeper cloud cover but is consistent with a similar chemistry to solar metallicity and subsolar to solar C/O.

D.8. Individual Analysis of HD 209458b

HD 209458b is one of the historically most-studied exoplanets, together with HD 189733b. In 1999, it was announced as the first transiting exoplanet (Charbonneau et al. 2000; Henry et al. 2000) and shortly thereafter became the prime target of many observing campaigns due to the detection of its atmosphere via the absorption of Na (Charbonneau et al. 2002). Many molecules (H₂O, CO, CH₄, CO₂, and NH₃) have now been detected (Barman 2007; Swain et al. 2008a; Snellen et al. 2010; Deming et al. 2013; Line et al. 2016; MacDonald & Madhusudhan 2017; Tsiaras et al. 2018). In particular, preliminary analyses of the dayside emission obtained with five photometric Spitzer channels indicated the possible presence of thermal inversions (Burrows et al. 2007; Knutson et al. 2008; Crossfield et al. 2012b). However, later analyses of HST G141 observations and resanalyses of the Spitzer data (Diamond-Lowe et al. 2014; Line et al. 2016) were more consistent with the presence of water vapor, seen in absorption at 1.4 μm and no thermal inversions. We reanalyzed the G141 data set (PN: 13467, PI: Bean 2013) using Iraclis and were able to recover an eclipse spectrum for all five visits. We note that Line et al. (2016) also attempted to reduce the five observed eclipses but did not manage to recover a spectrum from the fourth visit. We note that Line et al. (2016) fitted all the visits together and did not rely on a normalization of the white light-curve depths. Our pipeline does not offer this option at the moment, but future works could investigate if the observed differences are due to this point. For the Spitzer data sets, HD 209458b was not included as part of the population study from G20, so we used the six broadband points from 3.6 μm to 25 μm used in Diamond-Lowe et al. (2014), including the data sets reduced in Crossfield et al. (2012b) and Swain et al. (2008a).

For the terminator, the HST G141 transit observation (PN: 12181, PI: Deming 2010) was previously reduced with Iraclis in Tsiaras et al. 2018, so we take the transmission spectrum from this study.

We present the results of our retrievals on the eclipse spectrum of HD 209458b in Figure Set D1 but also illustrate our methodology in the Appendices B and C. We can immediately notice that our spectrum, as compared to the one obtained in Line et al. (2016) possesses a similar shape of the water feature between 1.2 and 1.3 μm , but with an apparent vertical offset. In all our free runs, except the full run with HST only, we however recover a similar solution that contains water vapor in subsolar abundances. Due to the particularly high S/N for this spectrum, the recovered abundances are very tightly constrained. When Spitzer is included, CH₄ and CO are also detected. For the full run with HST only, we find a very different solution that does not involve H₂O or CH₄. Instead, the spectrum that was interpreted with an absorption at 1.4 μm is now interpreted with an emission feature at 1.2 μm . In this case, the temperature profile is inverted, and the feature is fitted with a low amount of FeH and H⁻ opacity. We highlight that this solution is most likely an artifact of the spectrum scatter but the difference in $\log(E)$ between the HST-only runs is surprisingly high in favor of the FeH and H⁻ solution, confirming that the shape of our WFC3 data is better fit with the inverted solution. A similarly inverted temperature solution also develops in the equilibrium chemistry retrieval, further confirming the odd shape of the water feature in our data. In all the retrievals for HD 209458b, except the HST equilibrium chemistry run, we find subsolar-metallicity solutions that are most likely attributed to the low abundance of water we retrieve. We note that the full and equilibrium Spitzer solutions are very close, both in terms of retrieved thermal structure and elemental ratios, with a C/O of about 1.

In transit, we observe water in the atmosphere of HD 209458b, associated with a high-altitude cloud cover. No other molecules are detected. In both the free and equilibrium runs, the atmosphere is consistent with solar metallicity. A low C/O is found in the free run, while the equilibrium chemistry does not seem to provide constraints on this quantity.

D.9. Individual Analysis of KELT-1 b

The first low-mass object discovered by the KELT-North survey, KELT-1 b, is a $27M_J$, $1.12R_J$ planet with a very short-period circular orbit of 29 hr. In 2012, Siverd et al. (2012) presented spectroscopy, photometry, and radial velocity data and obtained an equilibrium temperature of $T_{eq} \approx 2400$ K, due to the significant amount of stellar irradiation received by this planet. Its extreme temperature and significant inflation make KELT-1b a valuable case study for short-period atmospheric characterization. In 2014, Beatty et al. (2014) observed KELT-1 b's secondary eclipse using Spitzer, obtaining eclipse depths that are compatible with the presence of a strong substellar hot spot, suggesting poor or moderate heat redistribution for this atmosphere. Subsequently, their investigations favor an atmosphere without a TiO inversion layer, where a mechanism of "day-to-night TiO cold trap" is proposed. This study was followed up with ground-based spectrophotometry in 2017, with Beatty et al. (2017) presenting an H-band emission spectrum obtained with the LUCI1 multiobject spectrograph on the Large Binocular Telescope. Modeling of the atmospheric emission using the obtained average dayside brightness

temperature of 3250 K suggested a monotonically decreasing temperature–pressure profile. The team highlighted these findings as unusual because many other hot Jupiters of similar temperatures were believed to be in possession of either an isothermal or a thermally inverted temperature structure. The differences were attributed to the higher surface gravity of KELT-1 b, which could contribute to the creation of TiO cold traps.

Using our standardized methodology, we reanalyzed the WFC3 eclipse observations (PN: 14664, PI: Beatty et al. 2016) of KELT-1 b. To our knowledge, this data set has not been analyzed in a publication before. Because the Spitzer observations were not included in the systematic analysis of G20, we chose to include the original data set from Beatty et al. (2014). For the transit, because the raw data (PN: 14664, PI: Beatty et al. 2016) were already analyzed with Iraclis by Tsiaras et al. 2018, we took the spectrum obtained in this study.

For the dayside, the spectra, temperature profiles, and posterior distributions of our standardized retrievals are presented in Figure Set D1. Broadly speaking, in both HST and HST+Spitzer runs, the atmosphere presents indications of a localized thermal inversion associated with VO, FeH, and H⁻. We note that some degeneracies exist with the posteriors presenting bimodal behavior and solutions that include either H⁻, or FeH and VO. By comparing the Bayesian evidence with the reduced runs (with no metal hydrides/oxides), our retrievals demonstrate the need for these optical absorbers, especially when Spitzer is included. In the full scenarios, the atmosphere is most consistent with a subsolar to solar metallicity, but as for many other planets, the recovered C/O is not well constrained and all values are allowed. When assuming equilibrium chemistry, we note that the thermal profiles decrease with altitude, contrasting with our full free runs. With this assumption, the atmosphere prefers a solar metallicity with high C/O if Spitzer is not included, or a supersolar metallicity and solar C/O when Spitzer is also considered. For this planet, chemical equilibrium is not a good assumption as demonstrated by the much lower Bayesian evidence obtained by these fits.

When analyzing the transmission spectrum of KELT-1 b, we do not find evidence for any molecular absorption, noting that clouds are most likely masking the presence of molecules in this atmosphere.

D.10. Individual Analysis of KELT-7 b

As a planet with a high equilibrium temperature and low surface gravity (Bieryla et al. 2015), KELT-7 b is an excellent candidate for atmospheric characterization. The transmission spectrum (PN: 14767, PI: Sing et al. 2016b) of KELT-7 b was analyzed by Pluriel et al. (2020), who found a rich transmission spectrum that is consistent with a cloud-free atmosphere and suggests the presence of H₂O and H⁻. The same study also analyzed the WFC3 emission spectrum (PN: 14767, PI: Sing et al. 2016b), which could be explained by a varying temperature–pressure profile, CIA, and H⁻. Pluriel et al. (2020) explored the effect of including Spitzer data from G20, finding little changes when including these observations in the emission retrievals. As the raw data were reduced using the Iraclis pipeline in Pluriel et al. (2020), we took the data as they are and started our analysis from there.

Our retrieval analysis differs from the one in Pluriel et al. (2020) in a few aspects. First, our free retrieval includes two

more molecules: CH₄ and CO₂. Here, we also considered the appropriate Spitzer instrument response functions, which were considered flat in Pluriel et al. (2020). The star was also modeled using an interpolated Phoenix spectrum at metallicity [Fe/H] = 0.139.

From the free run, we recover the results from Pluriel et al. (2020), who found a thermally inverted temperature profile associated with the emission of H⁻, in both the HST-only and HST+Spitzer cases. In the HST+Spitzer case, we also find hints for additional absorption from TiO. When comparing the ln(*E*) between the reduced and full runs, we find that the addition of optical absorbers is in fact justified only for the HST+Spitzer case. As discussed previously, for an atmosphere with a high level of thermal dissociation, such as KELT-7 b, the derived metallicity is likely biased. From the equilibrium chemistry runs, we find metallicities that are solar to supersolar, but we also note that the recovered thermal structure is very different from the ones found by the free-chemistry runs. In terms of C/O, the equilibrium chemistry retrieval favors high values.

For the transmission retrieval, we recover the same results as Pluriel et al. (2020). The terminator region is best characterized by H₂O and H⁻ absorption. Again, the derived metallicity for the free run is likely to be biased by the dissociation of the tracers used for its computation. The equilibrium chemistry retrieval on the transit spectrum does not seem to well fit the observed data and does not lead to strong constraints.

D.11. Individual Analysis of KELT-9 b

KELT-9 b is the hottest exoplanet known so far. It orbits an A0V/B9V star ($T = 10140$ K) and reaches a dayside temperature of about ~ 5000 K, being itself hotter than many stars (Gaudi et al. 2017). Given the extreme temperatures, the majority of molecules were anticipated to be dissociated, which would leave only atomic species on the dayside and a featureless broadband spectrum (Kitzmann et al. 2018). Ground-based high-resolution observations have detected a number of metals including iron, titanium, and calcium (Hoeijmakers et al. 2018; Cauley et al. 2019; Hoeijmakers et al. 2019; Yan et al. 2019; Pino et al. 2020; Turner et al. 2020), which are consistent with this picture. Observations of the KELT-9 b phase curve with TESS and Spitzer have revealed an asymmetric transit (Ahlers et al. 2020) induced by the fast rotation of its host star. The rotation leads to a non-uniform structure in the star, which has a larger and brighter equator than the poles, whereas KELT-9 b orbits with an 87° spin-orbit angle. The same studies indicate that the planet possesses a low day–night temperature contrast with indications for H₂ dissociation and recombination (Wong et al. 2020a; Mansfield et al. 2020b). As KELT-9 b is subject to intense irradiation from the star and has a large extended hydrogen envelope reaching the Roche lobe limit, it is experiencing extreme atmospheric escape (Yan et al. 2019). As of today, there are no transmission data for this planet. The HST eclipse observation (PN: 15820, PI: Pino et al. 2019) was previously analyzed by the same authors in Changeat & Edwards (2021) and using the same methodology, so we do not reproduce the reduction of the spectrum from this planet. We note that the physical characteristics of this system leads to a particularly precise spectrum in a single observation.

The only difference with the analysis in Changeat & Edwards (2021) is the addition of CO₂, which is required for

comparing with the rest of our population. This does not change the results, and we recover a strongly inverted temperature profile, with the presence of molecules on the dayside. This was noted in Changeat & Edwards (2021) as a rather surprising finding because the associated temperatures are high enough to dissociate them in a solar composition and equilibrium chemistry. This therefore suggested the presence of disequilibrium processes, nonsolar chemistry, or biases from other sources. When analyzing the equilibrium scenarios, we note that, similarly to the reduced cases, they do not perform well and lead to much worse fits of the observed data (see the Bayesian evidence). For this planet, the estimates of the metallicity and the C/O from our free chemistry are highly inaccurate due to the expected dissociation of the main molecules and our lack of constraints on the elements in atomic/ionic forms. Because the planet is likely experiencing disequilibrium chemistry, the equilibrium runs, which return a slightly subsolar metallicity and a C/O of about 1, are also most likely biased and should be considered with caution.

D.12. Individual Analysis of Kepler-13A b

The exoplanet Kepler-13A b (Shporer et al. 2011) orbits a rapidly rotating A-type star in a triple-star system. The planet's dayside was studied in great detail in two previous studies (Shporer et al. 2014; Beatty et al. 2017), which indicated a very high temperature but did not find thermal inversions. Due to the presence of the two stars Kepler-13 A and Kepler-13 BC, the extraction process for this planet involves many steps that are not automated in our pipeline Iraclis. We therefore choose not to reanalyze the HST emission spectrum obtained in Beatty et al. (2017), who carefully removed the contribution from the two stars to extract the spectrum. The data were taken as part of the proposal PN:13308 led by Ming Zhao (Zhao 2013). We also added the Spitzer photometric points from Shporer et al. (2014) as is and started our analysis from these spectra. We note that this atmosphere was not studied in transit spectroscopy with HST.

The spectra, temperature profiles, and posteriors from our atmospheric retrievals can be found in Figure Set D1. As in the previous studies in the literature, we recover a decreasing temperature gradient with altitude and a well-constrained abundance of water vapor in all scenarios. This is driven by the strong and well-defined $1.4 \mu\text{m}$ water feature in the HST spectrum. Given the temperature of this atmosphere, one might expect the presence of metal oxide and hydrides, but none were detected in our analysis. The addition of the Spitzer data does not impact the results of our retrievals, except by providing further limits on the CO_2 abundance. For the free and equilibrium runs, the metallicity is similar and consistent with solar values. The C/O in the free runs is difficult to constrain due to the nondetection of carbon-bearing species. When considering the equilibrium chemistry retrievals, the C/O is found to be roughly solar with large uncertainties.

D.13. Individual Analysis of TrES-3 b

TrES-3 b is a hot Jupiter of about $2 M_J$ (O'Donovan et al. 2007). At the time of its discovery in 2007, it had one of the shortest orbital periods of the known planets and was deemed a good candidate for atmospheric follow-up observations. The planet was then studied using photometric measurements, leading to some of the first exoplanet detections of emission via

secondary eclipse (de Mooij & Snellen 2009; Croll et al. 2010). An eclipse spectrum was then captured by the HST-WFC3 camera and studied as part of a population analysis of five planets (Ranjan et al. 2014). According to their findings, the TrES-3 b spectrum is consistent with a simple blackbody emission, but the authors point out that combining these observations with the Spitzer data from Fressin et al. (2010) is inconsistent with the blackbody fit. In their study, they find that an atmosphere with a solar to low metallicity best represents the combined data set. Similar results are also found in Line et al. (2014), who are also able to rule out a high-C/O solution, thanks to a statistical retrieval analysis.

We reduced the eclipse observation from the raw HST images (PN: 12181, PI: Deming 2010) using our Iraclis reduction pipeline. The eclipse spectrum we obtain differs strongly from the one in Ranjan et al. (2014), here displaying an emission feature at $1.4 \mu\text{m}$. In their study, we note, however, that the fit of their white light curve does not present data points covering the baseline or the ingress/egress of the transit. For our analysis, we add the Spitzer photometric observations recovered in Fressin et al. (2010) and perform our standardized retrieval runs.

Due to the higher emission obtained at $1.4 \mu\text{m}$ in our observed spectrum, the run that does not include the Spitzer data is well fit with the emission of water. The recovered thermal profile is therefore inverted and no other molecules are necessary to explain this data set. When the Spitzer data is added, however, the water is rejected due to the low emission in the Spitzer bandpass. The spectrum is best fit with small amounts of FeH and VO. The thermal profile in this case is more complex, with a temperature decrease with altitude deep in the atmosphere and a thermal inversion at lower pressures. The metallicity and C/O derived from the free retrieval with Spitzer are not well constrained as water and carbon-bearing species are not recovered. In the equilibrium chemistry runs, the solutions also differ depending on whether Spitzer is included or not. In the HST-only case, the thermal profile is inverted to best fit the $1.4 \mu\text{m}$ feature and associated with solar metallicity and C/O, most similar to the results of the corresponding free chemistry. When Spitzer is included, the profile is reversed and the spectrum is best fit with a flat spectrum in the WFC3 wavelength range, associated with a supersolar metallicity and a high C/O.

D.14. Individual Analysis of WASP-4 b

WASP-4 b is an inflated hot Jupiter (Wilson et al. 2008) with an equilibrium temperature of around 1800 K. The planet dayside was observed with HST during a single visit, taken in staring mode (PN: 12181, PI: Deming 2010). The data, while having a low S/N, favored an atmosphere with an isothermal or a weakly inverted thermal profile and poor water content (Ranjan et al. 2014). Those results confirmed previous findings using Spitzer (Beer et al. 2010). In this study, we reanalyzed the HST data using our Iraclis pipeline. As the Spitzer data were not part of the G20 study, we used the data from Beer et al. (2010). We note that an additional staring mode transit spectrum was taken as part of the same HST proposal, but an adequate fit to the data could not be obtained.

In our TauREx3 retrievals, we show that the HST spectrum does not contain a lot of information. Indeed, the pure blackbody fits perform similarly to the full and reduced runs in the HST-only scenarios. When optical absorbers are

considered, the retrievals indicate the possible presence of TiO, but large tails can be observed. The detection is not significant because the Bayesian evidence of the reduced runs is similar to the full cases. The thermal profile for this planet, found in our free runs, is either isothermal or locally inverted. When running the equilibrium chemistry retrievals, it is again difficult to conclude, with the HST-only case favoring a weak thermal inversion and the HST+Spitzer case favoring a decrease of temperature with altitude. In those two cases, the metallicity is solar with large uncertainties, while the C/O is supersolar.

D.15. Individual Analysis of WASP-12 b

WASP-12 b has previously been studied with transmission and emission spectroscopy using WFC3 G141 in staring mode (Swain et al. 2013). The study found an emission spectrum consistent with a blackbody and only marginal evidence for molecular features in the transmission data set. Phase-curve observations with the Spitzer Space Telescope at $3.6\ \mu\text{m}$ and $4.5\ \mu\text{m}$ indicated large emission amplitudes, showing evidence for poor day-to-night heat transport (Cowan et al. 2012). Photometric eclipse observations with Spitzer over $3.6\text{--}8\ \mu\text{m}$ (Campo et al. 2011) suggested a weak thermal inversion (Madhusudhan et al. 2011) and a supersolar C/O. These studies, however, did not account for the presence of a binary companion system (Bergfors et al. 2012; Bechter et al. 2014). When reanalyzed to correct for this, the previous observations of WASP-12 b were inconsistent with an isothermal atmosphere due to eclipse depth variations in the Spitzer bandpass (Crossfield et al. 2012a; Stevenson et al. 2014) and required the presence of a carbon-rich atmosphere (HCN and C_2H_2) on the dayside. On the terminator, analysis detected the possible presence of H_2O or CH_4/HCN and metal-bearing molecules (Stevenson et al. 2014). Later studies confirmed the possibility of supersolar C/O, detecting H_2O in the terminator (Kreidberg et al. 2015) thanks to the addition of the G102 grism, but highlighted the impact of priors and model choices (Kreidberg et al. 2015; Oreshenko et al. 2017) in analyzing this particularly difficult data set.

STIS transit observations were also taken and, when combined with the WFC3 data, showed no evidence for TiO (Sing et al. 2013). However, as the WFC3 observations were in staring mode, the error bars on the data were large ($\sim 120\text{--}200$ ppm). The G141 transmission spectrum was subsequently obtained in scanning mode and, when combined with transit observations from the G102 grism, displayed a broad water feature ($\log(\text{H}_2\text{O}) = -2.7^{+1.0}_{-1.1}$; Kreidberg et al. 2015). The spectrum showed no signs of optical absorbers with a 3σ upper limit of $\log(\text{TiO}) = -3.69$.

As for the other planets, we reduced the HST G141 eclipse observation (PN: 12230, PI: Swain 2010) using our Iraclis pipeline. We applied the dilution factor to correct for the unresolved companion of this system (Bergfors et al. 2012; Bechter et al. 2014). For the Spitzer data, we obtained the corrected reductions from Stevenson et al. (2014), which we included as is. The transmission spectrum (PN: 13467, PI: Bean 2013) with HST was already analyzed in Tsiaras et al. 2018, so we took the spectrum from this study.

The emission of WASP-12 b at HST wavelengths is most consistent with a blackbody spectrum. This is shown by the similar Bayesian evidence obtained in our reduced and full retrievals as compared with the simpler blackbody fit. When Spitzer is considered, the full retrieval recovers CO_2 and

possibly FeH, with a localized thermal inversion. The FeH detection is however not robust as shown by the similar Bayesian evidence obtained in the reduced run that includes the Spitzer points. In the reduced run, CO_2 is still detected, which confirms the need for this molecule to explain the observed combined spectrum. The derived metallicity for the full run is about solar with a C/O of 0.5, most likely biased by the CO_2 detection. In the equilibrium chemistry runs, the HST-only case is consistent with the results from the free-chemistry retrievals. When Spitzer is added, the C/O is found to be closer to 1 with a decreasing-with-altitude thermal profile. We note that the free-chemistry runs do not provide a significantly better fit than the chemical equilibrium.

At the terminator, the transit of WASP-12 b is clearly indicative of high-altitude clouds and the presence of water vapor, which was not detected on the dayside. Our results are similar to that of Tsiaras et al. 2018, and we derive an atmosphere with solar metallicity but large uncertainties on the C/O. The free retrievals do not require the presence of carbon-bearing species.

D.16. Individual Analysis of WASP-18 b

WASP-18 b (Hellier et al. 2009) has been thoroughly studied because its discovery in 2008. Spitzer, HST-WFC3, and ground-based eclipses have been taken (Nymeyer et al. 2011; Iro & Maxted 2013; Sheppard et al. 2017; Arcangeli et al. 2018; Kedziora-Chudczer et al. 2019; Manjavacas et al. 2019; Gandhi et al. 2020) as well as phase curves with HST-WFC3 and TESS (Arcangeli et al. 2019; Shporer et al. 2019). These have revealed a low albedo, poor redistribution of energy to the nightside, and evidence for an inverted dayside temperature–pressure profile. In particular, the analysis from Sheppard et al. (2017) considered a data set similar to us and detected a strong thermal inversion, associated with the presence of H_2O and CO.

The HST transmission spectrum was taken, along with two eclipses, as part of a phase curve (PN: 13467, PI: Bean 2013). As part of the same proposal, three additional eclipses were also obtained. For consistency, we reanalyzed the raw data using the Iraclis pipeline and our standardized methodology. We also added the Spitzer observations from Nymeyer et al. (2011) for the four photometric channels from 3.6 to $8\ \mu\text{m}$. The transmission spectrum (PN: 13467, PI: Bean 2013) was included in the Tsiaras et al. 2018 study, which also employed the Iraclis reduction pipeline, so we conserved their spectrum.

In eclipse, we find that the atmosphere of WASP-18 b is well fit by a localized thermal inversion, with emission from H_2O and e^- . For this planet, the results are consistent between the HST and HST+Spitzer runs. As opposed to the study from Sheppard et al. (2017), we do not find evidence for CO, differences that might be due to their model not including H^- opacities or differences in our reduction techniques. We find that the atmosphere has a solar to slightly supersolar metallicity, which is also confirmed by the equilibrium chemistry retrievals. For the C/O, this parameter is not constrained by our free runs due to the lack of detection of carbon-bearing species, but when assuming equilibrium chemistry, we find this atmosphere consistent with a C/O of about 1.

For the transit, our retrieval analysis reveals that a very flat spectrum provides a good fit to the data. This is most likely due to the presence of high-altitude clouds, opaque at those

wavelengths. As noted in Tsiaras et al. 2018, we are not able to extract further constraints on the possible abundances of any molecular species.

D.17. Individual Analysis of WASP-19 b

WASP-19 b has been the subject of a number of investigations, from both the ground and from space. Work by Anderson et al. (2013) analyzed four Spitzer eclipses, taken across 3.6–8 μm , and constructed a spectral energy distribution of the planet’s dayside atmosphere. They found no stratosphere, supporting the hypothesis that hot Jupiters orbiting active stars have suppressed thermal inversions (Knutson et al. 2010). Analysis of the TESS optical phase curve showed moderately efficient day–night heat transport, with a dayside temperature of 2240 K and a day-to-night contrast of around 1000 K (Wong et al. 2020b). This study also utilized a host of ground-based observations by Anderson et al. (2010), Burton et al. (2012), Abe et al. (2013), and Bean et al. (2013). However, they did not utilize the HST-WFC3 G141 observations of the WASP-19 b eclipse. WASP-19 b has also been studied via transmission spectroscopy. The retrievals of the STIS-G430L, G750L, WFC-G141, and Spitzer-IRAC observations suggest the presence of water at $\log(\text{H}_2\text{O}) \approx 4$ but show no evidence for optical absorbers (Sing et al. 2016a; Barstow et al. 2017; Pinhas et al. 2019). Those results do not match the ground-based transits that were acquired with the European Southern Observatory’s Very Large Telescope (VLT), using the low-resolution FORS2 spectrograph, which covers the entire visible-wavelength domain (0.43–1.04 μm). When analyzing this data, Sedaghati et al. (2017) detected the presence of TiO to a confidence level of 7.7σ .

In this study, we reduced the WFC3 data of the WASP-19 b eclipse (PN: 13431, PI: Huitson 2013) using Iraclis and obtained the eclipse spectrum. The Spitzer data are available in G20 for the 3.6 and the 4.5 μm channels, but because Anderson et al. (2013) also reduced the additional 5.3 and 8 μm channels, we choose to use the later Spitzer data in our retrieval analysis. As the transit observations of WASP-19 b were not included in the Tsiaras et al. 2018 population study with Iraclis, we also reduce this data set (PN: 12181 and 13431, PI: Deming 2010; Huitson 2013) before running our standardized retrieval analysis.

At the dayside, we find decreasing temperature profiles for all scenarios, with the data being well fit by the absorption of water. In all our models, we do not find evidence for optical absorbers. This is confirmed by the $\ln(E)$, which is essentially the same in both reduced and full runs. The free-chemistry runs are consistent with the equilibrium chemistry scenario, and we find a solar to supersolar metallicity best fits this observed spectrum. The C/O is, as expected, poorly constrained, but full runs seem to favor a low C/O, which is also confirmed by the HST+Spitzer equilibrium chemistry run.

At the terminator, the transmission spectrum is well fit by water vapor. In the free run, this is the only molecule that is clearly identified. Clouds could also be present with a wide range of possible altitudes, as shown by the posterior distribution. The metallicity inferred in both free and equilibrium runs is solar. For the C/O, the free run prefers a subsolar case due to the lack of detection of carbon-bearing species, while the equilibrium run does not provide strong constraints, again demonstrating the difficulty of constraining these parameters from HST only.

D.18. Individual Analysis of WASP-33 b

WASP-33 b is the first planet discovered to orbit a δ Scuti variable star (Cameron et al. 2010; Herrero et al. 2011). At the time of discovery, it was the hottest known exoplanet, with temperatures above 3000 K. It now belongs to the category of the extremely hot Jupiters, with KELT-9 b and WASP-189 b. As such its hot dayside is believed to be deprived of water vapor and contain metal oxide and hydrides. Due to the complex pulsations of the star, the analysis of WASP-33 b involves complex deconvolution of the stellar signal. Early studies of its atmosphere indicated the likely presence of a thermal inversion associated with TiO emission (Deming et al. 2012; von Essen et al. 2014; Haynes et al. 2015), which greatly contributed to the debate on the importance of TiO and VO in hot Jupiters (Fortney et al. 2008; Gandhi & Madhusudhan 2019). Later follow-ups at high resolution from the ground confirmed the detection of TiO (Nugroho et al. 2017), while observations of the terminator during transit were also consistent with the presence of optical absorbers, this time AIO (von Essen et al. 2019). While the picture appeared clear, recent studies and reanalysis of WASP-33 b’s atmosphere, however, shed some doubts on the robustness of the TiO and VO detections (Herman et al. 2020; Serindag et al. 2021). In this work, we consider the HST-WFC3 data obtained during the eclipse of WASP-33 b (PN: 12495, PI: Deming 2011). While the spectrum was extracted in Haynes et al. (2015) with another pipeline, we do not perform an Iraclis reduction from the raw data due to the complexity of accounting for the stellar pulsations. Instead, we take the reduced spectra as is from Haynes et al. (2015) and start our retrieval analysis there. For this planet, there are no WFC3 transit observations.

The results of our retrieval analysis are shown in Figure Set D1. From comparing the Bayesian evidence of the free models, it is evident that this reduced spectrum requires a model including optical absorbers. In the full models, the solutions are the same, independently of whether Spitzer is considered or not. The models converge to a strong thermal inversion associated with emission features of water vapor, TiO, and H^- . In Haynes et al. (2015), their investigations also highlighted the evidence for TiO absorption in the same data sets, but in their models, they did not fit for this molecule and choose to fix its abundance to solar values. Here we find compatible results but also highlight the likely presence of H^- , an opacity that was not considered in the original study. Our solutions possess a subsolar metallicity and unconstrained C/O, but we highlight that our method to determine elemental abundances is likely inaccurate for this type of atmosphere as many of the considered tracers dissociate into atomic/ionic species, similarly to KELT-9 b. In the equilibrium chemistry run, the atmosphere is found slightly subsolar but with a well-constrained C/O of about 1.

D.19. Individual Analysis of WASP-43 b

WASP-43 b is one of the first (Hellier et al. 2011) and most-studied hot Jupiters. With a dayside temperature of about 1800 K, this 1 R_J planet of about 2 M_J has been at the center of many studies, thanks to the large number of observations in transit, eclipse, and phase curves. In particular, it is one of the rare planets that has been observed in phase curve with HST (Stevenson et al. 2014). This study demonstrated the use of HST in phase-curve studies for the first time and detected the

presence of water vapor. A follow-up study included the Spitzer phase curve in the analysis (Stevenson et al. 2017), extending the constraints to carbon-bearing species. Those studies also highlighted an offset in the hot spot of the planet as well as a large day–night contrast. The nightside was found to be surprisingly cool, which suggested that global opaque clouds might cover the deeper layers of this side of the planet. We note, however, that the use of a more complex method to analyze the same data (Feng et al. 2016), highlighted that the previous constraints on CH₄ might be biased due to the 1D assumption in the earlier studies. Using the data from the same phase curve, water vapor was also detected in the terminator region (Kreidberg et al. 2014b) but a later, more complete study (Chubb et al. 2020a) also indicated that an optical absorber, AIO, might be present in this region.

For those reasons, WASP-43 b became the go-to planet for theoretical work on global circulation (Mendonça et al. 2018b; Carone et al. 2020; Venot et al. 2020) in exoplanet atmospheres and for cloud/haze modeling (Helling et al. 2020, 2021). Similarly, due to the availability of consistent HST and Spitzer phase curves, the planet is often used as a benchmark for the development of retrieval techniques exploiting the 3D aspects of atmospheres (Changeat & Al-Rafaie 2020; Feng et al. 2020; Irwin et al. 2020; Taylor et al. 2020; Changeat et al. 2021). However, later contradictory reanalyses of the Spitzer phase curve demonstrated the difficulties in recovering robust estimates of atmospheric emission with Spitzer (Mendonça et al. 2018a; Morello et al. 2019; May & Stevenson 2020; Bell et al. 2021). This further demonstrates the need for cautious approaches when combining the HST and Spitzer data sets. As for the thermal profile, it was believed to be decreasing with altitude up until Changeat et al. (2021), which displayed model-dependent behavior and concluded that thermal inversions could not be rejected for this planet.

In this paper, we reanalyze from scratch the eclipse observations (PN: 13467, PI: Bean 2013) of WASP-43 b. For the 3.6 and 4.5 μm Spitzer channels, we use the values from G20. For the transmission, the data (PN: 13467, PI: Bean 2013) were first studied in Kreidberg et al. (2014b), but it was since reanalyzed in Tsiaras et al. 2018, which used the Iraclis pipeline. We therefore proceed from the retrieval step directly, taking the spectrum from Tsiaras et al. 2018.

Analyzing the eclipse spectrum, we find that the HST +Spitzer retrieval contains a decreasing-with-altitude thermal profile. The 1.4 μm feature is, in this case, associated with the presence of water vapor, as found in previous studies. The models also require the presence of CO₂, which absorbs in the 4.5 μm Spitzer band. Now, considering HST only, the full run, including optical absorbers, converges to a different solution. This second solution displays a thermal inversion and low abundance of FeH, seen in emission. While this is most likely due to the data point being scattered between 1.2 and 1.3 μm , this result highlights why the interpretation of eclipse spectra with HST alone is difficult. This re-enforces the discussion regarding model degeneracies made in Appendix C, which explains why a spectral feature at 1.4 μm can be well interpreted by either absorption of H₂O or emission of refractory species. For this planet, comparisons of the Bayesian evidence in the HST-only case indicate that the simpler reduced model, with the absorption of H₂O, in fact, provides an equivalent fit to the data. Regarding the derived metallicity and C/O, the retrieval of the HST+Spitzer data are consistent with

a supersolar metallicity and a C/O of about solar. The C/O value is most likely due to CO₂ being the only detected species, but the metallicity is also confirmed by the HST+Spitzer equilibrium chemistry retrieval. The HST-only run is best represented by an isothermal thermal profile with large uncertainties on the metallicity and C/O.

When considering the transit data, we find some evidence for water vapor but the features appear relatively muted, most likely due to opaque clouds. As highlighted in previous studies (Kreidberg et al. 2014b; Stevenson et al. 2017), the temperature found at the terminator is much lower than the one from the dayside. Our findings from the free chemistry are consistent with a solar to supersolar metallicity but an unconstrained C/O, which matches the results found by our equilibrium chemistry model.

D.20. Individual Analysis of WASP-74 b

Orbiting a slightly evolved F9 star, WASP-74 b is a 0.95 M_J moderately inflated hot Jupiter (Hellier et al. 2015). While we did not find any analysis of the eclipse of this planet, the HST transmission spectrum was first analyzed in Tsiaras et al. 2018, uncovering a moderate water feature. Later, ground-based photometry with multiple filters was obtained and, when combined with the HST spectrum, favored models containing TiO and VO absorption (Mancini et al. 2019). This was however argued against in a follow-up study using the same data as well as further photometric observations from the ground and Spitzer-IRAC 1/2. In this later study, no evidence for these optical absorbers was found, and the data favored a strong Rayleigh slope (Luque et al. 2020).

We take the transmission spectrum from Tsiaras et al. 2018 (PN: 14767, PI: Sing et al. 2016b) and reduce the single G141 observation of the eclipse (PN: 14767, PI: Sing et al. 2016b) using our Iraclis pipeline. For the Spitzer observations, we use the photometric emission recovered as part of the G20 population study.

Analyzing the eclipse spectrum, we do not find evidence for optical absorbers. The free retrieval including HST and Spitzer observations reveals the presence of H₂O and CH₄ as the main absorbers with a decreasing thermal profile with altitude. It is interesting to note that the HST-only case leads to a slightly inverted thermal profile with H⁻ opacity, however, the Bayesian evidence of this retrieval as compared to the reduced case does not change, indicating that the increase in complexity is not justified. Looking at the metallicity and C/O, we find a solar metallicity and an unconstrained C/O. The metallicity recovered from the equilibrium chemistry runs is also solar, and the models are overall consistent with the findings from free chemistry. When equilibrium chemistry is assumed, the thermal profile is also decreasing with altitude. When only HST is considered in the equilibrium retrievals, the C/O remains unconstrained, but adding Spitzer restricts the solutions to high values.

At the terminator, we find some evidence for H₂O and FeH, but with large tails in the posterior distributions. In both free and equilibrium models, high-altitude clouds are likely to explain the flat shape of the transmission spectrum. The metallicity is found to be around solar values with large uncertainties, while the C/O is unconstrained.

D.21. Individual Analysis of WASP-76 b

WASP-76 b was first studied by HST-WFC3 in transmission. These observations were analyzed as part of the Tsiaras et al. 2018 population study (Tsiaras et al. 2018), where their retrievals suggested a water-rich atmosphere ($\log(\text{H}_2\text{O}) = -2.7 \pm 1.07$) with a 4.4σ detection of both TiO and VO. However, as noted in the study, the abundance of TiO retrieved is likely to be nonphysical and driven by narrow spectral coverage. Retrieval analysis of this spectrum was also performed by Fisher & Heng (2018) who extracted a water abundance that was incompatible with the previous study ($\log(\text{H}_2\text{O}) = -5.3 \pm 0.61$). Fisher & Heng (2018) did not include TiO and VO in their analysis but instead used a nongray cloud model to match the opacity at shorter wavelengths. In a more recent study, Edwards et al. (2020), we accounted for a faint stellar companion to WASP-76 b (Bohn et al. 2020; Southworth et al. 2020) and showed that the original transit spectrum was contaminated. A similar study was performed by Fu et al. (2021). Once the contamination was removed, the transmission spectrum no longer showed substantial evidence for optical absorbers but retained its strong water feature. WASP-76 b has also been observed in emission with WFC3 G141 and our analysis of the corrected spectrum in the same study shows strong evidence for VO. However, the best-fit abundance of $\log(\text{VO}) \approx -4$ is likely unfeasible, especially as the evidence for TiO in the current data set was marginal. In this initial study, only the WFC3 data were utilized. Here, we do not reanalyze the WFC3 data (Transit PN: 14260; Eclipse PN: 14767, PI: Sing et al. 2016b) and take it directly from Edwards et al. (2020), but we also include the Spitzer points from G20. The only differences from the retrievals performed in Edwards et al. (2020) are that we model the star using a Phoenix spectrum, account for the proper instrument profiles for Spitzer, and include CO_2 for the consistency in our approach.

The analysis of the eclipse spectrum is consistent with a thermal inversion for all models. When optical absorbers are not included, the data are well fit with CH_4 only. When optical absorbers are included, the results are similar to Edwards et al. (2020), and we confirm that H_2O and TiO provide the best fit to the HST data, with decisive evidence in favor of the more complex model. When HST+Spitzer are included, however, a higher $\ln(E)$ is obtained for the reduced case. This solution, while simpler, can arguably be ruled out due to the high abundance of CH_4 that would be required in this case. The free retrievals obtain solar metallicity and subsolar C/O. When running our equilibrium chemistry retrievals, we also find an inverted thermal profile and the chemistry displays a solar to supersolar metallicity as well as a high C/O.

Our interpretation of the transit spectrum of WASP-76 b is the same as in Edwards et al. (2020). The terminator region is most consistent with the presence of water vapor and high-altitude clouds. In the free run, this leads to solar metallicity and low C/O but one can see in the equilibrium chemistry run that solutions with higher metallicities and a wide range of C/O are also consistent with the observed spectrum.

D.22. Individual Analysis of WASP-77 A b

WASP-77 A b is an inflated hot Jupiter in a wide binary system that was first discovered in 2012 (Maxted et al. 2013). The planet orbits WASP-77 A, a G8 V star. WASP-77 B, a

fainter (2 mag) K-dwarf companion, is separated by $3''$. As such, the spatial scans from WASP-77 A and WASP-77 B overlap somewhat on the detector, as shown in Figure D3, and cannot be separated. If not corrected for, the flux from WASP-77 B would evidently adversely affect the recovered emission spectrum for the planet. Hence, to overcome this, we utilized the specialized WFC3 simulator Wayne (Varley et al. 2017) to model the contribution of the secondary star.

We started by analyzing the data (PN: 16168, PI: Mansfield et al. 2020a) in the normal way, extracting the contaminated eclipse spectrum of WASP-77 A b from both visits. We then preceded to account for the contamination. In each of the two eclipses of WASP-77 A b, the relative positions of WASP-77 A and WASP-77 B were different. Therefore, we calculated the positions of WASP-77A and B for each visit from the direct image. We then extracted the high-resolution (10 \AA bins) spectra of WASP-77A and B individually from the first nondestructive read of the out-of-eclipse observations during the second eclipse observation sequence as the star separation was better than the first. Using these spectra, we simulated high-resolution spatially scanned WFC3 images for each star individually. Next, utilizing the same setup used for the analysis of the real data, we extracted the stellar spectra of each star for each visit. For each bin of the eclipse spectrum, we then calculated the flux ratio between the two stars, using this to apply a correction to the eclipse spectrum of WASP-77 A b for each visit. Finally, we calculated the weighted average of the planetary emission.

As for the other planets, we included the Spitzer data. We obtained the photometric measurements in Maxted et al. (2013) and interpreted the spectrum using our standardized atmospheric retrievals. We note that Line et al. (2021) analyzed observations of the same planet at high resolution and detected H_2O and CO. In their study, they concluded from constraints on the abundance of those two molecules that the planet should have a subsolar metallicity and a solar C/O. To our knowledge, the HST observations of WASP-77 A b have not been presented in previous works. We obtained the Spitzer data from the population study of Garhart et al. (2020).

Our atmospheric retrievals are consistent with the presence of water vapor and a decreasing-with-altitude thermal profile in both HST and HST+Spitzer runs. In the HST data, we note that additional modulations of the spectrum at $1.25 \mu\text{m}$ could be associated with the molecule TiO. The detection is significant with an $\ln(E) > 5$ between the full and reduced models. When Spitzer is included, there is additional evidence for carbon-bearing species with the absorption of CH_4 and CO_2 being detected. In the full HST+Spitzer run, we recover a solar metallicity and an unconstrained C/O. Chemical equilibrium runs are consistent with a subsolar metallicity as in Line et al. (2021) but when Spitzer data are added, the C/O is about 0.8. When assuming chemical equilibrium, we note that the $1.25 \mu\text{m}$ spectral modulation that was attributed to TiO in the free runs is not well fit.

D.23. Individual Analysis of WASP-79 b

WASP-79 b (Smalley et al. 2012) is a very large hot Jupiter, believed to have an evaporating atmosphere (Bourrier et al. 2015). It has been shown to have a polar orbit through the Rossiter–McLaughlin effect (Addison et al. 2013).

The transmission spectrum of WASP-79 b (PN: 14767, PI: Sing et al. 2016b) has been previously analyzed with Iraclis as

part of Skaf et al. (2020). A water-rich atmosphere was found, with a $>5\sigma$ confidence level in models with H₂O and FeH included. The latter was included as the optical absorber of choice after initial models without it struggled with nonphysical values.

Sotzen et al. (2020) also analyzed the HST-WFC3, combining it with observations from Magellan/LDSS-3C R, TESS, and Spitzer, resulting in a transmission spectrum range of 0.6–5 μm . While the spectra extracted from the LDSS-3C R data indicated clouds initially, their retrieval code ATMO found that including FeH and H⁻ as absorbers provided better data fits. Rathcke et al. (2021) studied the most complete transmission range. This study included the STIS instrument on HST, with two transits observed through the G430L grating and another through the G750L grating, the HST-WFC3 instrument, the Spitzer 3.6 and 4.5 μm channels, and LDSS-3C R data. The study used three different retrieval tools: NEMESIS, POSEIDON, and ATMO’s retrieval tool, ARC. Similar to the results found by the other two studies, their best-fitting model spectrum is characterized by an absorption feature at 1.4 μm of H₂O, as well as the relatively smooth continuum from 0.4 to 1.3 μm indicative of H⁻ bound-free absorption.

Our analysis of the transmission data (PN: 16168, PI: Sing et al. 2016b) from HST-WFC3 is shown in Figure Set D2. While the water feature is relatively well constrained in the posterior, as with the other studies mentioned, there is little evidence to support the presence of any carbon-based species. The transmission spectrum also shows detection of H⁻ opacity, which was not included in Skaf et al. (2020). In their study, they did not include H⁻, which explains the differences found here. However, their Bayesian evidence (191.2 for their best model with FeH) is very similar to ours, indicating that from an observational point of view, it is difficult to conclude whether FeH or H⁻ (or both) is responsible for the absorption. We note that the equilibrium retrieval does not provide a good fit for the transmission spectrum.

The emission data (PN: 14767, PI: Sing et al. 2016b) were reduced with Iraclis in M. F. Bieger et al. (2022, in preparation), and are shown in Figure Set D1 along with the fits from our standardized retrievals. The emission analysis from our retrievals supports what is found in the transmission—again, the most unconstrained parameters are carbon-based species. Inspection of the full retrieval indicates the detection of VO and FeH, associated with an increasing-with-altitude thermal profile. In the full model, the spectral modulation in the HST spectrum is fit with an emission feature from optical absorbers. On the other hand, if optical absorbers are not included, or if additional constraints from chemical equilibrium are considered, the HST spectrum is better fit with a decreasing temperature profile and the absorption of water vapor. This behavior is independent of whether Spitzer is considered or not and is due to the degeneracies induced by the narrow spectral region of HST, as discussed in Appendix C. The full retrievals, however, provide strong evidence in favor of optical absorbers as the difference in Bayesian evidence is larger than 3 ($\Delta\ln(E) = 4.5$).

These results will require further retrievals and analysis in order to understand the role of TiO, VO, FeH, or H⁻ in the atmosphere of WASP-79 b. The JWST Early Release Science (ERS) program includes WASP-79b as a primary target; JWST will be observing it for 42 hr over four different modes, which will present more opportunities to study this planet in depth

with more precise data. A more detailed analysis of WASP-79 b will be presented in M. F. Bieger et al. 2022 (in preparation).

D.24. Individual Analysis of WASP-103 b

WASP-103 b is an ultra-short-period planet ($P = 22.2$ hr) whose orbital distance is less than 20% larger than its Roche radius, resulting in the possibility of tidal distortions and mass loss via Roche lobe overflow (Gillon et al. 2014).

WASP-103 b’s HST-WFC3 emission spectrum was found to be featureless down to a sensitivity of 175 ppm, showing a shallow slope toward the red (Cartier et al. 2017). Work by Manjavacas et al. (2019), who performed a reanalysis of the same data set, found that the emission spectrum of WASP-103 b was comparable to that of an M-3 dwarf. Delrez et al. (2018) obtained several ground-based high-precision photometric eclipse observations, which, when added to the HST data, could be fit with an isothermal blackbody or with a low water abundance atmosphere with a thermal inversion. However, their K_s-band observation showed an excess of emission compared to both these models. Recently, a phase-curve analysis of the planet was performed and reported in Kreidberg et al. (2018). The study also utilized the previous HST emission spectra and confirmed a seemingly featureless dayside. The phase-resolved spectra of WASP-103 b were compared in this work to those of brown dwarfs and directly imaged companions of similar temperatures, which show evidence for water absorption at 1.4 μm , whereas WASP-103 b showed no such feature. The result could be due to WASP-103 b’s irradiation environment and its low surface gravity. A later study on the same data (Changeat 2022) and employing a unified phase-curve retrieval technique obtained a more complex picture of the planet. It confirmed the presence of thermal inversion and dissociation processes on the dayside of the planet and found a signature of FeH emission. The study also constrained water vapor across the entire atmosphere. Ground-based transmission observations found strong evidence for sodium and potassium (Lendl et al. 2017).

Two HST G141 phase curves of WASP-103 b were obtained (PN: 14050, PI: Kreidberg et al. 2014a), each of which contained a single transit and eclipse. Additionally, two further eclipses were taken with the same instrument (PN: 13660, PI: Zhao 2014).

Our eclipse spectrum of WASP-103 b is not consistent with a pure blackbody fit, thus contrasting with the previous studies. In our reanalysis, we find that our models prefer a thermal inversion with the presence of an optical absorber such as VO or FeH. When Spitzer is included, the model also includes H⁻, which was predicted to be an important opacity source for this atmosphere (Kreidberg et al. 2018). We note, however, that comparing the Bayesian evidence with the reduced models does not provide decisive evidence in favor of the full models, meaning that an atmosphere without these active molecules could also well fit this data set. The metallicity associated with our full runs is centered around solar values but with large uncertainties. For the C/O, because CO₂ is detected in the HST + Spitzer case, the derived value converges to 0.5, but this is most likely due to the lack of detection of other species. When considering the equilibrium chemistry case, a thermal inversion is also inferred from the data. This is associated with solar metallicity and a C/O of about 1.

Analyzing the transit spectrum (PN: 14050, PI: Kreidberg et al. 2014a), we observed that the downward slope is well fit

by VO. Other optical absorbers might be present (TiO, H⁻) but the data do not allow verification of this. The solution found possesses a wide range of metallicities, subsolar in nature. When applying equilibrium chemistry to this data set, the thermal profile converges to unrealistic values for this atmosphere.

D.25. Individual Analysis of WASP-121 b

Significant observational time has been spent on WASP-121 b (Delrez et al. 2016). In transmission, the analyses of ground-based observations, Hubble-STIS, and Hubble-WFC3 have shown the presence of H₂O and optical absorption attributed to VO and/or FeH (Evans et al. 2016b, 2018). The authors of these studies note that chemical equilibrium models with solar abundances cannot reproduce the spectrum seen, while free chemical retrievals can only do so by converging to high abundances of VO and FeH. WASP-121 b has also been observed in eclipse, and the presence of a thermal inversion provides the best fit to the data (Parmentier et al. 2018; Bourrier et al. 2020; Mikal-Evans et al. 2020; Daylan et al. 2021). Bourrier et al. (2020) attributed this to VO with a best-fit abundance of $\log(\text{VO}) = -6.03$, while Mikal-Evans et al. (2020) performed chemical equilibrium retrievals, finding evidence for a muted water feature due to dissociation and H⁻ opacity.

In parallel, high-resolution ground-based observations of the transit have put upper limits on the abundances of TiO and VO at the terminator with $\log(\text{VMR}) < -7.3$ and 7.9 , respectively, suggesting these cannot be causing the inversion seen (Merritt et al. 2020). However, the study highlighted that these limits are largely degenerate with other atmospheric properties such as the scattering properties or the altitude of clouds on WASP-121 b. Another study found a host of atomic metals, including V, which are predicted to exist if a planet is in equilibrium and has a significant quantity of VO (Hoeijmakers et al. 2020). They too noted the absence of TiO, which could support the hypothesis that Ti is depleted via a cold trap.













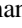
Here, we take the transmission spectrum from Tsiaras et al. 2018 (PN: 14468, PI: Evans (2015) already analyzed using the Iraclis pipeline and supplement it with the two new transit observations recently obtained as part of a phase-curve proposal (Evans (2017a), PN: 15134, PI: . All of these were taken with the WFC3 G141 grism. In emission, we analyze the two available visits with the G102 grism (PN: 15135, PI: Evans 2017b) and the five observations taken using G141, PN: 14767, PI: Sing et al. (2016b); PN: 15134, PI: Evans (2017a). In our most comprehensive retrievals, we also added the Spitzer data sets from G20.

For the planet dayside, we find that the solution depends on the data set considered but because the reduced runs achieve a much lower $\ln(E)$ than the full runs, there is decisive evidence in favor of the presence of optical absorbers for this planet. The full runs are consistent with a thermal inversion, detecting VO and H⁻. This result is independent of whether Spitzer is considered or not. If only HST G141 and G102 grisms are included, we also find evidence for H₂O. When Spitzer is added, the H₂O detection disappears in favor of TiO, a molecule that might be consistent with the temperatures found for this atmosphere, but was thought from previous studies to not be present. Those results are inconsistent with the recent findings in Mikal-Evans et al. (2020), who detected H⁻ and H₂O from the same data set. At this point, it remains difficult to know whether the differences in our interpretation come from

the retrieval setup or from the reduction pipelines. As described previously, different pipelines often lead to different results when combining the data from various instruments. In any case, all our retrievals seem consistent with a strong thermal inversion and H⁻ emission. Whereas the partition between the sources (TiO, VO, FeH, H⁻) could be different, optical absorption is required in all scenarios. The associated metallicity of those free retrievals is subsolar but the C/O remains unconstrained. We also ran equilibrium chemistry retrievals, finding different thermal structures in the free runs. The models still include a thermal inversion, but the thermal profile is decreasing with altitude for the highest pressures. The metallicity in this case is solar to supersolar and associated with high C/O. We note, however, that the Bayesian evidence obtained by the equilibrium chemistry models is much lower than with the free runs.

Our analysis of the transmission spectrum shows the presence of water vapor and H⁻. There is also evidence for absorption due to VO as seen in the posterior distribution. In addition to this, a large pressure range for opaque clouds is allowed, which might consequently have an impact on the degeneracies highlighted for the upper limits of VO and TiO in Merritt et al. (2020). In general, our analysis of the transmission spectrum is consistent with the results from Evans et al. (2018). The metallicity for the free retrieval of the transit spectrum is solar, while the C/O is found to be subsolar. When assuming equilibrium chemistry, a similar metallicity is found, but the C/O is unconstrained.

ORCID iDs

Q. Changeat  <https://orcid.org/0000-0001-6516-4493>
 B. Edwards  <https://orcid.org/0000-0002-5494-3237>
 A. F. Al-Refaie  <https://orcid.org/0000-0003-2241-5330>
 A. Tsiaras  <https://orcid.org/0000-0003-3840-1793>
 J. Y. K. Cho  <https://orcid.org/0000-0002-4525-5651>
 K. H. Yip  <https://orcid.org/0000-0002-9616-1524>
 L. Anisman  <https://orcid.org/0000-0002-7771-6432>
 M. Ikoma  <https://orcid.org/0000-0002-5658-5971>
 M. F. Bieger  <https://orcid.org/0000-0001-9166-3042>
 O. Venot  <https://orcid.org/0000-0003-2854-765X>
 S. Shibata  <https://orcid.org/0000-0002-5418-6336>
 I. P. Waldmann  <https://orcid.org/0000-0002-4205-5267>
 G. Tinetti  <https://orcid.org/0000-0001-6058-6654>

References

- Abe, L., Gonçalves, I., Agabi, A., et al. 2013, *A&A*, 553, A49
 Abel, M., Frommhold, L., Li, X., & Hunt, K. L. 2011, *JPCA*, 115, 6805
 Abel, M., Frommhold, L., Li, X., & Hunt, K. L. 2012, *JChPh*, 136, 044319
 Addison, B., Wright, D. J., Wittenmyer, R. A., et al. 2019, *PASP*, 131, 115003
 Addison, B. C., Tinney, C. G., Wright, D. J., et al. 2013, *ApJL*, 774, L9
 Ahlers, J. P., Johnson, M. C., Stassun, K. G., et al. 2020, *AJ*, 160, 4
 Al Derzi, A. R., Furtenbacher, T., Tennyson, J., Yurchenko, S. N., & Császár, A. G. 2015, *J. Quant. Spec. Radiat. Transf.*, 161, 117
 Alam, M. K., López-Morales, M., Nikolov, N., et al. 2020, *AJ*, 160, 51
 Allard, F., Homeier, D., & Freytag, B. 2012, *RSPTA*, 370, 2765
 Alonso, R., Alapini, A., Aigrain, S., et al. 2009, *A&A*, 506, 353
 Al-Refaie, A. F., Changeat, Q., Venot, O., Waldmann, I. P., & Tinetti, G. 2021b, arXiv:2110.01271
 Al-Refaie, A. F., Changeat, Q., Waldmann, I. P., & Tinetti, G. 2021a, *ApJ*, 917, 37
 Al-Refaie, A. F., Yachmenev, A., Tennyson, J., & Yurchenko, S. N. 2015, *MNRAS*, 448, 1704
 Anderson, D. R., Gillon, M., Maxted, P. F. L., et al. 2010, *A&A*, 513, L3
 Anderson, D. R., Smith, A. M. S., Madhusudhan, N., et al. 2013, *MNRAS*, 430, 3422

- Anisman, L. O., Edwards, B., Changeat, Q., et al. 2020, *AJ*, 160, 233
- Arcangeli, J., Désert, J.-M., Line, M. R., et al. 2018, *ApJL*, 855, L30
- Arcangeli, J., Désert, J.-M., Parmentier, V., et al. 2019, *A&A*, 625, A136
- Armstrong, D. J., de Mooij, E., Barstow, J., et al. 2016, *NatAs*, 1, 0004
- Asplund, M., Grevesse, N., Sauval, A. J., & Scott, P. 2009, *ARA&A*, 47, 481
- Azzam, A. A. A., Tennyson, J., Yurchenko, S. N., & Naumenko, O. V. 2016, *MNRAS*, 460, 4063
- Barber, R. J., Strange, J. K., Hill, C., et al. 2013, *MNRAS*, 437, 1828
- Barge, P., Baglin, A., Auvergne, M., et al. 2008, *A&A*, 482, L17
- Barman, T. 2007, *ApJL*, 661, L191
- Barstow, J. K., Aigrain, S., Irwin, P. G. J., & Sing, D. K. 2017, *ApJ*, 834, 50
- Barton, E. J., Hill, C., Yurchenko, S. N., et al. 2017, *QJSTR*, 187, 453
- Barton, E. J., Yurchenko, S. N., & Tennyson, J. 2013, *MNRAS*, 434, 1469
- Bean, J. L., Desert, J.-M., Dragomir, D., et al. 2016, HST Proposal, 14792
- Bean, J. L., Désert, J.-M., Seifahrt, A., et al. 2013, *ApJ*, 771, 108
- Bean, J. 2013, HST Proposal, 13467
- Beatty, T. G., Collins, K. A., Fortney, J., et al. 2014, *ApJ*, 783, 112
- Beatty, T. G., Deming, D., Fortney, J., et al. 2016, HST Proposal, 14664
- Beatty, T. G., Madhusudhan, N., Pogge, R., et al. 2017, *AJ*, 154, 242
- Beatty, T. G., Madhusudhan, N., Tsiaras, A., et al. 2017, *AJ*, 154, 158
- Bechter, E. B., Crepp, J. R., Ngo, H., et al. 2014, *ApJ*, 788, 2
- Beerer, I. M., Knutson, H. A., Burrows, A., et al. 2010, *ApJ*, 727, 23
- Bell, T. J., & Cowan, N. B. 2018, *ApJL*, 857, L20
- Bell, T. J., Dang, L., Cowan, N. B., et al. 2021, *MNRAS*, 504, 3316
- Bello-Arufe, A., Cabot, S. H. C., Mendonça, J. M., Buchhave, L. A., & Rathcke, A. D. 2022, *AJ*, 163, 96
- Bergfors, C., Brandner, W., Daemgen, S., et al. 2012, *MNRAS*, 428, 182
- Bernath, P. F. 2020, *QJSTR*, 240, 106687
- Bieryla, A., Collins, K., Beatty, T. G., et al. 2015, *AJ*, 150, 12
- Bodenheimer, P., & Pollack, J. B. 1986, *Icar*, 67, 391
- Bohn, A. J., Southworth, J., Ginski, C., et al. 2020, *A&A*, 635, A73
- Booth, R. A., Clarke, C. J., Madhusudhan, N., & Ilee, J. D. 2017, *MNRAS*, 469, 3994
- Borucki, W. J., Koch, D., Jenkins, J., et al. 2009, *Sci*, 325, 709
- Bouma, L. G., Winn, J. N., Baxter, C., et al. 2019, *AJ*, 157, 217
- Bourrier, V., des Etangs, A. L., & Vidal-Madjar, A. 2015, *A&A*, 573, A11
- Bourrier, V., Kitzmann, D., Kuntzer, T., et al. 2020, *A&A*, 637, A36
- Bowesman, C. A., Shuai, M., Yurchenko, S. N., & Tennyson, J. 2021, *MNRAS*, 508, 3181
- Boyajian, T., von Braun, K., Feiden, G. A., et al. 2015, *MNRAS*, 447, 846
- Brewer, J. M., Fischer, D. A., & Madhusudhan, N. 2017, *AJ*, 153, 83
- Brown, D. J. A., Triaud, A. H. M. J., Doyle, A. P., et al. 2017, *MNRAS*, 464, 810
- Burrows, A., Hubeny, I., Budaj, J., Knutson, H. A., & Charbonneau, D. 2007, *ApJL*, 668, L171
- Burrows, A. S. 2014, *PNAS*, 111, 12601
- Burton, J. R., Watson, C. A., Littlefair, S. P., et al. 2012, *ApJS*, 201, 36
- Caldas, A., Leconte, J., Selsis, F., et al. 2019, *A&A*, 623, A161
- Cameron, A. C., Guenther, E., Smalley, B., et al. 2010, *MNRAS*, 407, 507
- Campo, C. J., Harrington, J., Hardy, R. A., et al. 2011, *ApJ*, 727, 125
- Carone, L., Baeyens, R., Mollière, P., et al. 2020, *MNRAS*, 496, 3582
- Cartier, K. M. S., Beatty, T. G., Zhao, M., et al. 2017, *AJ*, 153, 34
- Caulley, P. W., Shkolnik, E. L., Ilyin, I., et al. 2019, *AJ*, 157, 69
- Changeat, Q. 2022, *AJ*, 163, 106
- Changeat, Q., & Al-Refaie, A. 2020, *ApJ*, 898, 155
- Changeat, Q., Al-Refaie, A., Mugnai, L. V., et al. 2020a, *AJ*, 160, 80
- Changeat, Q., Al-Refaie, A. F., Edwards, B., Waldmann, I. P., & Tinetti, G. 2021, *ApJ*, 913, 73
- Changeat, Q., & Edwards, B. 2021, *ApJL*, 907, L22
- Changeat, Q., Edwards, B., Al-Refaie, A. F., et al. 2020b, *AJ*, 160, 260
- Changeat, Q., Edwards, B., Waldmann, I. P., & Tinetti, G. 2019, *ApJ*, 886, 39
- Changeat, Q., Keyte, L., Waldmann, I. P., & Tinetti, G. 2020c, *ApJ*, 896, 107
- Charbonneau, D., Brown, T. M., Latham, D. W., & Mayor, M. 2000, *ApJL*, 529, L45
- Charbonneau, D., Brown, T. M., Noyes, R. W., & Gilliland, R. L. 2002, *ApJ*, 568, 377
- Charbonneau, D., Knutson, H. A., Barman, T., et al. 2008, *ApJ*, 686, 1341
- Cho, J. Y.-K., Menou, K., Hansen, B. M. S., & Seager, S. 2003, *ApJL*, 587, L117
- Cho, J. Y.-K., Polichtchouk, I., & Thrastarson, H. T. 2015, *MNRAS*, 454, 3423
- Cho, J. Y.-K., Skinner, J. W., & Thrastarson, H. T. 2021, *ApJL*, 913, L32
- Christiansen, J. L., Ballard, S., Charbonneau, D., et al. 2010, *ApJ*, 710, 97
- Christiansen, J. L., Ballard, S., Charbonneau, D., et al. 2011, *ApJ*, 726, 94
- Chubb, K. L., Min, M., Kawashima, Y., Helling, C., & Waldmann, I. 2020a, *A&A*, 639, A3
- Chubb, K. L., Rocchetto, M., Yurchenko, S. N., et al. 2021, *A&A*, 646, A21
- Chubb, K. L., Tennyson, J., & Yurchenko, S. N. 2020b, *MNRAS*, 493, 1531
- Coles, P. A., Yurchenko, S. N., & Tennyson, J. 2019, *MNRAS*, 490, 4638
- Collier Cameron, A., Guenther, E., Smalley, B., et al. 2010, *MNRAS*, 407, 507
- Collins, K. A., Kielkopf, J. F., & Stassun, K. G. 2017, *AJ*, 153, 78
- Cowan, N. B., & Agol, E. 2011, *ApJ*, 729, 54
- Cowan, N. B., Machalek, P., Croll, B., et al. 2012, *ApJ*, 747, 82
- Cox, A. N. 2015, *Allen's Astrophysical Quantities* (Berlin: Springer)
- Cridland, A. J., van Dishoeck, E. F., Alessi, M., & Pudritz, R. E. 2019, *A&A*, 632, A63
- Croll, B., Jayawardhana, R., Fortney, J. J., Lafrenière, D., & Albert, L. 2010, *ApJ*, 718, 920
- Crossfield, I. J. M., Barman, T., Hansen, B. M. S., Tanaka, I., & Kodama, T. 2012a, *ApJ*, 760, 140
- Crossfield, I. J. M., Knutson, H., Fortney, J., et al. 2012b, *ApJ*, 752, 81
- Crossfield, I. J. M., & Kreidberg, L. 2017, *AJ*, 154, 261
- Crouzet, N., McCullough, P. R., Deming, D., & Madhusudhan, N. 2014, *ApJ*, 795, 166
- Damiano, M., Morello, G., Tsiaras, A., Zingales, T., & Tinetti, G. 2017, *AJ*, 154, 39
- Daylan, T., Günther, M. N., Mikal-Evans, T., et al. 2021, *AJ*, 161, 131
- de Mooij, E. J. W., & Snellen, I. A. G. 2009, *A&A*, 493, L35
- Delrez, L., Madhusudhan, N., Lendl, M., et al. 2018, *MNRAS*, 474, 2334
- Delrez, L., Santerne, A., Almenara, J. M., et al. 2016, *MNRAS*, 458, 4025
- Deming, D. 2010, HST Proposal, 12181
- Deming, D. 2011, HST Proposal, 12495
- Deming, D., Benneke, B., Fraine, J., et al. 2015, HST Proposal, 14260
- Deming, D., Fraine, J. D., Sada, P. V., et al. 2012, *ApJ*, 754, 106
- Deming, D., Knutson, H., Agol, E., et al. 2010, *ApJ*, 726, 95
- Deming, D., Wilkins, A., McCullough, P., et al. 2013, *ApJ*, 774, 95
- Desert, J.-M., Stevenson, K., Arcangeli, J., et al. 2020, HST Proposal, 16194
- Diamond-Lowe, H., Stevenson, K. B., Bean, J. L., Line, M. R., & Fortney, J. J. 2014, *ApJ*, 796, 66
- Edwards, B., Changeat, Q., Baeyens, R., et al. 2020, *AJ*, 160, 8
- Edwards, B., Changeat, Q., Mori, M., et al. 2021, *AJ*, 161, 44
- Edwards, B., Mugnai, L., Tinetti, G., Pascale, E., & Sarkar, S. 2019a, *AJ*, 157, 242
- Edwards, B., Rice, M., Zingales, T., et al. 2019b, *ExA*, 47, 29
- Eistrup, C., Walsh, C., & van Dishoeck, E. F. 2018, *A&A*, 613, A14
- Esteves, L. J., De Mooij, E. J. W., & Jayawardhana, R. 2013, *ApJ*, 772, 51
- Esteves, L. J., Mooij, E. J. W. D., & Jayawardhana, R. 2015, *ApJ*, 804, 150
- Evans, D. F., Southworth, J., Maxted, P. F. L., et al. 2016a, *A&A*, 589, A58
- Evans, T. 2015, HST Proposal, 14468
- Evans, T. 2017a, HST Proposal, 15134
- Evans, T. 2017b, HST Proposal, 15135
- Evans, T. M., Aigrain, S., Gibson, N., et al. 2015, *MNRAS*, 451, 680
- Evans, T. M., Sing, D. K., Goyal, J. M., et al. 2018, *AJ*, 156, 283
- Evans, T. M., Sing, D. K., Wakeford, H. R., et al. 2016b, *ApJL*, 822, L4
- Feng, Y. K., Line, M. R., Fortney, J. J., et al. 2016, *ApJ*, 829, 52
- Feng, Y. K., Line, M. R., & Fortney, J. J. 2020, *AJ*, 160, 137
- Feroz, F., Hobson, M. P., & Bridges, M. 2009, *MNRAS*, 398, 1601
- Fisher, C., & Heng, K. 2018, *MNRAS*, 481, 4698
- Fletcher, L. N., Gustafsson, M., & Orton, G. S. 2018, *ApJS*, 235, 24
- Fortney, J. J., Lodders, K., Marley, M. S., & Freedman, R. S. 2008, *ApJ*, 678, 1419
- Fressin, F., Knutson, H. A., Charbonneau, D., et al. 2010, *ApJ*, 711, 374
- Fu, G., Deming, D., Ih, J., Kempton, E. M. R., & Malik, M. 2020, HST Proposal, 16307
- Fu, G., Deming, D., Lothringer, J., et al. 2021, *AJ*, 162, 108
- Gandhi, S., & Madhusudhan, N. 2019, *MNRAS*, 485, 5817
- Gandhi, S., Madhusudhan, N., & Mandell, A. 2020, *AJ*, 159, 232
- Gardner, J. P., Mather, J. C., Clampin, M., et al. 2006, *SSRv*, 123, 485
- Garhart, E., Deming, D., Mandell, A., et al. 2020, *AJ*, 159, 137
- Gaudi, B. S., Stassun, K. G., Collins, K. A., et al. 2017, *Natur*, 546, 514
- Gillon, M., Anderson, D. R., Collier-Cameron, A., et al. 2014, *A&A*, 562, L3
- Gillon, M., Demory, B.-O., Triaud, A. H. M. J., et al. 2009, *A&A*, 506, 359
- Gordon, I., Rothman, L. S., Wilzewski, J. S., et al. 2016, AAS/DPS Meeting, 48, 421.13
- Grillmair, C. J., Burrows, A., Charbonneau, D., et al. 2008, *Natur*, 456, 767
- Guilluy, G., Gressier, A., Wright, S., et al. 2021, *AJ*, 161, 19
- Hartman, J. D., Bakos, G. A., Torres, G., et al. 2011, *ApJ*, 742, 59
- Hartman, J. D., Bakos, G. Á., Béky, B., et al. 2012, *AJ*, 144, 139
- Hasegawa, Y., Bryden, G., Ikoma, M., Vasisht, G., & Swain, M. 2018, *ApJ*, 865, 32
- Haynes, K., Mandell, A. M., Madhusudhan, N., Deming, D., & Knutson, H. 2015, *ApJ*, 806, 146

- Hellier, C., Anderson, D. R., Collier Cameron, A., et al. 2009, *Natur*, **460**, 1098
- Hellier, C., Anderson, D. R., Collier Cameron, A., et al. 2011, *A&A*, **535**, L7
- Hellier, C., Anderson, D. R., Collier Cameron, A., et al. 2015, *AJ*, **150**, 18
- Helling, C., Iro, N., Corrales, L., et al. 2019, *A&A*, **631**, A79
- Helling, C., Kawashima, Y., Graham, V., et al. 2020, *A&A*, **641**, A178
- Helling, C., Lewis, D., Samra, D., et al. 2021, *A&A*, **649**, A44
- Henry, G. W., Marcy, G. W., Butler, R. P., & Vogt, S. S. 2000, *ApJL*, **529**, L41
- Herman, M. K., Mooij, E. J. W. d., Jayawardhana, R., & Brogi, M. 2020, *AJ*, **160**, 93
- Herrero, E., Morales, J. C., Ribas, I., & Naves, R. 2011, *A&A*, **526**, L10
- Hill, C., Yurchenko, S. N., & Tennyson, J. 2013, *Icar*, **226**, 1673
- Hoeijmakers, H. J., Ehrenreich, D., Heng, K., et al. 2018, *Natur*, **560**, 453
- Hoeijmakers, H. J., Ehrenreich, D., Kitzmann, D., et al. 2019, *A&A*, **627**, A165
- Hoeijmakers, H. J., Seidel, J. V., Pino, L., et al. 2020, *A&A*, **641**, A123
- Hubeny, I., & Burrows, A. 2009, in IAU Symp. 253, *Transiting Planets*, ed. F. Pont, D. Sasselov, & M. J. Holman (Cambridge: Cambridge Univ. Press), 239
- Huitson, C. 2013, HST Proposal, 13431
- Ikoma, M., Nakazawa, K., & Emori, H. 2000, *ApJ*, **537**, 1013
- Iro, N., & Maxted, P. F. L. 2013, *Icar*, **226**, 1719
- Irwin, P. G. J., Parmentier, V., Taylor, J., et al. 2020, *MNRAS*, **493**, 106
- Jeffreys, H. 1961, *Theory of Probability* (Oxford: Clarendon)
- John, T. L. 1988, *A&A*, **193**, 189
- Johnson, M. C., Cochran, W. D., Addison, B. C., Tinney, C. G., & Wright, D. J. 2017, *AJ*, **154**, 137
- Kass, R., & Raftery, A. 1995, *J. Am. Stat. Assoc.*, **90**, 773
- Kedziora-Chudczer, L., Zhou, G., Bailey, J., et al. 2019, *MNRAS*, **483**, 5110
- Kitzmann, D., Heng, K., Rimmer, P. B., et al. 2018, *ApJ*, **863**, 183
- Knutson, H. A., Charbonneau, D., Allen, L. E., Burrows, A., & Megeath, S. T. 2008, *ApJ*, **673**, 526
- Knutson, H. A., Howard, A. W., & Isaacson, H. 2010, *ApJ*, **720**, 1569
- Komacek, T. D., & Showman, A. P. 2020, *ApJ*, **888**, 2
- Bakos, G. Á., Kovács, G., Torres, G., et al. 2007, *ApJ*, **670**, 826
- Kreidberg, L., Bean, J., Stevenson, K., et al. 2014a, *Spitzer Proposal*, 11099
- Kreidberg, L., Bean, J. L., Désert, J.-M., et al. 2014b, *ApJL*, **793**, L27
- Kreidberg, L., Bean, J. L., Désert, J.-M., et al. 2014c, *Natur*, **505**, 69
- Kreidberg, L., Line, M. R., Bean, J. L., et al. 2015, *ApJ*, **814**, 66
- Kreidberg, L., Line, M. R., Parmentier, V., et al. 2018, *AJ*, **156**, 17
- Lee, J.-M., Heng, K., & Irwin, P. G. J. 2013, *ApJ*, **778**, 97
- Lendl, M., Cubillos, P. E., Hagelberg, J., et al. 2017, *A&A*, **606**, A18
- Lewis, N. K., Knutson, H. A., Showman, A. P., et al. 2013, *ApJ*, **766**, 95
- Lewis, N. K., Showman, A. P., Fortney, J. J., Knutson, H. A., & Marley, M. S. 2014, *ApJ*, **795**, 150
- Li, G., Gordon, I. E., Rothman, L. S., et al. 2015, *ApJS*, **216**, 15
- Li, H. Y., Tennyson, J., & Yurchenko, S. N. 2019, *MNRAS*, **486**, 2351
- Libby-Roberts, J. E., Berta-Thompson, Z. K., Diamond-Lowe, H., et al. 2021, arXiv:2105.10487
- Line, M. R., Brogi, M., Bean, J. L., et al. 2021, *Natur*, **598**, 580
- Line, M. R., Knutson, H., Wolf, A. S., & Yung, Y. L. 2014, *ApJ*, **783**, 70
- Line, M. R., Stevenson, K. B., Bean, J., et al. 2016, *AJ*, **152**, 203
- Lodders, K. 2002, *ApJ*, **577**, 974
- Lodi, L., Yurchenko, S. N., & Tennyson, J. 2015, *MolPh*, **113**, 1998
- Loeillet, B., Shporer, A., Bouchy, F., et al. 2008, *A&A*, **481**, 529
- Lothringer, J. D., Barman, T., & Koskinen, T. 2018, *ApJ*, **866**, 27
- Lothringer, J. D., Rustamkulov, Z., Sing, D. K., et al. 2021, *ApJ*, **914**, 12
- Luque, R., Casasayas-Barris, N., Parviainen, H., et al. 2020, arXiv:2007.11851
- MacDonald, R. J., Goyal, J. M., & Lewis, N. K. 2020, *ApJL*, **893**, L43
- MacDonald, R. J., & Madhusudhan, N. 2017, *MNRAS*, **469**, 1979
- MacDonald, R. J., & Madhusudhan, N. 2019, *MNRAS*, **486**, 1292
- Madhusudhan, N., Bitsch, B., Johansen, A., & Eriksson, L. 2017, *MNRAS*, **469**, 4102
- Madhusudhan, N., Crouzet, N., McCullough, P. R., Deming, D., & Hedges, C. 2014, *ApJL*, **791**, L9
- Madhusudhan, N., Harrington, J., Stevenson, K. B., et al. 2011, *Natur*, **469**, 64
- Madhusudhan, N., & Seager, S. 2010, *ApJ*, **725**, 261
- Mancini, L., Southworth, J., Mollière, P., et al. 2019, *MNRAS*, **485**, 5168
- Manjavacas, E., Apai, D., Zhou, Y., et al. 2019, *AJ*, **157**, 101
- Mansfield, M., Arcangeli, J., Bean, J. L., et al. 2020a, HST Proposal, 16168
- Mansfield, M., Bean, J. L., Line, M. R., et al. 2018, *AJ*, **156**, 10
- Mansfield, M., Bean, J. L., Stevenson, K. B., et al. 2020b, *ApJL*, **888**, L15
- Mansfield, M., Line, M. R., Bean, J. L., et al. 2021, *NatAs*, **5**, 1224
- Mant, B. P., Yachmenev, A., Tennyson, J., & Yurchenko, S. N. 2018, *MNRAS*, **478**, 3220
- Maxted, P. F. L., Anderson, D. R., Collier Cameron, A., et al. 2013, *PASP*, **125**, 48
- May, E. M., & Stevenson, K. B. 2020, *AJ*, **160**, 140
- McCullough, P. 2012, HST Proposal, 12881
- McCullough, P., & MacKenty, J. 2012, Considerations for Using Spatial Scans with WFC3, Instrument Science Report WFC3 2012-08, (Baltimore, MD: STScI), https://www.stsci.edu/files/live/sites/www/files/home/hst/instrumentation/wfc3/documentation/instrument-science-reports-isrs/_documents/2012/WFC3-2012-08.pdf
- McCullough, P. R., Crouzet, N., Deming, D., & Madhusudhan, N. 2014, *ApJ*, **791**, 55
- McKemmish, L. K., Masseron, T., Hoeijmakers, H. J., et al. 2019, *MNRAS*, **488**, 2836
- McKemmish, L. K., Yurchenko, S. N., & Tennyson, J. 2016, *MNRAS*, **463**, 771
- Mendonça, J. M., Malik, M., Demory, B.-O., & Heng, K. 2018a, *AJ*, **155**, 150
- Mendonça, J. M., Tsai, S.-m., Malik, M., Grimm, S. L., & Heng, K. 2018b, *ApJ*, **869**, 107
- Merritt, S. R., Gibson, N. P., Nugroho, S. K., et al. 2020, *A&A*, **636**, A117
- Mikal-Evans, T., Sing, D. K., Kataria, T., et al. 2020, *MNRAS*, **496**, 1638
- Miller, N., & Fortney, J. J. 2011, *ApJL*, **736**, L29
- Min, M., Ormel, C. W., Chubb, K., Helling, C., & Kawashima, Y. 2020, *A&A*, **642**, A28
- Mizuno, H. 1980, *PThPh*, **64**, 544
- Mordasini, C., van Boekel, R., Mollière, P., Henning, T., & Benneke, B. 2016, *ApJ*, **832**, 41
- Morello, G., Danielski, C., Dickens, D., Tremblin, P., & Lagage, P. O. 2019, *AJ*, **157**, 205
- Mugnai, L. V., Modirrousta-Galian, D., Edwards, B., et al. 2021, *AJ*, **161**, 284
- Nikolov, N., Sing, D. K., Goyal, J., et al. 2018, *MNRAS*, **474**, 1705
- Nugroho, S. K., Kawahara, H., Masuda, K., et al. 2017, *AJ*, **154**, 221
- Nymeyer, S., Harrington, J., Hardy, R. A., et al. 2011, *ApJ*, **742**, 35
- O'Donovan, F. T., Charbonneau, D., Bakos, G. A., et al. 2007, *ApJL*, **663**, L37
- Oreshenko, M., Lavie, B., Grimm, S. L., et al. 2017, *ApJL*, **847**, L3
- Pál, A., Bakos, G. Á., Torres, G., et al. 2008, *ApJ*, **680**, 1450
- Pál, A., Bakos, G. Á., Torres, G., et al. 2010, *MNRAS*, **401**, 2665
- Parmentier, V., & Crossfield, I. J. M. 2017, *Handbook of Exoplanets* (Cham: Springer), 116
- Parmentier, V., Line, M. R., Bean, J. L., et al. 2018, *A&A*, **617**, A110
- Patrascu, A. T., Yurchenko, S. N., & Tennyson, J. 2015, *MNRAS*, **449**, 3613
- Peek, J., Desai, V., White, R. L., et al. 2019, *BAAS*, **51**, 105
- Pinhas, A., Madhusudhan, N., Gandhi, S., & MacDonald, R. 2019, *MNRAS*, **482**, 1485
- Pino, L., Arcangeli, J., Bean, J. L., et al. 2019, HST Proposal, 15820
- Pino, L., Désert, J.-M., Brogi, M., et al. 2020, *ApJL*, **894**, L27
- Pluriel, W., Whiteford, N., Edwards, B., et al. 2020, *AJ*, **160**, 112
- Pluriel, W., Zingales, T., Leconte, J., & Parmentier, V. 2020, *A&A*, **636**, A66
- Polyansky, O. L., Kyuberis, A. A., Zobov, N. F., et al. 2018, *MNRAS*, **480**, 2597
- Qin, Z., Bai, T., & Liu, L. 2021, *JQSRT*, **258**, 107352
- Ram, R., Brooke, J., Western, C., & Bernath, P. 2014, *JQSRT*, **138**, 107
- Ranjana, S., Charbonneau, D., Désert, J.-M., et al. 2014, *ApJ*, **785**, 148
- Rathcke, A. D., MacDonald, R. J., Barstow, J. K., et al. 2021, *AJ*, **162**, 138
- Reach, W. T., Megeath, S. T., Cohen, M., et al. 2005, *PASP*, **117**, 978
- Rocchetto, M., Waldmann, I. P., Venot, O., Lagage, P.-O., & Tinetti, G. 2016, *ApJ*, **833**, 120
- Roth, A., Drummond, B., Hébrard, E., et al. 2021, *MNRAS*, **505**, 4515
- Rothman, L. S., & Gordon, I. E. 2014, 13th Biennial HITRAN Conf. (Cambridge, MA: Harvard-Smithsonian Center for Astrophysics), 49
- Saba, A., Tsiaras, A., Morvan, M., et al. 2021, arXiv:2108.13721
- Saumon, D., & Guillot, T. 2004, *ApJ*, **609**, 1170
- Sedaghati, E., Boffin, H. M. J., MacDonald, R. J., et al. 2017, *Natur*, **549**, 238
- Serindag, D. B., Nugroho, S. K., Mollière, P., et al. 2021, *A&A*, **645**, A90
- Sheppard, K. B., Mandell, A. M., Tamburo, P., et al. 2017, *ApJL*, **850**, L32
- Shibata, S., Helled, R., & Ikoma, M. 2020, *A&A*, **633**, A33
- Shibata, S., & Ikoma, M. 2019, *MNRAS*, **487**, 4510
- Showman, A. P., Cho, J. Y.-K., & Menou, K. 2010, in *Exoplanets*, ed. S. Seager (Tucson, AZ: Univ. Arizona Press), 471
- Shporer, A., Jenkins, J. M., Rowe, J. F., et al. 2011, *AJ*, **142**, 195
- Shporer, A., O'Rourke, J. G., Knutson, H. A., et al. 2014, *ApJ*, **788**, 92
- Shporer, A., Wong, I., Huang, C. X., et al. 2019, *AJ*, **157**, 178
- Sing, D. K., Fortney, J. J., Nikolov, N., et al. 2016a, *Natur*, **529**, 59
- Sing, D. K., Lecavelier des Etangs, A., Fortney, J. J., et al. 2013, *MNRAS*, **436**, 2956
- Sing, D. K., Lopez-Morales, M., Ballester, G. E., et al. 2016b, HST Proposal, 14767
- Siverd, R. J., Beatty, T. G., Pepper, J., et al. 2012, *ApJ*, **761**, 123
- Skaf, N., Fabienne Bieger, M., Edwards, B., et al. 2020, *AJ*, **160**, 109

- Skinner, J. W., & Cho, J. Y.-K. 2021a, *MNRAS*, **504**, 5172
- Skinner, J. W., & Cho, J. Y.-K. 2021b, *MNRAS*, **511**, 3584
- Smalley, B., Anderson, D. R., Collier-Cameron, A., et al. 2012, *A&A*, **547**, A61
- Snellen, I. A. G., de Kok, R. J., de Mooij, E. J. W., & Albrecht, S. 2010, *Natur*, **465**, 1049
- Sotzen, K. S., Stevenson, K. B., Sing, D. K., et al. 2020, *AJ*, **159**, 5
- Sousa-Silva, C., Al-Refaie, A. F., Tennyson, J., & Yurchenko, S. N. 2015, *MNRAS*, **446**, 2337
- Southworth, J. 2011, *MNRAS*, **417**, 2166
- Southworth, J., Bohn, A. J., Kenworthy, M. A., Ginski, C., & Mancini, L. 2020, *A&A*, **635**, A74
- Spiegel, D. S., & Burrows, A. 2010, *ApJ*, **722**, 871
- Spiegel, D. S., Silverio, K., & Burrows, A. 2009, *ApJ*, **699**, 1487
- Stassun, K. G., Collins, K. A., & Gaudi, B. S. 2017, *AJ*, **153**, 136
- Stevenson, K. B., Bean, J. L., Madhusudhan, N., & Harrington, J. 2014, *ApJ*, **791**, 36
- Stevenson, K. B., Bean, J. L., Seifahrt, A., et al. 2014, *AJ*, **147**, 161
- Stevenson, K. B., Line, M. R., Bean, J. L., et al. 2017, *AJ*, **153**, 68
- Swain, M. 2010, HST Proposal, 12230
- Swain, M., Deroo, P., Tinetti, G., et al. 2013, *Icar*, **225**, 432
- Swain, M. R., Bouwman, J., Akeson, R. L., Lawler, S., & Beichman, C. A. 2008a, *ApJ*, **674**, 482
- Swain, M. R., Deroo, P., Griffith, C. A., et al. 2010, *Natur*, **463**, 637
- Swain, M. R., Vasisht, G., & Tinetti, G. 2008b, *Natur*, **452**, 329
- Swain, M. R., Vasisht, G., Tinetti, G., et al. 2008c, arXiv:0812.1844
- Syme, A.-M., & McKemmish, L. K. 2021, *MNRAS*, **505**, 4383
- Tan, X., & Komacek, T. D. 2019, *ApJ*, **886**, 26
- Taylor, J., Parmentier, V., Irwin, P. G. J., et al. 2020, *MNRAS*, **493**, 4342
- Tennyson, J., Yurchenko, S. N., Al-Refaie, A. F., et al. 2016, *JMoSp*, **327**, 73
- Thorngrren, D. P., Fortney, J. J., Murray-Clay, R. A., & Lopez, E. D. 2016, *ApJ*, **831**, 64
- Tinetti, G., Drossart, P., Eccleston, P., et al. 2018, *ExA*, **46**, 135
- Tinetti, G., Eccleston, P., Haswell, C., et al. 2021, arXiv:2104.04824
- Tinetti, G., Vidal-Madjar, A., Liang, M.-C., et al. 2007, *Natur*, **448**, 169
- Todorov, K. O., Deming, D., Burrows, A., & Grillmair, C. J. 2014, *ApJ*, **796**, 100
- Tsiaras, A., Rocchetto, M., Waldmann, I. P., et al. 2016c, *ApJ*, **820**, 99
- Tsiaras, A., Waldmann, I., Rocchetto, M., et al. 2016a, pylightcurve: Exoplanet lightcurve model, Astrophysics Source Code Library, ascl:1612.018
- Tsiaras, A., Waldmann, I. P., Rocchetto, M., et al. 2016b, *ApJ*, **832**, 202
- Tsiaras, A., Waldmann, I. P., Tinetti, G., Tennyson, J., & Yurchenko, S. N. 2019, *NatAs*, **3**, 1086
- Tsiaras, A., Waldmann, I. P., Zingales, T., et al. 2018, *AJ*, **155**, 156
- Turner, J. D., de Mooij, E. J. W., Jayawardhana, R., et al. 2020, *ApJL*, **888**, L13
- Turrini, D., Schisano, E., Fonte, S., et al. 2021, *ApJ*, **909**, 40
- Varley, R., Tsiaras, A., & Karpouzas, K. 2017, *ApJS*, **231**, 13
- Venot, O., Parmentier, V., Blecic, J., et al. 2020, *ApJ*, **890**, 176
- von Essen, C., Czesla, S., Wolter, U., et al. 2014, *A&A*, **561**, A48
- von Essen, C., Mallonn, M., Welbanks, L., et al. 2019, *A&A*, **622**, A71
- Wakeford, H. R., Sing, D. K., Deming, D., et al. 2018, *AJ*, **155**, 29
- Wakeford, H. R., Sing, D. K., Stevenson, K. B., et al. 2020, *AJ*, **159**, 204
- Waldmann, I. P., Rocchetto, M., Tinetti, G., et al. 2015a, *ApJ*, **813**, 13
- Waldmann, I. P., Tinetti, G., Rocchetto, M., et al. 2015b, *ApJ*, **802**, 107
- Wang, Y.-H., Wang, S., Hinse, T. C., et al. 2019, *AJ*, **157**, 82
- Welbanks, L., Madhusudhan, N., Allard, N. F., et al. 2019, *ApJL*, **887**, L20
- West, R. G., Hellier, C., Almenara, J. M., et al. 2016, *A&A*, **585**, A126
- Wilkins, A. N., Deming, D., Madhusudhan, N., et al. 2014, *ApJ*, **783**, 113
- Wilson, D. M., Gillon, M., Hellier, C., et al. 2008, *ApJL*, **675**, L113
- Winn, J. N., Holman, M. J., Torres, G., et al. 2008, *ApJ*, **683**, 1076
- Winn, J. N., Johnson, J. A., Peek, K. M. G., et al. 2007, *ApJL*, **665**, L167
- Woitke, P., Helling, C., Hunter, G. H., et al. 2018, *A&A*, **614**, A1
- Wong, I., Benneke, B., Shporer, A., et al. 2020b, *AJ*, **159**, 104
- Wong, I., Knutson, H. A., Kataria, T., et al. 2016, *ApJ*, **823**, 122
- Wong, I., Shporer, A., Kitzmann, D., et al. 2020a, *AJ*, **160**, 88
- Yan, F., Casasayas-Barris, N., Molaverdikhani, K., et al. 2019, *A&A*, **632**, A69
- Yip, K. H., Changeat, Q., Edwards, B., et al. 2021, *AJ*, **161**, 4
- Yip, K. H., Tsiaras, A., Waldmann, I. P., & Tinetti, G. 2020, *AJ*, **160**, 171
- Yurchenko, S. N., Mellor, T. M., Freedman, R. S., & Tennyson, J. 2020, *MNRAS*, **496**, 5282
- Yurchenko, S. N., & Tennyson, J. 2014, *MNRAS*, **440**, 1649
- Yurchenko, S. N., Tennyson, J., Syme, A.-M., et al. 2022, *MNRAS*, **510**, 903
- Zhao, M. 2013, HST Proposal, 13308
- Zhao, M. 2014, HST Proposal, 13660
- Zhao, M., O'Rourke, J. G., Wright, J. T., et al. 2014, *ApJ*, **796**, 115
- Zhou, G., Huang, C. X., Bakos, G. A., et al. 2019, *AJ*, **158**, 141